Lumped Impedance Matchers and GHz Noise Investigation of Quantum Dots

Inauguraldissertation

zur
Erlangung der Würde eines Doktors der Philosophie
vorgelegt der
Philosophisch-Naturwissenschaftlichen Fakultät
der Universität Basel

von

Mihai-Cezar Harabula
von Frankreich und Rumänien

Basel, 2019

Genehmigt von der Philosophisch-Naturwissenschaftlichen Fakultät
auf Antrag von

Prof. Dr. Christian Schönenberger
Dr. Erwann Bocquillon
Dr. Andreas Hüttel
Dr. Gergő Fülöp

Basel, 24.4.2018

Prof. Dr. Martin Spiess
Dekan

Contents

Introduction

One investigates physical systems by *looking* at them or by *inquiring* them. If finding the right questions is craft, then having the most enriching dialog with nature is art. On their path to becoming artists, scientists need first to imagine and create tools that convey the words of nature. And so have we tried, too, to make a chat room for nanoscale objects and to invite them to talk. This room is a microwave setup, a cryostat, where quietness emerges at low temperatures. My role was to have *them* listen and talk back by way of an impedance-matching resonator. So questions started being asked, as you may expect, and even ended answered, as you may hope. Until the moment we began to ask not for the sake of a response, that did keep coming, but... for the mumbling sound that always accompanies answers. It is unusual to engage in conversation not for the exchanged words, but for the murmur that tickles our ears. Still, we diverged from our way to artistic consecration and looked for noise. We persistently formulated questions with gate and bias voltages, yet the current noise was our interest. Why so? Were we searching a hardly whispered coded message? Was not all said in loudly spoken current? In our defense, we don't mistrust the current message, but hoped for more. It resonated out and here it is.

Before presenting our findings, let me come back to a more common language style in our scientific community. The marriage of microwave circuitry and quantum devices has seen a consistently growing interest during the last decade, owing to the emergence of a promising field: the quantum computer with superconducting qubits [1], commonly called *circuit quantum electrodynamics* (cQED). Inflamed by a seminal proof of concept in 2004 [2], at the bottom of the field stays an older, Nobel-prized research domain: cavity quantum electrodynamics. In this foundational domain, qubits (physical systems able to hold each a superposition of two states, denoted by 0 and 1) were made out of atoms, in an optical cavity [3]. This initial research domain spawned into its microwave version, cQED, in which (i) cavities are wave-bearing transmission lines with capacitive couplings (mirrors) at their ends and (ii) atoms are several-state quantum devices.

Not only superconducting qubit control, but also readout of very resistive quantum devices needs microwave resonators, operating at frequencies in the range of $1-10\,\mathrm{GHz}$. To efficiently measure radiation emitted from a device, one attempts to couple the high device impedance to the $Z_0 = 50\,\Omega$ characteristic impedance of the usual coaxial lines using an impedance-matching circuit. These circuits are often implemented with superconducting on-chip transmission lines. Examples include the quarter-wavelength step transformer in the fluxonium qubit [4], stub tuners for quantum point contacts [5] and quantum dots [6, 7]. An alternative approach makes use of an LC resonator built either from a lumped element inductor [8] or form on-chip coils [9]. Nonetheless, the resonance frequencies have typically been limited to a maximum of $\sim$1 GHz [10–12].

This thesis continues the work carried out in our group in terms of microwave measurements of quantum devices [13, 14], with stress now on superconducting lumped resonators as impedance transformers, instead of the distributed, relatively large stub tuners. Addressing here the compactness of GHz resonators, we fabricate 200-μm-wide on-chip superconducting coils with wire-bonded bridges and utilize them as lumped LC matching circuits in a carbon nanotube quantum dot noise experiment. Compared to the previously reported case of on-chip inductor with bonded bridge [11, 15], we achieved a threefold frequency increase with a similar footprint decrease. Our results are equally important in cQED: When aiming quantum supremacy (the character of a computer to solve in linear times problems that even the best classical-bit-manipulating algorithm solves in exponential times) and error-correcting redundancy, the number of needed qubits rapidly increase. Yet, microwave cavities are mm-long, making hard to so many qubits to share the limited volume of a cryostat. Therefore, great interest resides in replacing transmission line resonators by lumped-element resonators. Comparable compactness to that of our LC circuit has been achieved only with Josephson junction arrays acting as quarter-wavelength resonators [16, 17].

The overlap continues in more ways: Due to the larger bandwidth exhibited by LC-like resonators, readout times decrease significantly, and this is beneficial to qubits, too. Moreover, to ensure high fields in the region where such resonators couple with the quantum device [18], efforts were made to increase their characteristic impedance [17]. An attractive finding of our work is the fit-supported validation of a lumped-resonator version in which the inductance is boosted, and with it the characteristic impedance.

The second direction of this thesis is a deeper GHz-noise-based investigation of transport phenomena in quantum dots. Distinct from what the qubit-focused measurements, our noise measurements are based on the idea that noise can be the signal [19]. The noise data triggered analyses of features that are potential projections of quantum transport phenomena.

Electrical transport and noise phenomena in quantum dots (QDs) have been studied in experimental [20–24] and theoretical works [25–28]. Theory has shown that in single-level QDs the Pauli exclusion principle and the repulsive Coulomb interaction result in anti-bunching [25–28]. However, occupation dynamics in multi-level QDs can give rise to bunching, and correspondingly, super-Poissonian noise [29–32]. The electron transport in an interacting two-level system is a telegraphic process if the tunnel couplings of one level are much stronger than of the other [31, 32]. This system supports a high current through the strongly coupled level, which is strongly reduced for random intervals when the weakly coupled level is filled. The electrons transferred in the highly conducting state form bunches and result in enhanced noise. Recently, noise measurements have been applied to probe the correlations induced by the many-body Kondo effect [24]. It has been demonstrated that the increased effective charge results in enhanced shot noise.

In general, such a state in which the QD can be trapped, thus blocking the current, is referred to as a blocking state [33]. We investigate blocking states through conductance and noise spectroscopy in CNT QDs. Different blocking-state pictures were identified under their enhanced-noise signature. A distinction is made between augmented noise and negative differential conductance. The studies were convincingly supported by numerical simulations.

At last, surprisingly, these analyses improved in our circles the understanding of the quantum dot language, that still misleadingly refers to chemical potential levels with the term *state* instead of *transition* between states [34].

This thesis has the following structure: Chapter 1 introduces the reader to microwave theory and details practical aspects of rf[1]-circuit design, like signal flow graphs Chapter 2 presents the basic physics of carbon nanotubes, then treats transport in quantum dots, from Coulomb diamonds to the interplay of cotunneling and sequential tunneling. This is also where quantum dot transport language is clarified. Chapter 3 gives the formal definitions of noise spectral densities and points to different limits of the current noise. Telegraphic transport, later employed in our noise interpretations, is shortly developed. Chapter 4 exhibits design and fabrication methods specific to microwave lumped resonators. The measurement setup is briefly exposed. Chapter 5 presents the data and the calibration methods. An alternative LC-like model is presented and validated together with a standing-wave pattern removal method. Chapter 6 is the *pièce de résistance* of our noise and conductance analysis. It identifies and confirms by numerical simulations blocking states that lead to enhanced-noise transport phenomena. At the end, chapter 7 uses the conclusions of the previous chapter to explain cotunneling-assisted sequential tunneling outside Coulomb diamonds.

---

[1] rf = radio frequencies, i.e. 20 kHz – 300 GHz. The microwave spectrum is usually considered to contain the rf frequencies above 300 MHz.

1 Microwave Theory

Microwaves (MWs) represent electromagnetic radiation with wavelengths between 100 cm and 0.1 cm. In terms of frequencies, this range corresponds, in vacuum or air, to 300 MHz – 300 GHz. In an electric circuit, alternating current at such a frequency can also be seen as a wave and thus specific phenomena such as propagation and reflection are present. The wave effects can be ignored when the length scale of the circuit is much smaller than the involved MW wavelength. However, when the circuit size is comparable to the MW wavelength, the usual methods of circuit analysis (precisely, those approaches based on decomposing the circuit in lumped elements) are not effective anymore. One should apply instead the MW circuit theory [35, 36].

1.1. Transmission lines

For the purpose of presenting the manifestation of wave phenomena in circuits, a uniform line or cable comparable to the wavelength of the ac signal it transports is a simple object to start with. Such a line, called transmission line, can be modeled as a ladder network made of identical infinitesimal cells of length dz, comprising an element impedance dZ and an element shunt admittance dY, see fig. 1.1.

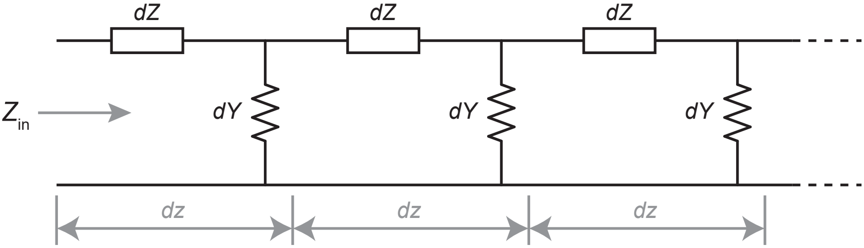

Figure 1.1. A distributed network models well uniform lines, because any infinitesimal segment dz of the line is characterized by an element impedance dZ and an element shunt admittance dY to a reference plane, i.e. ground.

Voltage and current equations can be written for an element cell of the transmission line, see fig. 1.2:

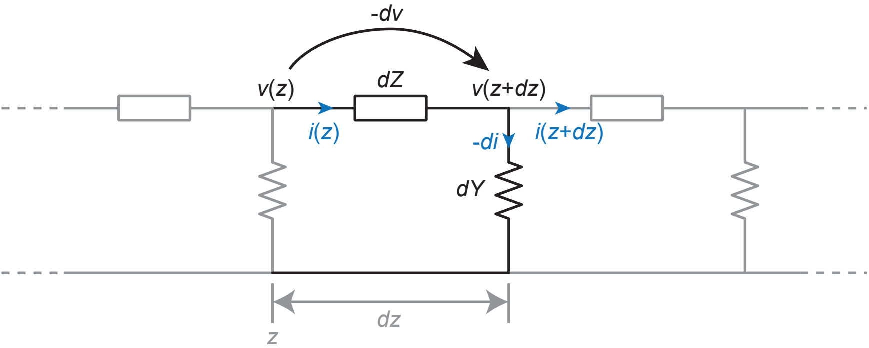

Figure 1.2. Each infinitesimal element of a transmission line produces a voltage reduction, $dv < 0$, and a current leak, $di < 0$.

$$-dv = i(z)dZ, \tag{1.1a}$$

$$-di = v(z+dz)dY, \tag{1.1b}$$

reformulated as:

$$-\frac{dv}{dz} = i(z)\frac{dZ}{dz}, \tag{1.2a}$$

$$-\frac{di}{dz} = v(z)\frac{dY}{dz}. \tag{1.2b}$$

1.1.1. The telegraph equations

Eqs. 1.2a, 1.2b can be processed further, by differentiating (d/dz) each of them and substituting the simple derivative from the other. This way, we obtain wave equations for $v(z)$ and $i(z)$, commonly referred to as the telegraph equations:

$$\boxed{\begin{aligned} \frac{d^2v}{dz^2} &= \gamma^2 \cdot v(z), \quad (1.3a)\\ \frac{d^2i}{dz^2} &= \gamma^2 \cdot i(z), \quad (1.3b)\end{aligned}}$$

with $\gamma = \sqrt{\frac{dZ}{dz} \cdot \frac{dY}{dz}}$ the complex propagation constant for v and i.

Assuming sinusoidal steady-state conditions, one can specify $dZ = dR + j\omega \cdot dL$ and $dY = dG + j\omega \cdot dC$, where ω is the angular frequency of the excitation applied at one end of the line and dR, dL, dG, dC are the resistance, the impedance, the shunt conductance, and the shunt capacitance of the infinitesimal segment transmission line. Notating per-unit-length quantities by the corresponding cursive letter, i.e. $\mathcal{Q} \equiv \frac{dQ}{dz}$ for any quantity Q, the propagation constant reads:

$$\gamma = \sqrt{\mathcal{Z}\mathcal{Y}} = \sqrt{(\mathcal{R} + j\omega\mathcal{L})(\mathcal{G} + j\omega\mathcal{C})}. \tag{1.4}$$

The solutions of the telegraph equations, 1.3a and 1.3b, are:

$$v(z) = v^+(0)e^{-\gamma z} + v^-(0)e^{\gamma z}, \tag{1.5a}$$

$$i(z) = i^+(0)e^{-\gamma z} + i^-(0)e^{\gamma z}. \tag{1.5b}$$

Therefore, the voltage along the line, $v(z)$, is a superposition of a forward wave, $v^+(0)e^{-\gamma z}$, and a backward wave, $v^-(0)e^{\gamma z}$. Similarly for the current along the line, $i(z)$.

The relation between the current and the voltage waves can be extracted by introducing eq. 1.3a in eq. 1.2a: $i(z)\mathcal{Z} = \gamma[v^+(0)e^{-\gamma z} - v^-(0)e^{\gamma z}]$, rewritten as:

$$i(z) = \frac{v^+(0)}{Z_0}e^{-\gamma z} - \frac{v^-(0)}{Z_0}e^{\gamma z}, \tag{1.6}$$

where

$$Z_0 \equiv \sqrt{\frac{\mathcal{Z}}{\mathcal{Y}}}, \tag{1.7}$$

called the *characteristic impedance*, would actually be the impedance of the line if it were semi-infinite. Indeed, if the forward wave never reached the line end in order to reflect and give birth to a backward wave, then $Z_0 = v^+(0)/i^+(0)$ would correspond to the impedance of that endless line.

The time-dependent solutions of the telegraph equations easily emerge from the boundary condition $v^{\pm}(z = 0, t) = V_0^{\pm}e^{j\omega t}$. Hence, eqs. 1.5a, 1.6 are generalized to:

$$\boxed{\begin{aligned} v(z,t) &= V_0^+ e^{-\alpha z} e^{j(\omega t - \beta z)} + V_0^- e^{-\alpha(-z)} e^{j(\omega t + \beta z)}, \\ i(z,t) &= \frac{V_0^+}{Z_0} e^{-\alpha z} e^{j(\omega t - \beta z)} - \frac{V_0^-}{Z_0} e^{-\alpha(-z)} e^{j(\omega t + \beta z)}, \end{aligned}} \qquad \begin{aligned} (1.8a) \\ (1.8b) \end{aligned}$$

where $\alpha = \Re\{\gamma\}$ and $\beta = \Im\{\gamma\}$. Physically, α is the attenuation constant (in both propagation directions) and β the wave number. The speed of the waves is found if considering the movement of a fixed-phase point, i.e. $\frac{d}{dt}(\omega t \mp \beta z) = 0$. Therefore, both the forward and the backward waves travel at a velocity of absolute value:

$$|c| = \frac{\omega}{\beta}. \tag{1.9}$$

1.1.2. The lossless line

An ideal transmission line has no energy losses: $\mathcal{R} = 0$ and $\mathcal{G} = 0$. One consequence is that the propagation constant is imaginary:

$$\gamma = j\omega\sqrt{\mathcal{LC}}. \tag{1.10}$$

It follows that attenuation constant is null, $\alpha \equiv \Re\{\gamma\} = 0$, and the wave number is $\beta \equiv \Im\{\gamma\} = \omega\sqrt{\mathcal{LC}}$. Substituting in eq. 1.9, one explicitly gets the wave velocity:

$$\boxed{|c| = \frac{1}{\sqrt{\mathcal{LC}}}.} \tag{1.11}$$

Another consequence that the characteristic impedance (eq. 1.7) is real:

$$\boxed{Z_0 = \sqrt{\frac{\mathcal{L}}{\mathcal{C}}}.} \tag{1.12}$$

We remind that the impedance of a semi-infinite transmission line is equal to the characteristic impedance, $Z_{\mathrm{in}} = Z_0$. Therefore, a semi-infinite lossless line has a real impedance. We know however that a real impedance is synonym to losses! The apparent paradox is explained by the fact that, although no energy is lost on the way, the current wave conveys energy to infinity. In other words, the loss occurs at $z \to \infty$.

1.1.3. Wave reflections in transmission lines

Having showed the presence of both forward and backward waves in transmission lines, we want to investigate quantitatively how reflections produce backward waves. Intuition can tell us that, like in optics, reflections should occur where the transmission medium ends. We have already used the physical argument that endless (semi-infinite) lines do not exhibit reflections. Here, we investigate what happens at end of the finite transmission line.

Let us terminate a line with an impedance, Z_{L}, that we call load. Fixing the axis origin, $z = 0$, at the interface between the line and the load (see fig. 1.3), one can relate the interface voltage and the current by the relation:

$$v(0) = Z_{\mathrm{L}} \cdot i(0).$$

With v and i provided by equations . 1.8a, 1.8b, we obtain:

$$V_0^+ + V_0^- = \frac{Z_{\mathrm{L}}}{Z_0}(V_0^+ - V_0^-),$$

reformulated as

$$\frac{V_0^-}{V_0^+} = \frac{Z_{\mathrm{L}} - Z_0}{Z_{\mathrm{L}} + Z_0}. \tag{1.13}$$

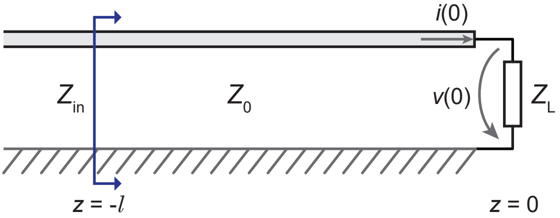

Figure 1.3. Transmission line terminated with a load impedance Z_L. The hashed part represents ground. Z_0 is the characteristic impedance of the line.

We now define the *reflection coefficient* in a point of the transmission line as the amplitude of the reflected voltage wave relative to the amplitude of the forward voltage wave, $\Gamma \equiv V^-/V^+$. The previous equation implies:

$$\boxed{\Gamma_\mathrm{L} = \frac{Z_\mathrm{L} - Z_0}{Z_\mathrm{L} + Z_0}.} \tag{1.14}$$

This means that, at the interface of a transmission line, called TL0, with another circuit element, reflections are generated and their relative strength is given by the total impedance seen from the line side into the interface, Z_L. Here are some applied situations:

- If the transmission line is open at the end, $Z_\mathrm{L} = \infty$, then $\Gamma_\mathrm{L} = 1$. In words, a total reflection occurs.

- If the transmission line is shorted (grounded) at the end, $Z_\mathrm{L} = 0$, then $\Gamma_\mathrm{L} = -1$. This is a total reflection with a phase change of π.

- If the transmission line is terminated with an impedance equal to Z_0, then no reflection occurs: $\Gamma_\mathrm{L} = 0$. This is equivalent to extending the transmission line to infinity.

- If the load is another transmission line, of characteristic impedance Z_1, one could still apply eq. 1.14:
  - If the load transmission line is semi-infinite, then we know that $Z_\mathrm{L} = Z_1$ and the reflection coefficient can be immediately calculated as $\Gamma_\mathrm{L} = \Gamma_1 \equiv (Z_1 - Z_0)/(Z_1 + Z_0)$.
  - We get the same result if the load transmission line is terminated in Z_1.
  - If the load transmission line (TL_1) is terminated in some impedance different from Z_1, then the ends of TL_1 will act as two mirrors. At the beginning, there is only a forward wave in TL_1 and the wave reflected

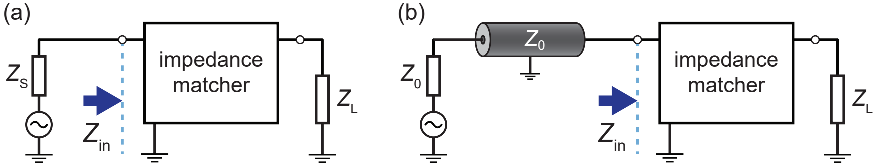

Figure 1.4. **(a)** An impedance matcher, together with a load Z_L, has an impedance $Z_{in} = Z_S$. **(b)** In series with a source impedance Z_0, a transmission line (of characteristic impedance Z_0) is seen from right as a semi-infinite transmission line. The only possible reflections appear at its interface with a load. No reflections occur when the appropriate impedance matcher is placed in between, i.e. $Z_{in} = Z_0$.

into TL_0 is described by Γ_1. Later, the backward wave in TL_1 reaches TL_0 and partially passes into TL_0, strengthening Γ_1; it also partially stays in TL_1, as an extra forward wave. So on and so forth, waves arriving at the termination of TL_1 are reflected, reach later TL_0 and partially pass into TL_0, further enforcing the backward wave in TL_0. Therefore, when loading with a terminated transmission line, $\Gamma_L \geq \Gamma_1$.

1.2. Impedance matching

In microwave circuitry, the lines which connect different elements are modeled as transmission lines. Reflections at their ends decrease the power transferred between elements. In order to minimize reflections and thus maximize the power transfer, special objects are inserted between transmission line ends and circuit elements, such that the impedance perceived by the ends of the transmission lines be equal to their characteristic impedance. These objects are interchangeably called impedance transformers, impedance matchers, impedance-matching networks or impedance-matching circuits.

In the previous section, we have already met the simplest impedance matcher (fig. 1.3): a Z_0 impedance between a short to ground ($0\,\Omega$) and a transmission line of characteristic impedance Z_0. One can easily calculate that this component increases from 0 to 100% the power transfer.

By definition, an impedance matcher transforms a given load impedance Z_L into the source impedance, Z_S. This concept is suggested by fig. 1.4.

1.2.1. *LC* matching networks

Simple, yet effective, impedance matchers are the so-called *LC* matching networks. Two common declinations are presented in fig. 1.5.

Because we are interested in highly ohmic loads, let us analyze the circuit in

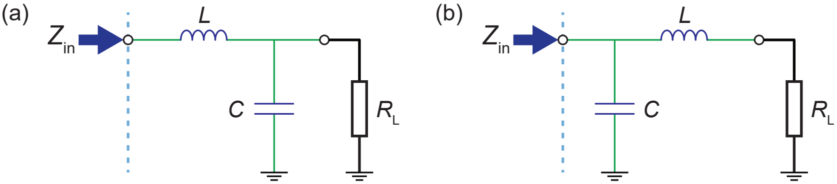

Figure 1.5. Some LC matching networks. **(a)** The source is more resistive than the load: $R_\mathrm{S} = Z_\mathrm{in} > R_\mathrm{L}$. **(b)** The source is less resistive than the load: $R_\mathrm{S} = Z_\mathrm{in} < R_\mathrm{L}$.

fig. 1.5a. If R_S is the resistance of the source as presented in fig. 1.4, then the matching condition is: $R_\mathrm{S} = Z_\mathrm{in}$, with Z_in expressed as $i\omega L + 1/(R_\mathrm{L}^{-1} + i\omega C)$. The imaginary part of the equality, $0 = \Im\{Z_\mathrm{in}\}$, reveals the frequency for which matching occurs:

$$\boxed{\omega_\mathrm{r} = \omega_0\sqrt{1 - Q_\mathrm{L}^{-2}}.} \tag{1.15}$$

Here, we use the notations $\omega_0 = 1/\sqrt{LC}$ and $Q_\mathrm{L} = \omega_0 C R_\mathrm{L}$. If the circuit is not loaded ($R_\mathrm{L} \to \infty$), then $\omega_\mathrm{r} = \omega_0$. Q_L is called the *quality factor* of the loaded circuit. ω_0 is the resonance angular frequency of the unloaded circuit. ω_r is the resonance angular frequency of the loaded circuit.

The real part of the impedance match condition, $R_\mathrm{S} = \Re\{Z_\mathrm{in}\}$, together with eq. 1.15, gives:

$$R_\mathrm{S} R_\mathrm{L} = Z_\mathrm{c}^2, \tag{1.16}$$

where $Z_\mathrm{c} \equiv \sqrt{L/C}$ is the *characteristic impedance* of the LC circuit. Therefore, this type of LC network impedance-matches a load to a source if and only if its characteristic impedance is the geometric mean of the source and the load resistances. When matching to a transmission line like in fig. 1.4b, the LC network of characteristic impedance Z_c matches the load impedance R_match determined by:

$$\boxed{Z_\mathrm{c}^2 = Z_0 R_\mathrm{match}.} \tag{1.17}$$

Hence, if one aims at matching a 50-Ω transmission line to a quantum device of resistance 100 kΩ, at a 3-GHz frequency, with the above LC network (fig. 1.5a), then L and C are easily retrieved using $1/\sqrt{LC} = \omega_0 \approx \omega_\mathrm{r} = 2\pi \cdot 3\,\mathrm{GHz}$ and $L/C = 50\Omega \cdot 10^5\Omega$. The result is: $L = 119\,\mathrm{nH}$ and $C = 24\,\mathrm{fF}$. One can describe this resonator either by the calculated values of L and C or by $\omega_0 = 2\pi \cdot 3\,\mathrm{GHz}$ and $Z_\mathrm{c} = \sqrt{L/C} = 2.24\,\mathrm{k}\Omega$.

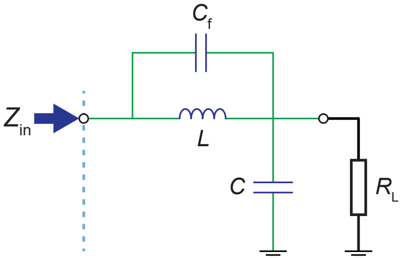

Figure 1.6. An LC matching network characterized and used in this thesis. It presents a *feed-forward* capacitance, C_f, in parallel with the inductor L.

1.2.2. Feed-forward capacitance in impedance transformers

Matching a resistive load is possible also with an LC-network variant in which a *feed-forward* capacitor, C_f, is added in parallel with the existing inductor, L, like in fig. 1.6. This can be the case of a spiral or cylindrical coil with inter-turn capacitance that builds up [9, 37, 38] into an equivalent one, C_f. In this subsection, we show that C_f acts as an inductance booster.

With $Z_\mathrm{in} = 1/[(i\omega L)^{-1} + i\omega C_\mathrm{f}] + 1/(R_\mathrm{L}^{-1} + i\omega C)$, we can repeat the calculation steps of the previous subsection, to extract the resonance frequency and the matched load.

First, we use the imaginary part of the match condition, $0 = \Im\{Z_\mathrm{in}\}$. If the circuit is not loaded, $R_\mathrm{L} \to \infty$, then the resonance frequency is:

$$\omega_{0,\mathrm{f}} = \frac{1}{\sqrt{L(C + C_\mathrm{f})}}. \tag{1.18}$$

The resonance frequency of the loaded circuit is:

$$\omega_{\mathrm{r,f}} = \omega_{0,\mathrm{f}} \sqrt{1 - \frac{1}{R_\mathrm{L}^2}\frac{L}{C}} \tag{1.19}$$

Let us introduce the ration $\chi \equiv C_\mathrm{f}/C$. With the further notations

$$\boxed{L_\mathrm{f} \equiv L(1+\chi) \quad \text{and} \quad Z_{\mathrm{c,f}} \equiv \sqrt{\frac{L_\mathrm{f}}{C}},} \tag{1.20}$$

the real part of the match condition, $Z_0 = \Re\{Z_\mathrm{in}\}$, leads to the equation:

$$\chi + \frac{R_\mathrm{match}}{Z_0} = \frac{R_\mathrm{match}^2}{Z_{\mathrm{c,f}}^2}. \tag{1.21}$$

This equation becomes:

$$\boxed{Z_0 R_{\mathrm{match}} = Z_{\mathrm{c,f}}^2} \quad \text{if } \chi \ll \frac{R_{\mathrm{match}}}{Z_0}, \tag{1.22}$$

similar to eq. 1.17. We can now re-write, without approximations, the resonance frequency of the unloaded circuit (eq. 1.18):

$$\boxed{\omega_{0,\mathrm{f}} = \frac{1}{\sqrt{L_{\mathrm{f}} C}}.} \tag{1.23}$$

In consequence, from the point of view of the resonance frequency and that of the characteristic impedance, the additional capacitance, C_{f}, acts as a booster of the inductance value, $L \to L(1+\chi)$, with $\chi = C_{\mathrm{f}}/C$. As a remark, if $C_{\mathrm{f}} = 0$, then $\chi = 0$ and we retrieve the old values of the circuit parameters, i.e. $L_{\mathrm{f}} = L$, $\omega_{0,\mathrm{f}} = \omega_0$, $Z_{\mathrm{c,f}} = Z_{\mathrm{c}}$.

1.3. The scattering matrix

A microwave (MW) electric circuit is composed of MW components and transmission lines. Such an electric circuit is often modeled as a black box with n ports, i.e. an n-port *network*. A two-port network is presented in fig. 1.7a,b. As shown there, we associate to each port i an incident wave and a reflected one, noted in general with a_i and b_i. When working with voltage waves, we use the notations V_i^+ and V_i^- and define the scattering matrix of the n-port network by its elements,

$$S_{ij} = \left.\frac{V_i^-}{V_j^+}\right|_{V_k^+=0 \ \forall k \neq j}. \tag{1.24}$$

The matrix element S_{ij} regards ports i and j; for the remaining ports, the incident wave is set to zero. Therefore, S_{ij} quantifies how much signal entering port j is transmitted at port i.

If the analyzed network is *reciprocal*, i.e. it behaves identically when inversing the sense of each signal flow, then its scattering matrix is symmetric: $S_{ij} = S_{ji} \Rightarrow S = S^{\mathrm{T}}$. Moreover, if the network is lossless, one can demonstrate that S is *unitary*: $SS^\dagger = \mathbb{1}$.

Every MW component or circuit can be graphically described by a *signal flow graph*, whose arrows are labeled with scattering matrix elements. A signal flow graph example for a two-port network appears in fig. 1.7c.

1.3.1. Modeling defects in signal flow graphs

Although MW circuits are designed such that most of the interfaces are impedance-matched, sometimes unforeseen reflections still appear. We say that unexpected reflections are caused by *defects*. If these reflections interfere with those of the device under test (DUT), then standing waves arise between the defect and the DUT, like in a Fabry-Pérot cavity. Hence, a standing-wave pattern will appear in frequency-dependent measurements. Successful defect modeling can lead to useful data corrections in rf experiments, e.g. calibrations that remove spurious standing-wave patterns.

In the following examples, an electrical distance d is assumed between the DUT and the port to which it is connected. The effective reflection coefficient Γ incorporates the wave traveling from the port to the DUT and back:

$$\Gamma = \Gamma_{\mathrm{DUT}} \cdot e^{-i \cdot 2kd}, \tag{1.25}$$

with $k = \omega/c$. Thus, d is the electrical length of the formed Fabry-Pérot cavity.

The error box

When a DUT is interfaced with a transmission line (TL), the reflection coefficient, $\Gamma(\omega)$, is dictated by the DUT and TL impedances (eq. 1.14). Measuring a response with a different shape from the anticipated $\Gamma(\omega)$ is a defect symptom. A simple model for such a defect is the *error box*, well suited for faulty connectors, presented in fig. 1.7.

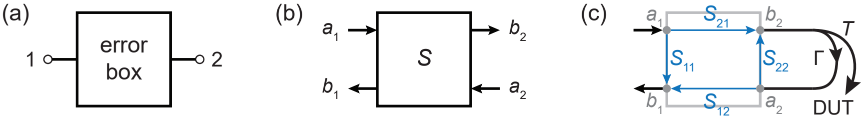

Figure 1.7. **(a)** Symbol for an error box. The ground, common to ports and box, in usually not depicted. **(b)** The signal flow representation considers, for each port i, an incoming wave, a_i, and an outgoing wave, b_i. Their ratios can be grouped in S, the scattering matrix. **(c)** The scattering matrix of the error box, S, defines the signal flow graph of the error box. Port 2 is here connected to a device under test (DUT) that partially reflects (Γ) the signal.

Ref. [39] applies reduction rules for the signal flow graph (fig. 1.7c) in order to obtain an adjusted relation for the reflection coefficient:

$$\Gamma_{\mathrm{measured}} = S_{11} + \frac{S_{21}\Gamma S_{12}}{1 - S_{22}\Gamma}. \tag{1.26}$$

A lossless, reciprocal error box can be described by the real matrix:

$$S = \begin{bmatrix} -\epsilon & \sqrt{1-\epsilon^2} \\ \sqrt{1-\epsilon^2} & -\epsilon \end{bmatrix}, \tag{1.27}$$

with $|\epsilon| < 1$. Using it in eq. 1.26, the altered reflection coefficient reads:

$$\Gamma_{\text{measured}} = \frac{-\epsilon + \Gamma}{1 - \epsilon\Gamma}. \tag{1.28}$$

For $\epsilon = 0$, the error box becomes a perfect connector—that is total, phaseless transmission between ports—and $\Gamma_{\text{measured}} = \Gamma$.

If such a simple model is not successful in the data analysis, it should be replaced by a more specific one. In our case, the error box model opened the way to the model of erroneous directional couplers.

The erroneous directional coupler

Sometimes, an entire microwave part is faulty, for instance when the impedance of its ports is not the nominal one ($50\,\Omega$) at low temperature. The interface with the part is then impedance-mismatched, and undesigned reflections arise at ports. Here, we take the example of a directional coupler (fig. 1.8a). Such a component behaves like an attenuator between input and the *coupled* port; the wave reflected by the coupled port is collected at a distinct, *isolated* port. Its ideal behavior, captured in the signal flow graph of fig. 1.8b, shows null internal reflections: $S_{ii} = 0\ \forall i$.

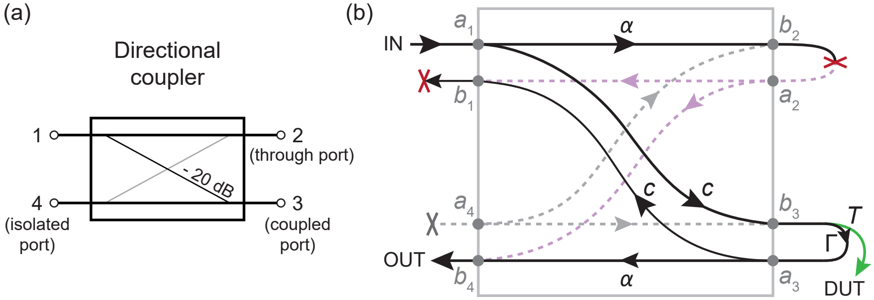

Figure 1.8. **(a)** Symbol of a directional coupler. **(b)** The usual signal flow graph of an ideal directional coupler, that couples an input to a device under test (DUT). The red crosses indicate reflection-suppressing 50Ω terminations, the gray X indicates the lack of an incident wave. Thus, in this configuration, the dashed arrows carry no signal. $c = S_{31}$ is the coupling constant and $\alpha = S_{21}$ is the transmission constant.

Starting with only the *coupling* factor, $c = S_{31}$, we can build the scattering matrix of an ideal directional coupler using its unitarity:

$$S_{\text{ideal}} = \begin{bmatrix} 0 & \alpha & c & 0 \\ \alpha & 0 & 0 & -c \\ c & 0 & 0 & \alpha \\ 0 & -c & \alpha & 0 \end{bmatrix} \tag{1.29}$$

with $|\alpha|^2 + |c|^2 = 1$. A power attenuation of $-20\,\text{dB}$ corresponds to $|c|^2 = 0.01$, thus $|\alpha| \approx 1$. The measured output of the connected directional coupler is the product of the transmission coefficients on the signal path $a_1 b_3 a_3 b_4$ in the signal flow graph of fig. 1.8b:

$$S_{41,\text{connected}} = c\Gamma\alpha \approx c\Gamma. \tag{1.30}$$

An erroneous direction coupler with reflections at the coupled port, $S_{33} = \epsilon$, can be described in the lossless case by the scattering matrix:

$$S' = \begin{bmatrix} -\epsilon & \alpha & c & 0 \\ \alpha & \epsilon & 0 & -c \\ c & 0 & \epsilon & \alpha \\ 0 & -c & \alpha & \epsilon \end{bmatrix} \tag{1.31}$$

with $|\alpha|^2 + |c|^2 + |\epsilon|^2 = 1$. At this point, ϵ propagates into the matrix, due to the imposed lossless character of the hole part. The signal flow graph of this erroneous component, connected to a device, is drawn in fig. 1.9a. The loop

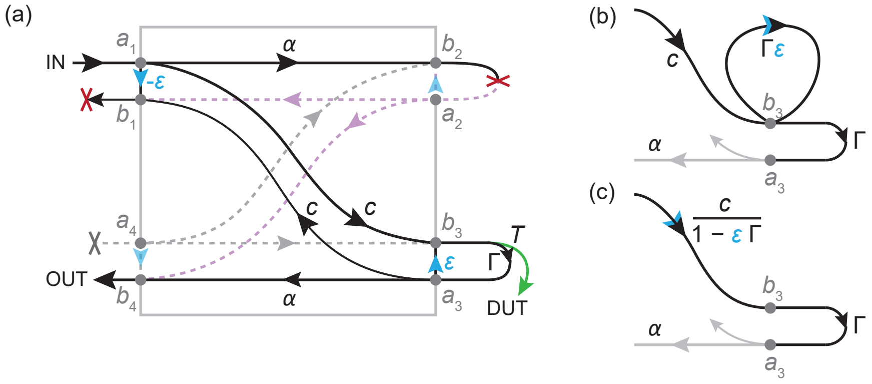

Figure 1.9. **(a)** The signal flow graph of an erroneous directional coupler, with a device under test connected at the coupled port. Like in fig. 1.8b, the dashed arrows carry no signal. $\epsilon = S_{33}$ (in blue) characterizes the unexpected reflection, $c = S_{31}$ is the coupling constant, $\alpha = S_{21}$ is the transmission constant. **(b)** The signal flow graph around port 3 contains a loop. **(c)** Simplification of the signal flow graph around port 3.

present at the coupled port, 3, can be successively reduced like in fig. 1.9b,c. Here, reductions rules were applied [39, 40].

The measured output is the product of the transmission coefficients that label the path shown in fig. 1.9c:

$$S'_{41,\text{connected}} = \frac{c\Gamma\alpha}{1-\epsilon\Gamma} \approx \frac{c\Gamma}{1-\epsilon\Gamma}\sqrt{1-\epsilon^2}, \tag{1.32}$$

where we used the approximation $\alpha \approx \sqrt{1-\epsilon^2}$, because $c^2 \approx 0$. By dividing the output by c, we obtain:

- Γ in the ideal case (from eq. 1.30) or
- a function of Γ (from eq. 1.32) in the case of the faulty directional coupler:

$$\Gamma_{\text{measured}} \approx \frac{\Gamma}{1-\epsilon\Gamma}\sqrt{1-\epsilon^2} = \frac{\Gamma_{\text{DUT}}\cdot e^{-i\cdot 2kd}}{1-\epsilon\Gamma_{\text{DUT}}\cdot e^{-i\cdot 2kd}}\sqrt{1-\epsilon^2}. \tag{1.33}$$

One can now fit the measured curve, $\Gamma_{\text{measured}}(\omega)$, with the formulas arisen from the above defect models, namely with eq. 1.28 and eq. 1.33.

2 Quantum Dots

Quantum dots (QDs) are objects in which charge carriers are confined in all directions, such that their states are quantized. They are also referred to as *artificial atoms* [41–44]. There are many implementations of QDs [45]. One way to make them is to start from objects that already exhibit confinement in two directions, such as nanowires and nanotubes. This thesis considers only carbon nanotube quantum dots.

A single-wall carbon nanotube is a sheet of graphene, i.e. monolayer graphite, rolled on itself such that the resulting cylinder has a nanometer-scale diameter. The movement of electrons is confined in the transversal directions (more precisely, it is subject to periodic boundary conditions in the circumferential direction). In the longitudinal direction, electrons move freely, because the nanotube length is usually much bigger than the diameter: $L \gg d$. However, if the tube is shorter (fig. 2.1a), effects of longitudinal confinement arise.

A multi-wall carbon nanotube is a structure of several concentric single-wall nanotubes. We restrain ourselves to single-wall carbon nanotubes.

In a carbon nanotube quantum dot, two electrical contacts to the nanotube are placed at a small distance ($L \sim 500\,\mathrm{nm}$), in order to establish electron confinement in the longitudinal direction, too—see fig. 2.1b. Not shown in the figure, an electric gate is commonly added to the quantum dot, in order to tune its electrochemical potential.

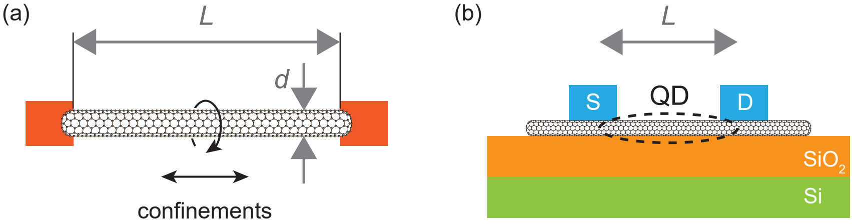

Figure 2.1. **(a)** Carbon nanotube; the electron movement is confined, more strongly in the circumferential direction and less in the longitudinal one. **(b)** Quantum dot made by placing electric contacts, i.e. source (S) and drain (D), at a relatively small distance. If doped, the entire Si layer could act as a bottom gate.

2.1. The structure of the carbon nanotube

The properties of carbon nanotubes are derived from those of graphene and are enriched by confinement effects.

If we do the mental exercise of unfolding a carbon nanotube, we get a sheet of graphene (fig. 2.2a). On the unfolded circumference lies the chiral vector of the nanotube, $\mathbf{C} = n\mathbf{a}_1 + m\mathbf{a}_2$. Here, $\mathbf{a}_1$ and $\mathbf{a}_2$ are the graphene lattice vectors. The indices n and m are integers whose values determine the properties of the carbon nanotube. For a summary of the structure parameters of the (n, m) nanotube, see table I in [46].

As illustrated in fig. 2.2b, the band structure of graphene is gapless in the so-called *Dirac points*, where the conductance and valence bands form the *Dirac cones*, that describe linear energy dispersion. The Dirac points are the vector momenta $\mathbf{K}$ and $\mathbf{K}'$ in the reciprocal lattice (fig. 2.2c) where the valence and the conductance bands touch. Locally, the energy dispersion writes:

$$\boxed{E = \pm\hbar v_{\mathrm{F}}\kappa,} \tag{2.1}$$

with $\boldsymbol{\kappa} = \mathbf{k} - \mathbf{K}$ or $\boldsymbol{\kappa} = \mathbf{k} - \mathbf{K}'$ and $\kappa \ll K$. Here, v_{F} is the Fermi velocity and takes values around 8×10^5 m/s, both in graphene and carbon nanotubes [46].

In carbon nanotubes, the circumferential confinement imposes discrete values for the transverse component of the momentum:

$$\mathbf{kC} = (K_\perp + \kappa_\perp)\pi d \quad = \quad 2p\pi, \qquad p \in \mathbb{Z}. \tag{2.2}$$

After the geometric calculation of $K_\perp$, this equation leads to the discrete values:

$$\boxed{\kappa_{\perp,p} = \frac{2}{d}\left(\frac{n-m}{3} + p\right)} \quad p \in \mathbb{Z}. \tag{2.3}$$

To exemplify, fig. 2.2c shows in blue lines the spectrum of allowed chiral momenta, $\kappa_{\perp,p}$, for the chiral indices $n = 4$ and $m = 2$.

The Dirac points, $\mathbf{K}$ and $\mathbf{K}'$, are possible momenta in the nanotube if $n = m \bmod 3$, because in this case the minimal value of the $|\boldsymbol{\kappa}|$ is $\kappa_\perp^{\min} = 0$. If so, the bandstructure is gapless, therefore the nanotube is metallic (fig. 2.2d). Its first subbands are still described by eq. 2.1.

The band structure is formed by the p-parametrized hyperbolas:

$$E_p^{\pm}(\kappa_\parallel) = \pm\hbar v_{\mathrm{F}}\sqrt{\kappa_\parallel^2 + \kappa_{\perp,p}^2}, \quad p \in \mathbb{Z}. \tag{2.4}$$

If the Dirac point is missed by the $\kappa_{\perp,p}$ spectrum, then $n - m = \pm 1 \bmod 3$, hence $\kappa_\perp^{\min} = 2/3d$. A gap is present and the nanotube is semiconducting (fig. 2.2d). The first set of subbands of the semiconducting nanotube are the hyperbolas:

$$\boxed{E^{\pm}(\kappa_\parallel) = \pm\sqrt{\hbar^2 v_{\mathrm{F}}^2 \kappa_\parallel^2 + E_{\mathrm{g}}^2/4},} \tag{2.5}$$

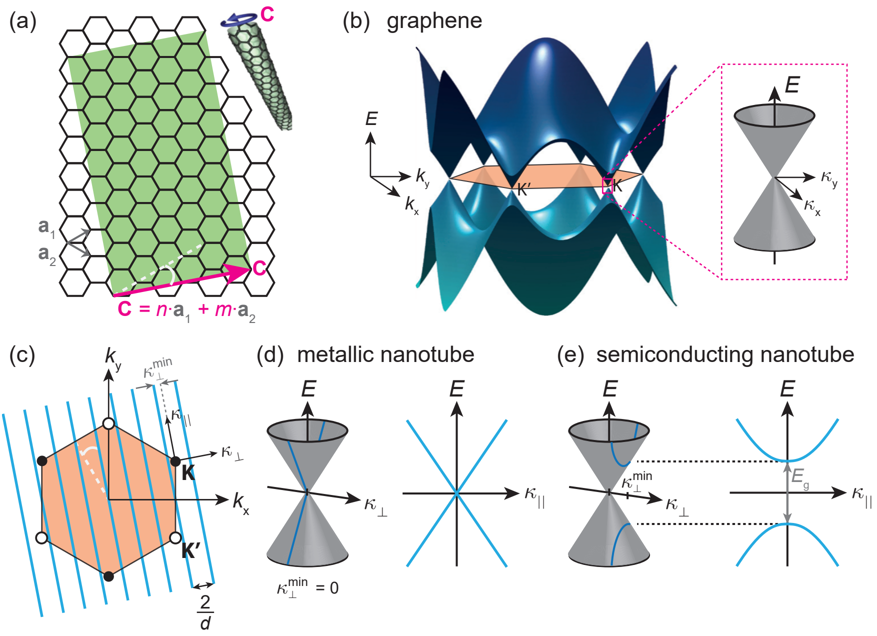

Figure 2.2. **(a)** By unfolding a carbon nanotube, one obtains a sheet of graphene, i.e. a 2D honeycomb lattice of carbon atoms. The chiral vector, **C**, corresponds to the unfolded circumference. Adapted from [46], inspired by [47]. **(b)** The energy band structure of graphene exhibits *Dirac* cones that close the gap between the upper, conductance band and the bottom, valence band. The dispersion $E(\mathbf{k})$ is locally linear. **(c)** The first Brillouin zone of graphene upon which overlay, as blue lines, the discrete chiral momenta, $\kappa_\perp$, of the $(n, m) = (4, 2)$ carbon nanotube. (d, e) The dispersion curves, $E(\kappa_\|)$, of a nanotube consist of the cuts made in a Dirac cone by the allowed chiral momenta, $\kappa_\perp$. **(d)** The nanotube is metallic when the chiral momentum may be null. **(e)** When the chiral momentum takes only finite values, a gap is present, and the nanotube is semiconducting. Adapted from [46].

with the energy gap $E_\mathrm{g} = 2\hbar v_\mathrm{F}\kappa_\perp^\mathrm{min} = 4\hbar v_\mathrm{F}/3d \approx 0.7\,\mathrm{eV}/d\,[\mathrm{nm}]$ inversely proportional to the nanotube diameter, d. One can further observe that eq. 2.3 can be re-written here as $\kappa_{\perp,p} = 2(\pm 1 + 3p)/3d$ with $p \in \mathbb{Z}$. It follows from eq. 2.4 that the subbands of the semiconducting nanotube are the p-parametrized hyperbolas $|E_p(\kappa_\|)| = \sqrt{\hbar^2 v_\mathrm{F}^2 \kappa_\|^2 + E_\mathrm{g}^2(3p \pm 1)^2/4}$, $p \in \mathbb{N}$.

The equations of this section refer to free-standing carbon nanotubes, where only chiral confinement os present. However, in a carbon nanotube with electrical contacts (i.e. a QD) lateral confinement effects arise in addition. These effects are treated in the next section.

2.2. Quantum dots in CNTs: confinement energy and Coulomb interaction

By design, carbon nanotube quantum dots have a relatively short length between contacts, $L < 1\,\mu\text{m}$, and therefore longitudinal quasimomentum, $k_\parallel$, is quantized. Indeed, the contacts can confine the charge carriers like hard walls [48], hence the effective length of the nanotube becomes L. In this case, one can write:

$$k_{\parallel,s} \cdot L = s\pi, \quad s \in \mathbb{N} \setminus \{0\}. \tag{2.6}$$

This quantization relation writes for the **K** valley as $K_\parallel + \kappa_{\parallel,q} = s\frac{\pi}{L}$. In the particular case where $K_\parallel$ can be sliced into an integer number of π/L, it results a discrete spectrum for the parallel momenta neatly expressed as:

$$\boxed{\kappa_{\parallel,q} = q\frac{\pi}{L}} \quad q \in \mathbb{Z}. \tag{2.7}$$

This is shown in fig. 2.3 with orange lines, cutting also through **K** (and consequently **K′**) points[1]. The longitudinal-momenta spacing (i.e. the distance between two consecutive orange cuts) is $\Delta\kappa_\parallel = \Delta k_\parallel = \pi/L$.

Of course, the cuts of the perpendicular momenta do not necessarily hit **K** and **K′**, as implied in eq. 2.7. Nonetheless, this simplification helps the purpose of sketching a possible energetic model of the QD.

Let us see further how the longitudinal quantization has an effect on the dispersion curve already depicted in fig. 2.2e. The $\frac{\pi}{L}$-spaced last cuts, applied onto the dispersion curve, impose a discrete energy spectrum (fig. 2.3b). This corresponds to one of the two Dirac points, e.g. **K**. Every level in each of the two branches (branch degeneracy) can be filled with two electrons of different spins (spin degeneracy). The reduced dimensions of a quantum dot enhance the Coulomb interaction between charge carriers. If, for the sake of simplicity, we consider each pair of two electrons in the dot amounts for an effective charging energy, U_c, then the fourfold degeneracy[2] is lifted, as in the zoom of fig. 2.3b.

The energy spectrum (eq. 2.5) in a carbon nanotube quantum dot becomes, for the lowest conductance subband, is composed by the one-electron energies:

$$E_{q,l} = E(\kappa_{\parallel,q}) + (N_q + l) \cdot U_\text{c} = \sqrt{\hbar^2 v_\text{F}^2 \kappa_{\parallel,q}^2 + E_\text{g}^2/4} + (N_q + l) \cdot U_\text{c}, \tag{2.8}$$

---

[1] The Dirac points, **K** and **K′**, are cut if for instance the angle drew in white is null (so-called *zigzag* nanotubes, i.e. $m = 0$).

[2] A supplementary degeneracy is the *valley* one, **K**-**K′**, like in graphene. Magnetically lifted in semiconducting nanotubes [46], it manifests itself in clockwise and anticlockwise movement of electrons around the nanotube, resulted from same-value, opposite-sign perpendicular momenta $\kappa_\perp = \pm\kappa_\text{min} \neq 0$ in **K** and **K′** respectively. It can also be destroyed in valley mixing, produced by defects or contacts [49]. Otherwise, valley degeneracy brings the total degeneracy to $2^3 = 8$, as analyzed in [50].

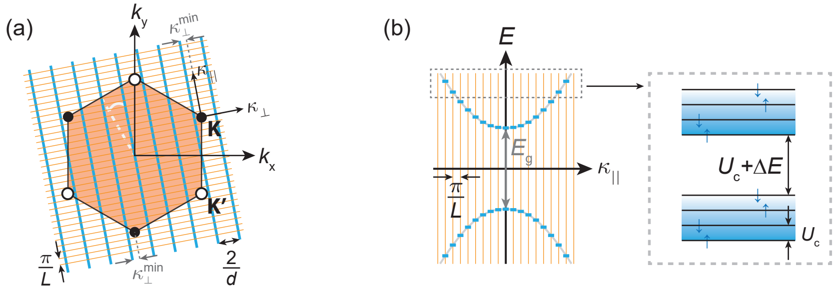

Figure 2.3. **(a)** First Brillouin zone of graphene above which blue and orange lines mark the discrete chiral and longitudinal momenta, $\kappa_\perp$ and $\kappa_{||}$, in a carbon nanotube or a carbon nanotube quantum dot. d is the nanotube diameter and L is the length of the nanotube or quantum dot. Partially adapted from [46]. **(b)** The dispersion relation, $E(\kappa_{||})$, takes into account the quantization of the longitudinal momentum, $\kappa_{||}$. It does not account for Coulomb interaction. Zoom: Coulomb interaction lifts the fourfold degeneracy of the energy levels. U_c is an effective charging energy, accounting for the interaction between two electrons. Only one subband is illustrated. Suggested by [51].

with N_q is the number of electrons in shells $1...q$ and $l \in \{0, 1, 2, 3\}$ is the index of each electron in shell q. This relation also expresses the fact that a charging energy of $N_q U_\text{c}$ shifts up the energies of each shell.

Farther from the Dirac point or in metallic nanotubes, the momentum $\boldsymbol{\kappa} = \mathbf{k} - \mathbf{K}$ consists mainly of its parallel component ($\hbar v_\text{F} \kappa_{||,q} \gg E_\text{g}/2$), hence the dispersion eq. 2.5 is linear ($E(\kappa_{||}) \approx \pm\hbar v_\text{F} \kappa_{||}$) and the *lateral-confinement energy spacing* of the quantum dot, $\Delta E \equiv E(\kappa_{||,q+1}) - E(\kappa_{||,q})$, reads:

$$\boxed{\Delta E \approx \hbar v_\text{F} \Delta\kappa_{||} = \hbar v_\text{F} \frac{\pi}{L}.} \tag{2.9}$$

Therefore, the quantum dot longitudinal modes in the linear-dispersion limit, also known as the massless-electron limit, are equally spaced in energy.

The opposite limit, i.e. the massive-electron limit [46], describes the region closer to the Dirac point in semiconducting nanotubes. It is mathematically defined by the relation $\hbar v_\text{F} \kappa_{||,q} \ll E_\text{g}/2$, that in conjunction with eq. 2.7 leads to a shell-dependent mode spacing:

$$\boxed{\Delta E_q = \frac{1}{E_\text{g}} \left(\hbar v_\text{F} \frac{\pi}{L}\right)^2 (2q+1)} \; q \in \mathbb{Z}. \tag{2.10}$$

With this possible configuration, we can now develop the constant-interaction model for the carbon nanotube quantum dot with a fourfold degeneracy. Nonetheless, a more complete description of such systems should go into the details of momentum quantization cuts in nanotubes [52]. One applied example for the general case $K_\parallel \neq n\frac{\pi}{L}$ is the metallic nanotube measured in [53].

2.3. The constant-interaction model and the QD capacitance model

The well-established constant-interaction model (CIM) supposes that the interaction between any two electrons of the system is the constant $U_\mathrm{c} = e^2/C$, with C called the *self-capacitance* of the system. CIM was already used in eq. 2.8 without being explicitly named. This subsection presents the CIM implications within the quantum dot capacitance model.

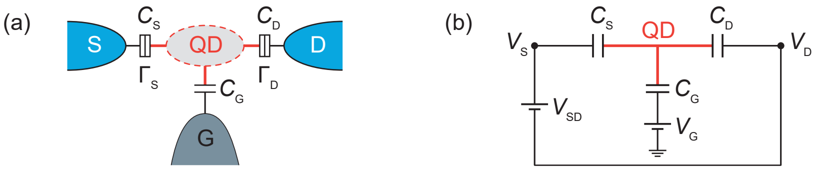

Figure 2.4. **(a)** The capacitance model of quantum gate with one gate. **(b)** The equivalent electrical circuit. Negative charges are indicated on the QD island. The voltage reference point (the ground) can be placed anywhere, e.g. at V_D.

Presented in fig. 2.4, the capacitance model of the quantum dot connects the dot to the source, the drain, and the gate through capacitances: C_S, C_D, C_G. If more gates are present, then each one will be ascribed its own capacitance. The particularity here is that charge can leak through capacitors C_S and C_D, by means of tunneling, i.e. resistors in parallel with the concerned capacitors. Hence, the quantum dot is a charged island, as schematized in fig. 2.4b, and its charge corresponds to N electrons: $Q = -|e|N$. One can partition this QD charge into contributions from the above capacitors:

$$Q = -|e|N_0 + C_\mathrm{S}(V_\mathrm{QD} - V_\mathrm{S}) + C_\mathrm{D}(V_\mathrm{QD} - V_\mathrm{D}) + C_\mathrm{G}(V_\mathrm{QD} - V_\mathrm{G}), \qquad (2.11)$$

with N_0 the number of electrons on the dot island when $V_\mathrm{S} = V_\mathrm{D} = V_\mathrm{G} = 0$. Without the N_0 term, the previous equation would not necessarily hold anymore if the voltage reference were reassigned. The dot voltage as a function of its charge and the surrounding voltages results from eq. 2.11:

$$V_\mathrm{QD} = \frac{1}{C}\left(Q + |e|N_0 + \sum_i C_i V_i\right), \quad i = \mathrm{S}, \mathrm{D}, \mathrm{G}, \qquad (2.12)$$

where $C = C_\mathrm{S} + C_\mathrm{D} + C_\mathrm{G}$ is the self-capacitance of the quantum dot island. By integrating between $Q = 0$ and $Q = -|e|N$, one gets the total charging energy of the QD:

$$U_{\mathrm{c,tot},N} = \int_0^{-|e|N} V_{\mathrm{QD}} \cdot dQ = \frac{e^2N^2}{2C} - \frac{e^2N_0N}{C} - |e|N\sum_i \frac{C_i}{C}V_i, \tag{2.13}$$

with $i \in \{\mathrm{S,D,G}\}$.

The total energy of the quantum dot charged with N electrons is the sum of their single-particle energies and the total charging energy:

$$E_{\mathrm{tot},N} = \sum_{n=1}^{N} E_n + U_{\mathrm{c,tot},N}, \tag{2.14}$$

with $E_n = E(\kappa_{\|,q(n)})$ the confinement energies of the electrons. By this equation, we assume that charging has no effect on the quantum spectrum generated by confinement. Of course, this equality is equivalent to a summation over eq. 2.8.

The electrochemical potential is the energy paid for adding an electron to the quantum dot:

$$\mu_N \equiv E_{\mathrm{tot},N} - E_{\mathrm{tot},N-1} \tag{2.15a}$$

$$= E_N + \frac{e^2}{C}\left(N - \frac{1}{2} - N_0\right) - |e| \sum_{i=\mathrm{S,D,G}} \frac{C_i}{C}V_i. \tag{2.15b}$$

Thus, we obtained an electrochemical potential in which the charging component is linear in N. Using the notation $U_{\mathrm{c}} = e^2/C$, we deduce, for a large number of electrons, $N \gg N_0 + 1/2$:

$$\boxed{\mu_N \approx E_N + NU_{\mathrm{c}} - |e|\frac{C_{\mathrm{G}}}{C}V_{\mathrm{G}} - |e|\frac{C_{\mathrm{S}}}{C}V_{\mathrm{S}} - |e|\frac{C_{\mathrm{D}}}{C}V_{\mathrm{D}}.} \tag{2.16}$$

We observe in this expression that the leads (S and D) act as gates, too. If the drain is grounded, then eq. 2.16 simplifies to:

$$\mu_N \approx E_N + NU_{\mathrm{c}} - |e|\frac{C_{\mathrm{G}}}{C}V_{\mathrm{G}} - |e|\frac{C_{\mathrm{S}}}{C}V_{\mathrm{SD}}, \quad \text{with} \quad V_{\mathrm{D}} = 0. \tag{2.17}$$

2.3.1. Gating a QD

The expression of the QD electrochemical potential, μ_N, in the framework of the constant-model interaction (eq. 2.16) shows that the level of μ_N can be electrostatically controlled, at constant source and drain potentials, by a gate voltage. Fig. 2.5a presents two diagrams, differing by the level of the QD chemical potential. This is lowered by increasing the gate voltage, V_{G}.

An electron can tunnel into the QD if its removal from the contact can pay the energy increase in the QD, e.g. $\mu_{\mathrm{S}} \geq E_{\mathrm{tot},N+1} - E_{\mathrm{tot},N} = \mu_{N+1}$. Therefore, the energy condition for tunneling does not directly involve the energy levels of the two sides of the tunnel barrier, but their respective electrochemical-potential values. Another example: losing an electron of the QD to one contact, e.g. to the drain, needs $\mu_{N+1} \geq \mu_{\mathrm{D}}$. We say a transition $N \leftrightarrow N+1$ is in the bias window if both tunneling-in and -out conditions are met, e.g. $\mu_{\mathrm{S}} \geq \mu_{N+1} \geq \mu_{\mathrm{D}}$. In conclusion, for a current to flow between the two leads of the QD, at least one transition, i.e. a QD chemical-potential level, has to be in the bias window.

The situations presented in fig. 2.5a are created by gate voltage increase that brings a level, μ_{N+1}, in *resonance* with the source, then fully in the bias window, and ultimately in resonance with the drain. The current is expected to sharply increase first, then remain relatively stable, and finally suddenly decrease[3]. By gating further the QD, many other states can be brought in resonance with leads or deeper into the bias window.

The spacing between two consecutive electrochemical-potential levels in the QD is called the *addition energy*, E_{add}. According to eq. 2.16, at a given gate voltage the addition energy is:

$$E_{\mathrm{add}} \equiv \mu_{N+1} - \mu_N = U_{\mathrm{c}} + \delta E, \tag{2.18}$$

where δE is either 0 or the inter-shell spacing ΔE from eq. 2.9 or eq. 2.10: $\delta E|_{N=4q} = \Delta E$ each time that a shell q is filled with its four electrons, in the above fourfold-degeneracy assumption. Therefore, the addition energy sweeps the sequence:

$$\ldots,\ U_{\mathrm{c}},\ U_{\mathrm{c}},\ U_{\mathrm{c}},\ (U_{\mathrm{c}}+\Delta E),\ U_{\mathrm{c}},\ U_{\mathrm{c}},\ U_{\mathrm{c}},\ (U_{\mathrm{c}}+\Delta E),\ \ldots \tag{2.19}$$

The last situation of fig. 2.5a indicates the addition energy $\mu_{N+2} - \mu_{N+1} = U_{\mathrm{c}} = e^2/C$.

2.3.2. Coulomb diamonds

We now understand that, in a plane defined by the gate and the bias voltages, V_{G} and V_{SD}, regions of finite current alternate with regions of no current. We have seen that, at the borders of these regions, the QD chemical-potential level is in resonance with one of the leads. We can find out the geometry of these regions in the $(V_{\mathrm{G}}, V_{\mathrm{SD}})$ plane by determining the aspect of their borders. Recall that the source and drain electrochemical potentials are $-|e|V_{\mathrm{S}}$ and $-|e|V_{\mathrm{D}}$. Let us assume again that $V_{\mathrm{D}} = 0$, thus $V_{\mathrm{S}} = V_{\mathrm{SD}}$.

First, we observe that the borders are described by eq. 2.17 and they intersect on the gate voltage axis ($-|e|V_{\mathrm{SD}} = -|e|V_{\mathrm{D}} = 0$) in the points $V_{\mathrm{G},N}$ defined by:

$$0 = E_N + NU_{\mathrm{c}} - |e|\frac{C_{\mathrm{G}}}{C}V_{\mathrm{G},N}. \tag{2.20}$$

---

[3] However, current at resonance is not a δ function, but is smoothened by temperature [54] (which empties some states below the Fermi level of the lead and occupies other states above) and Γ-broadening [34] (due to Heisenberg's principle, tunneling can occur from one chemical-potential level in the lead to a more energetic one in the QD and vice versa).

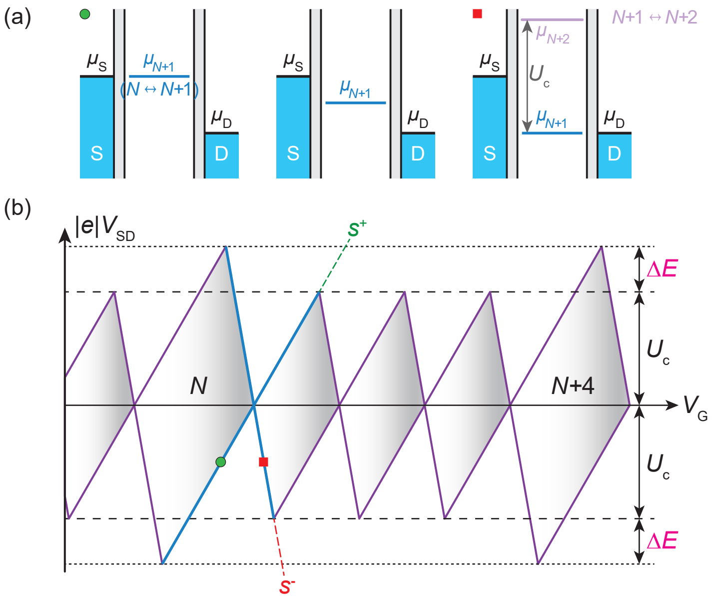

Figure 2.5. (a) Electrochemical-potential diagrams of a quantum dot. $\mu_S = -|e|V_S$ and $\mu_D = -|e|V_D$ are the chemical potential of the leads. μ_{N+1} is the chemical potential of the dot when charged with N electrons. The middle diagram indicates a transition in the bias window; the lateral diagrams depict the same transition in resonance with one of the leads. **(b)** Coulomb diamonds in a generic charge stability diagram. The blue lines depict the QD transition $N \leftrightarrow N+1$ resonant with the source (positive slope, s^-) or with the drain (negative slope, s^+). On these lines, the green circle and the red square mark situations illustrated in (a).

These intersection points, spaced by the addition energies of eq. 2.18, are the only points of finite current at zero bias voltage.

Then, their space variation is dictated by the differentiation of eq. 2.17, $-d\mu_N = |e|\frac{C_G}{C}dV_G + |e|\frac{C_S}{C}dV_{SD}$, applied to source or drain resonances. Starting in $(0, V_{G,N})$, resonances of the QD with the source, i.e. $\mu_N = -|e|V_S = -|e|V_{SD}$, draw $dV_{SD} = \frac{C_G}{C}dV_G + \frac{C_S}{C}dV_{SD}$, that is climbing on a straight line of slope

$$s^+ = \frac{dV_{SD}}{dV_G} = \frac{C_G}{C - C_S}. \tag{2.21}$$

Resonances of the QD with the drain, i.e. $\mu_N = -|e|V_D = 0$, sketch the variation $0 = \frac{C_G}{C}dV_G + \frac{C_S}{C}dV_{SD}$, which is sliding on a straight line of slope

$$s^- = \frac{dV_{SD}}{dV_G} = -\frac{C_G}{C_S}. \tag{2.22}$$

Sets of straight lines of positive and negative slopes, s^+ and s^-, originating in the same points, $(0, V_{\mathrm{G},N})$ from eq. 2.20, define a sequence of diamonds, like in fig. 2.5b. They are termed *Coulomb diamonds*. Inside any of them, no current can flow, because no QD chemical-potential level resides in the bias window. This phenomenon is called *Coulomb blockade*. Outside the diamonds and on their edges, current can flow. The edges are characterized by a finite differential conductance, $dI/dV_{\mathrm{SD}} \neq 0$.

Two consecutive Coulomb diamonds are regimes of consecutive QD charges. Because of that, the kind of $(V_\mathrm{G}, V_{\mathrm{SD}})$ map we have elaborated is usually addressed as *charge stability diagram*.

2.3.3. Excited states

We showed that the energy of one electron on the quantum dot can be divided into two parts: the confinement energy and the contribution of the electron in the charging energy. If one electron is excited to the next possible single-particle state, by receiving the amount ΔE (eq. 2.9 or eq. 2.10), then the quantum dot entirely is in an excited state. In this thesis, we commonly say that the QD went from ground state $|N\rangle$ to excited state $|N^*\rangle$, where N is the number of electrons on the dot. Subsequent excited states are marked by multiple stars, e.g. $|N^{**}\rangle$.

Other quantum dot energy models too include the possibility of excited states.

The following graphical construction helps placing excited states on chemical-potential diagrams and charge stability diagrams. To start, fig. 2.6a draws the energy levels (horizontal lines) and possible transitions between them. Each sketched transition (a vertical arrow) between two states $|N\rangle$ and $|M\rangle$ that differ by one electron represents the spacing energy $\mu_{N\leftrightarrow M} = |E_N - E_M|$, already referred to as chemical potential. We order these transitions in fig. 2.6b. The result of their ordering is fig. 2.6c, showing the chemical-potential diagram of the QD.

We have just illustrated how the existence of a QD excited state generates new possible transitions, adding several *excited levels* in the electrochemical-potential diagram. Fig. 2.6c exemplifies two possible transitions in the case of the excited state $|N^*\rangle$: transition $N-1 \leftrightarrow N^*$ is located at ΔE above $N-1 \leftrightarrow N$; another transition, namely $N^* \leftrightarrow N+1$, is located at ΔE below $N \leftrightarrow N+1$. Other additional levels could arise in the chemical-potential diagram, illustrating transitions between $|N^*\rangle$ and excited states of charge N or $N+1$.

In charge stability diagrams, new source- and drain-resonant lines appear due to excited states, see fig. 2.6d. Such *excited lines* exist only at bias voltages that can provide the excitation energy:

$$|eV_{\mathrm{SD}}| \geq \Delta E \tag{2.23}$$

for the first excited state. If the shells are equidistant, this condition becomes $|eV_{\mathrm{SD}}| \geq n \cdot \Delta E$ for the n^{th} excited state, $n \in \mathbb{N} \setminus \{0\}$. It is however common to

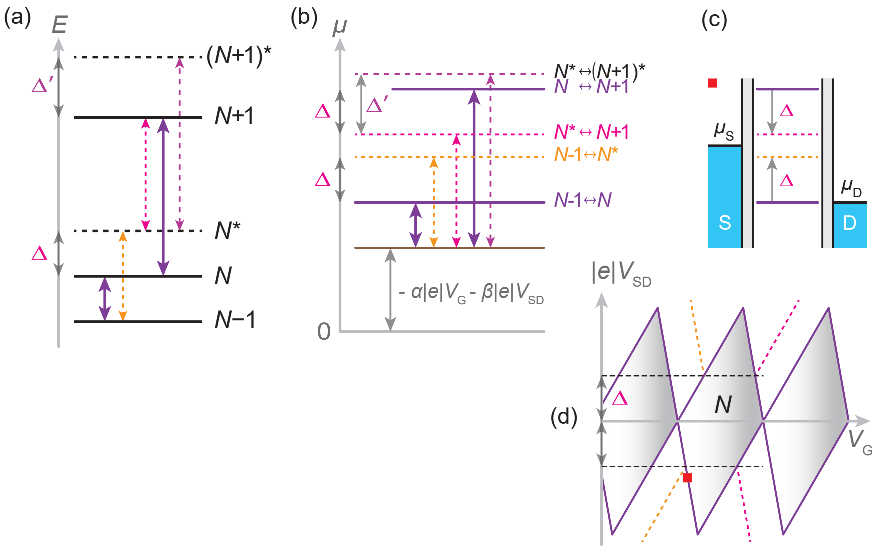

Figure 2.6. **(a)** Energy diagram of a quantum dot with a possible selection of excited states: $|N^*\rangle$, $|(N{+}1)^*\rangle$. Their excitation energies are Δ, Δ'. Transitions between states are marked with vertical arrows. **(b)** The electrochemical-potential levels are obtained by standing on a common base the transitions arrows of the energy diagram in (a). At fixed source and drain voltages, the common-base height is dictated by the gate voltage. **(c)** The electrochemical-potential diagram respects the levels determined in (a). We observe here two *excited levels*, i.e. $N-1 \leftrightarrow N^*$ and $N^* \leftrightarrow N+1$. The level of the $N^* \leftrightarrow (N+1)^*$ transition is omitted. **(d)** On a charge stability diagram, the *excited lines* intersect the Coulomb diamonds at a bias voltage that provides the excitation energy: $|e|V_{\mathrm{SD}} = \pm\Delta$. Here, the orange lines correspond to the lead-resonant transition $N-1 \leftrightarrow N^*$ and the red ones to $N^* \leftrightarrow N+1$, like the excited levels in (b), (c). Each line should be prolonged in the region of opposite-sign bias and sufficient lead chemical potential ($|eV_{\mathrm{SD}}| \geq \Delta$).

observe excited lines which are not equally spaced, suggesting that shells are not equidistant.

2.4. Quantum dot tunneling

In a quantum dot, a continuous flow of electrons appears if tunneling into the QD from one contact is followed or accompanied by tunneling out into the other contact. To this process family belong sequential tunneling on one hand and cotunneling on the other hand.

2.4.1. Sequential tunneling

If a transition, i.e. an electrochemical-potential level, is in the bias window $\mu_S - \mu_D$, then the QD can be filled from one lead and it empties into the other one, sequentially.

First, we can easily see for a given point (V_G, V_{SD}) on a charge stability diagram what transitions are in the bias window. If the point is below both or above both the source-resonant and drain-resonant lines of a transition A $\leftrightarrow$ B, then transition A $\leftrightarrow$ B is in the bias window. For example, the stared point in fig. 2.7a is below both the source- and drain-resonant lines of $N \leftrightarrow N+1$, therefore this transition is included in the bias window. We call the region lying below or above both resonant lines of a transition *the cone* of that transition.

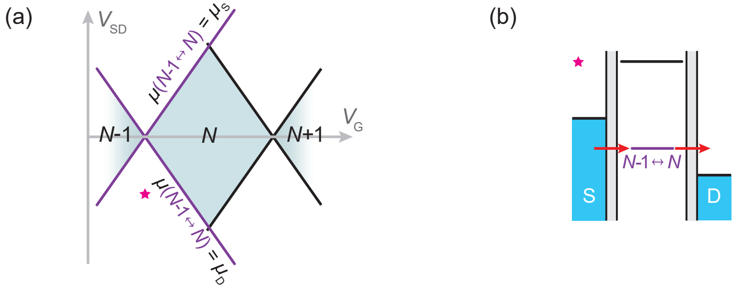

Figure 2.7. **(a)** The stared point is inside the vertical cone of transition $N \leftrightarrow N+1$, in purple. **(b)** Sequential tunneling for the stared point in (a).

Then, on a chemical-potential diagram, we can visualize the sequential-tunneling process that uses a transition contained in the bias window. Hence, in fig. 2.7b, the following tunneling sequence takes place:

$$N-1 \;\rightarrow\; N \;\rightarrow\; N-1 \;\rightarrow\; \ldots$$

In conclusion, if a point (V_G, V_{SD}) is in the cone of a transition, then the transition level is in the bias window and electrons sequentially tunnel through that level.

Inside Coulomb diamonds, there is no transition in the bias window, unless excited lines are present. That is why sequential tunneling is not present in the Coulomb blockade.

2.4.2. Elastic cotunneling

Cotunneling is a process in which an electron tunnels from one lead into the QD and quasi-simultaneously another electron or the same tunnels out of the QD into the other lead. Thus, cotunneling is a second-order process. It does not change the charge of the QD.

When cotunneling leaves the QD state unchanged, it is called *elastic*. Elastic tunneling is possible at any bias voltage. This means even Coulomb diamonds exhibit a relatively small current, due to elastic tunneling.

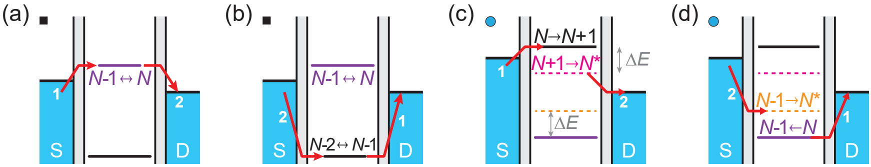

Figure 2.8. **(a)** Elastic cotunneling trough virtual state $|N\rangle$. The 'first' transition is $N-1 \to N$, the 'second' is $N \to N-1$. **(b)** Elastic cotunneling trough virtual state $N-2$. The 'first' transition is $N-1 \to N-2$, the 'second' is $N-2 \to N-1$. **(c)** Inelastic tunneling through virtual state $|N+1\rangle$. The 'first' transition is $N \to N+1$, the 'second' is $N+1 \to N^*$. **(d)** Inelastic tunneling through virtual state $|N\rangle$. The 'first' transition is $N \to N-1$, the 'second' is $N-1 \to N^*$.

The QD state reached for a very short time during the cotunneling process is termed *virtual state*. An example of elastic tunneling is given in fig. 2.8a,b for a QD in state $|N-1\rangle$. Here, the virtual state is either $|N\rangle$ or $|N-2\rangle$.

2.4.3. Inelastic cotunneling

When cotunneling excites or relaxes the quantum dot, it is called *inelastic*. Exciting inelastic tunneling is possible only when the bias voltage is large enough to provide the excitation energy (eq. 2.23). If the cotunneling process that relaxes excited QD, no minimum bias voltage is needed.

Examples of inelastic tunneling are given in fig. 2.8c,d. Here, the initial state of the QD is $|N\rangle$ and the final one is $|N^*\rangle$. The virtual state is $|N-1\rangle$ in fig. 2.8c and $|N\rangle$ in fig. 2.8d.

2.4.4. Interplay of inelastic cotunneling and sequential tunneling

Excited states allow a combination of processes that produces higher currents inside Coulomb diamonds. An excited state is possible can in principle be reached by inelastic cotunneling (IEC). Relaxation is a concurrent process, that undoes the effect of exciting IEC. Here, we suppose that relaxation is not strong. Thus, after the IEC event, an excited level, e.g. $N^* \leftrightarrow N+1$, if in the bias window, allows sequential tunneling (SET) without being immediately stopped by relaxation, $N^* \rightsquigarrow N$:

$$\underbrace{N \to N^*}_{\text{IEC}} \underbrace{\to N+1 \to N^* \to N+1 \to N^* \to N+1 \to}_{\text{SET}} \underbrace{N^* \rightsquigarrow N}_{\text{relaxation}}. \tag{2.24}$$

This phenomenon is called *cotunneling-assisted sequential tunneling*, abbreviated COSET [55]. Fig. 2.9 shows that COSET appears inside diamonds, beyond a minimum absolute bias voltage, in lateral bands delineated by the excited lines.

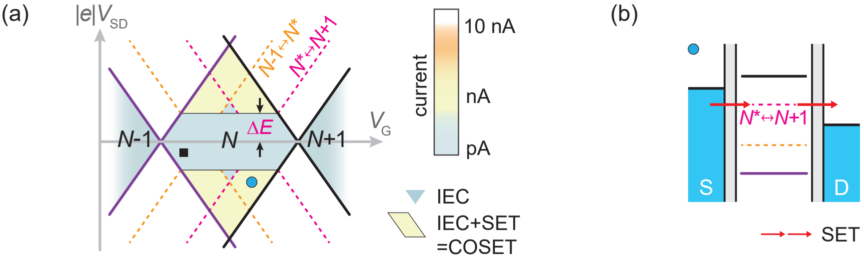

Figure 2.9. **(a)** This charge stability diagram highlights phenomena involving an excited state, $|N^*\rangle$. The current scale shows only possible magnitude orders. The excited lines are dashed. Elastic cotunneling (EC) occurs everywhere; EC in the point marked by ■ is detailed in fig. 2.8a,b. Inelastic cotunneling (IEC) occurs only at sufficient bias voltages, $|eV_{\mathrm{SD}}| \geq \Delta E$; IEC in the point marked by ● is detailed in fig. 2.8c,d. Relaxation is assumed negligible. In the yellow bands of Coulomb diamond N, an excited level is in the bias window (see ●). IEC without relaxation enables sequential tunneling (SET) through this excited level. This phenomenon is termed COSET. **(b)** SET for ● in (a).

Recognizing COSET in Coulomb diamonds is often reduced to observing full or incomplete triangles of enhanced noise and increased current—see the yellow bands sketched in fig. 2.9a. When the COSET bands are wide enough ($\Delta E \geq U_{\mathrm{c}}/3$), the triangle is full, otherwise it is incomplete. We meet both situations in our measurements. We refer to such a graphical feature with the terms *COSET triangle* or *IEC triangle*.

3 Noise in Quantum Dots

Noise — the phenomenon of random fluctuations added to a signal — may be extra information in the carried experiment. For instance, if present, thermal noise can be used in measuring the temperature of a system. In this section, we show that current noise reveals correlations between the electron pulses that constitute the current. We establish a quantitative reference in the Schottky noise and so define the Fano factor. In this thesis, further comparisons of noise levels, each of them characterized by a Fano factor value, will shed light on the discrete flow of electrons through quantum dots. Two instruments—the telegraph noise analysis and full counting statistics—close the chapter.

3.1. Noise as a correlator

In the case of a stationary system, noise means fluctuations around the time-average value of a measured observable. For example, a direct current in an electric circuit (see fig. 3.1) exhibits the current fluctuations:

$$\delta I(t) = I(t) - \langle I \rangle,$$

with $\langle I \rangle$ the time-average current. This particular way to describe noise can be

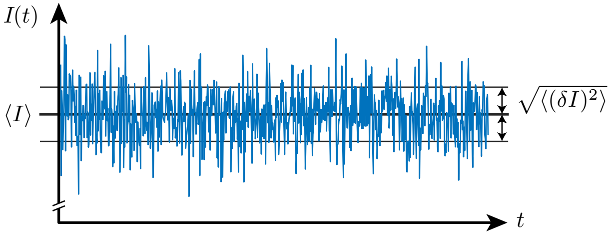

Figure 3.1. Fluctuations in a stationary current.

further concentrated in one number: the standard deviation of the fluctuations, $\sqrt{\langle (\delta I)^2 \rangle_t}$.

Noise can however be quantitatively characterized in more detailed ways and we present here the most common of them. One is the autocorrelator $C_I(t,t') = 2\langle \delta I(t) \cdot \delta I(t')\rangle_t$, with the factor 2 justified later. In a stationary system, this quantity does not depend on the two sweeping moments t and t', but only on the interval $\Delta t = t' - t$:

$$C_I(\Delta t) = 2\langle \delta I(t) \cdot \delta I(t+\Delta t)\rangle_t. \tag{3.1}$$

It is common in stationary stochastic processes and in signal processing to address the autocorrelation of a signal as *power* and its Fourier transform as *power spectrum*. In this case, the autocorrelation of fluctuations will be called *noise power*. Its unit is A^2.

The frequency space counterpart of noise power is the its Fourier transform,

$$S_I(\omega) = \int_{-\infty}^{\infty} C_I(\Delta t) e^{-i\omega\Delta t} d(\Delta t) \text{ for } \omega \geq 0. \tag{3.2}$$

This is called the *noise power spectral density* or simply the *noise power spectrum* [56]. Its unit is A^2/Hz. The noise powers spectral density $S_I(\omega)$ of any frequency value ω incorporates both emission ($+\omega$) and absorption ($-\omega$); this is captured in the factor 2 of the autocorrelator (eq. 3.1).

The above definitions are given for current noise. In the same manner can we treat the noise of other observables, for instance voltage. Thus, $S_V(\omega)$ would be the *spectral density* of *voltage noise power*, measured in V^2/Hz.

Equivalent definitions can be formulated in quantum mechanics, using corresponding operators.

3.1.1. Noise measurements

We run current noise measurements at frequencies of $\sim$3 GHz, far from its disturbing limits: Using cryogenic temperatures, the thermal noise component is also negligible, except for the zero bias voltage. The frequency domain is not high enough for noticeable vacuum fluctuations. These limits are introduced later in the chapter. Another limit is the generally termed $1/f$ noise (the flicker noise), which appears at low frequencies.

The noise data is acquired with a spectrum analyzer—a measurement instrument which collects signal *power* in a frequency range, by applying a bandwidth filter around a set frequency, f_0. This collected power divided by the filter bandwidth is an approximation of the power spectral density in f_0 or its precise value if the noise power spectrum is uniform, i.e. *white noise*.

In order to employ the spectrum analyzer for noise measurement, one needs to separate noise from the underlying, dc signal. This separation is done by a bias tee.

3.1.2. Noise limits: the fluctuation-dissipation theorem

The fluctuation-dissipation relation [57, 58] is a very general theorem in statistical physics that describes noise power spectrum in stationary linear systems:

$$S_I(\omega) = 2\hbar\omega G \left(\coth \frac{\hbar\omega}{2k_\mathrm{B}T} + 1\right), \tag{3.3}$$

where G is the conductance of the noise source. The above relation has two significant limits:

In the low-frequency limit, fluctuations are due to temperature:

$$\hbar|\omega| \ll k_\mathrm{B}T \;\Rightarrow\; \boxed{S_I(\omega) = 4Gk_\mathrm{B}T.} \tag{3.4}$$

This is called *thermal noise.*

For high frequencies or low temperatures, *vacuum fluctuations* play the major role:

$$\hbar\omega \gg k_\mathrm{B}T \;\Rightarrow\; S_I(\omega) = 4G\hbar\omega. \tag{3.5}$$

This is also called *quantum noise.* Because vacuum fluctuations can only absorb energy and cannot be used as a power source, the actual value of the quantum noise should be half:

$$\hbar\omega \gg k_\mathrm{B}T \;\Rightarrow\; \boxed{S_I(\omega) = 2G\hbar\omega.} \tag{3.6}$$

In our experiments, run at frequencies of $\sim 3\,\mathrm{GHz}$, the quantum noise can be neglected.

3.2. Shot noise. Schottky noise. Fano factor

If current is seen as a sequence of electrons flowing through an imaginary ammeter, then fluctuations are obvious: the instantaneous value of the current is either below the average, namely null, when no electron passes through, or above the average, when one electron is passing. The discreteness of charges is therefore the cause of a specific type of noise, termed *shot noise.*

Formally, current can be expressed as a sum of Dirac δ pulses: $I(t) = e\sum_i \delta(t-t_i)$. The average current is $\langle I\rangle = e/\tau$, with τ the average time between two electron pulses. Supposing that the pulse moments, t_i, are *uncorrelated*, the correlator of $I(t)$ from eq. 3.1 easily yields the shot noise power

$$C_I(\Delta t) = |2e\langle I\rangle|\delta(\Delta t) \tag{3.7}$$

and its Fourier transform, the shot noise power spectrum:

$$S_I(\omega) = |2e\langle I\rangle| = S_\mathrm{Schottky}. \tag{3.8}$$

This treatment ignores the possibility of some electrons going in the opposite direction of the average flow. In this complete image, one gets the same result as above.

The noise of uncorrelated pulses was measured first by Schottky in vacuum tubes (1918) [59]. The duration between consecutive uncorrelated pulses follows an exponential distribution, therefore the number of pulses in the time unit is Poissonian-distributed. Different values of the shot noise power spectral density suggest correlations between electron pulses. Using the Schottky noise as a reference, at zero frequency we define the *Fano factor*:

$$\boxed{F = \frac{S_I}{S_{\text{Schottky}}} = \frac{S_I}{|2e\langle I\rangle|}.} \tag{3.9}$$

We say that noise is Poissonian if $F = 1$, sub-Poissonian if $F < 1$, and super-Poissonian if $F > 1$.

3.2.1. Two general expressions for the Fano factor

Using a two-terminal scattering approach—i.e. modeling the system as a medium with several conductance channels n of transmission probability T_n and $G_0 = 2e^2/h$ the conductance of a channel with transmission probability 1—physicists arrived at the following relation [60] for noise power spectral density at zero frequency:

$$S_I = 2G_0 \left[2k_{\text{B}}T \sum_n T_n + eV \coth\left(\frac{eV}{2k_{\text{B}}T}\right) \sum_n T_n(1 - T_n) \right]. \tag{3.10}$$

At small voltage, $|eV| \ll 2k_{\text{B}}T$, the thermal noise dominates: $S_I = 4Gk_{\text{B}}T$, because $G = G_0 \sum_n T_n$.

At small temperatures, $2k_{\text{B}}T \ll |eV|$, one gets $S_I = |2eV|G \sum_n T_n(1 - T_n)/\sum_n T_n = |2e\langle I\rangle|F$, with:

$$\boxed{F = \frac{\sum_n T_n(1 - T_n)}{\sum_n T_n}.} \tag{3.11}$$

In this derivation, we used the equality $VG = \langle I\rangle$, placing ourselves in the linear regime. The formula given by eq. 3.11 is therefore valid for small voltages, such that the current variations responds linearly to voltage changes. Another assumption is that the transmission probabilities are constant.

In a quantum dot, the two tunnel barriers (indices S and D) exhibit various transmission probabilities, $T_{\text{S|D}} \ll 1$. They are Lorentzians centered at the electrochemical potentials (*levels*) of the QD transitions. We write the tunneling rates as $\Gamma_{\text{S|D}} = \hbar\nu T_{\text{S|D}}$ with $\nu = \frac{v_e}{2L}$ the rate at which one electron inside the QD hits one barrier, $v_e = \frac{1}{\hbar}\frac{\partial E}{\partial k}$ the group velocity of the electron and L the width of the QD. If the bias window contains several QD levels (indices n), one obtains [61] the average current

$$\langle I \rangle = \frac{e}{\hbar} \sum_n \frac{\Gamma_{\mathrm{S}n}\Gamma_{\mathrm{D}n}}{\Gamma_{\mathrm{S}n} + \Gamma_{\mathrm{D}n}} \tag{3.12}$$

and the zero frequency shot noise at low temperatures

$$S_I = \frac{2e^2}{\hbar} \sum_n \frac{\Gamma_{\mathrm{S}n}\Gamma_{\mathrm{D}n}(\Gamma_{\mathrm{S}n}^2 + \Gamma_{\mathrm{D}n}^2)}{(\Gamma_{\mathrm{S}n} + \Gamma_{\mathrm{D}n})^3}. \tag{3.13}$$

The Fano factor, $F = S_I/|2e\langle I \rangle|$, results immediately. In the particular case of only one level in the bias window of the QD, the Fano factor takes the form:

$$\boxed{F = \frac{\Gamma_{\mathrm{S}}^2 + \Gamma_{\mathrm{D}}^2}{(\Gamma_{\mathrm{S}} + \Gamma_{\mathrm{D}})^2}.} \tag{3.14}$$

3.2.2. Some typical Fano factor values

The following cases are derived with eq. 3.11:

- $F = 0$ for ballistic wires, because all channels have maximal transmission probability, $T_n = 1$.
- $F = 1$ for a tunnel barrier with very low transmission probability, $T \ll 1$. This result equally applies to a quantum dot in the Coulomb blockade that features only elastic cotunneling.
- $F = \frac{1}{3}$ for diffusive wires [60, 61].

In quantum dots, eq. 3.14 exposes the limits:

- $F = \frac{1}{2}$ in the symmetric QD, i.e. $\Gamma_{\mathrm{S}n} = \Gamma_{\mathrm{D}n}$.
- $F = 1$ in the totally asymmetric QD, i.e. $\Gamma_{\mathrm{S}} \ll \Gamma_{\mathrm{D}}$ or $\Gamma_{\mathrm{S}} \gg \Gamma_{\mathrm{D}}$.

3.3. Telegraph noise and telegraphic transport

The noise exhibited by a signal with only two possible values is called *telegraph noise*. If the signal has two equally probable values, i.e. $\langle I \rangle \pm \delta I$ (fig. 3.2a), then the telegraph noise power, C_I, is finite in one point only [60], namely $\Delta t = 0$. Using the Dirac $\delta(t)$ distribution and τ is a small time constant defined by $\tau\delta(0) = 1$, we write $C_I(\Delta t) = 2(\delta I)^2\delta(\Delta t)\tau$. Its Fourier transform, the telegraph noise power spectrum, reads: $S_I(\omega) = 2(\delta I)^2\tau$. This is *white* noise.

In general, the two values are not equally probable: $I \in \{I_1, I_2\}$ with $p_2/p_1 = m$ the ratio of the probabilities of the two possible values (fig. 3.2b). With

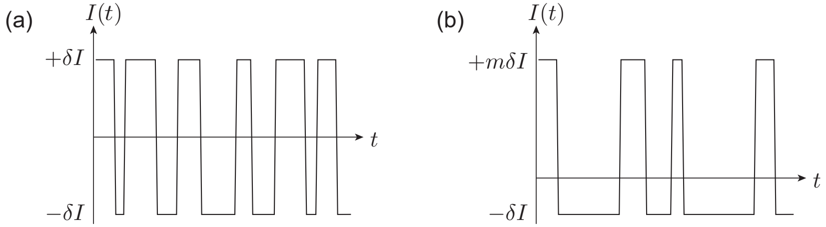

Figure 3.2. **(a)** Simplest form of telegraph noise. Adapted from [60]. **(b)** Generalized telegraph signal.

$\delta I \equiv (I_1 - I_2)/(m+1)$, one can calculate the expressions of the telegraph noise power and noise power spectrum:

$$C_I(\Delta t) = 2m(\delta I)^2 \delta(\Delta t)\tau, \tag{3.15a}$$

$$S_I(\omega) = 2m(\delta I)^2 \tau. \tag{3.15b}$$

If a current is switched on and off, $I_{\mathrm{on}} \neq 0 = I_2$, then a simplifying relation arises: $\langle I \rangle = p_1 I_1 = I_1/(m+1) = \delta I$. The telegraph noise power spectrum becomes: $S_I(\omega) = 2m\langle I \rangle \frac{I_1 \tau}{m+1}$. With the notations $I_{\mathrm{on}} \equiv I_1$ and $P_{\mathrm{off}} \equiv p_2 = \frac{m}{m+1}$, the noise takes the value $S_I(\omega) = 2\langle I \rangle I_{\mathrm{on}} \tau P_{\mathrm{off}}$. Therefore, the Fano factor, $S_I/|2e\langle I \rangle|$, is:

$$F = \frac{I_{\mathrm{on}}\tau}{e} P_{\mathrm{off}}. \tag{3.16}$$

We conclude that longer the circuit is usually off, higher the Fano factor. Also, more intense the charge flow is, bigger the Fano factor.

The above elaboration ignores the discreteness of the electron flow. By considering it, we talk below about the shot noise in telegraphic transport.

It happens in quantum dots that sequential tunneling, thus current, is temporarily interrupted because the quantum system fell in a *blocking* state. Let us take the example of fig. 3.3a: a QD with two transition levels, $N-1 \leftrightarrow N$ and $N-1 \leftrightarrow N^*$, in the bias window ($|N^*\rangle$ denotes an excited state of charge N). We neglect relaxation ($N^* \to N$). The transport sequence is:

$$N-1 \ \rightarrow \ N|N^* \rightarrow \ N-1 \ \rightarrow \ N|N^* \rightarrow \ldots$$

with $N|N^*$ designating (N or N^*). If the tunneling rates ($\Gamma_{\mathrm{S|D}}$ and $\Gamma^*_{\mathrm{S|D}}$) of the two respective transitions are not all equal, but $\Gamma^*_{\mathrm{S}} \gg \Gamma^*_{\mathrm{D}}$, then the transport sequence, once it reaches N^*, stops for a relatively long time, because tunneling-out to the drain is now slow-rated. We say that transport is blocked in state $|N^*\rangle$. The time dependence of the current, sketched in fig. 3.3b, shows that

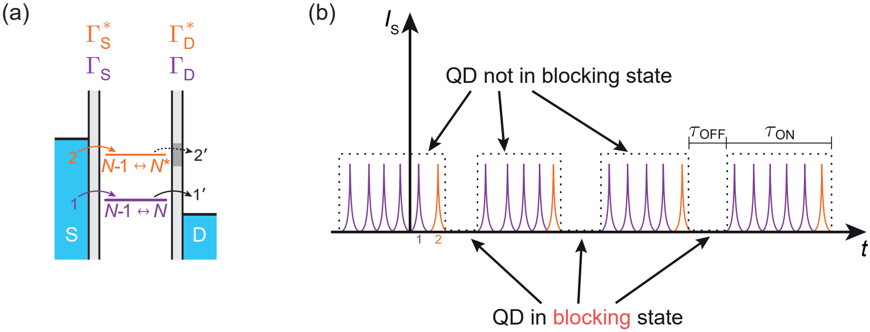

Figure 3.3. (a) Electrochemical-potential diagram of a QD that may fall into a blocking state, because $\Gamma_D^* \ll \Gamma_S^*$. The blocking state is $|N^*\rangle$. **(b)** Telegraphic transport illustrated by the current $I_S(t)$, measured at source. The colors of the electron pulses correspond to the transitions $N-1 \to N|N^*$ in (a). Adapted from [32].

electrons are transported in *bunches*. The situation is described within an equivalent framework in ref. [32], which also derives the following relation for the Fano factor:

$$\boxed{F = 1 + 2\langle n\rangle P_{\mathrm{off}}^2,} \tag{3.17}$$

where $\langle n\rangle \equiv \Gamma_S/\Gamma_S^*$ is the average number of electrons flowing through level $N-1 \to N$. One could argue that the average number of electrons in a bunch is $N_{\mathrm{on}} \approx \langle n\rangle + 1$.

In conclusion, the shot noise in telegraphic transport is characterized by a Fano factor that scales with the square of the blocking-state probability and with the average number of electrons in a bunch.

4 Design, Fabrication, Experimental Setup

4.1. Lumped-resonator design

We wanted to investigate in a microwave experimental setup highly ohmic quantum devices, using lumped-element resonators as impedance transformers. Matching the typical impedance of carbon nanotube quantum dots ($\sim 100\,\mathrm{k\Omega}$) to the $50\,\Omega$ of the transmission lines demands, at $\sim 3\,\mathrm{GHz}$, an LC matching circuit with $L \simeq 120\,\mathrm{nH}$ and $C \simeq 25\,\mathrm{fF}$ (see the example given in 1.2.1), that is a characteristic impedance $Z_\mathrm{c} = \sqrt{L/C} \simeq 2.2\,\mathrm{k\Omega}$. Moreover, the resonator needs to be placed on the same chip as the quantum device, in order to avoid microwave phenomena related to an eventually wavelength-comparable distance between the LC circuit and the quantum dot. This additional requirement brings us to the fabrication of a planar spiral inductor, with the inner end connected through a bridge to the setup.

Our technical endeavor is obtaining $L \gtrsim 100\,\mathrm{nH}$ values for an on-chip coil with a bridge and and $C \lesssim 30\,\mathrm{fF}$ values for the adjacent capacitor. The electrical losses in the coil are minimized by choosing a superconductor metal, i.e. Nb.

It is possible to evaluate on paper the inductance of a polygonal planar coil, using methods (e.g. Grover [62]) or formulas (e.g. Wheeler [63], Mohan [64]) that usually result from combining the mutual inductances of all segments. Several online calculators also implement these methods and formulas. However, a real inductor includes distributed capacitive shunt elements, who can play a heavy role at our target frequencies. Therefore, it is more efficient to design with the aid of first-principles software calculations.

4.1.1. Computer-aided design with Sonnet

We use the Sonnet software suite to architect microwave resonators. Our designs considered first a supported bridge, then an airbridge (fig. 4.1). We eventually opted for the latter, in order to replace several error-prone lithography and sputtering steps by a simpler operation, wire bonding.

Within Sonnet, the metallic material for the resonator, bridge, and ground is modeled as a perfect conductor, since superconductors are not supported by this software suite yet.

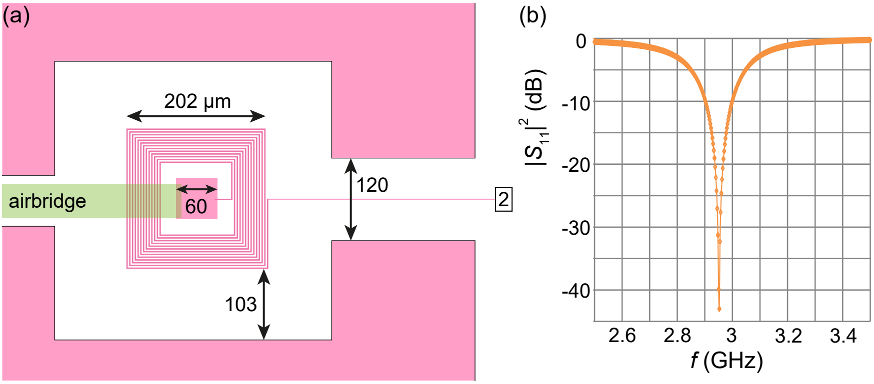

Figure 4.1. **(a)** Coil design with the Sonnet$^{\mathrm{TM}}$ *em* simulation software (zoom). The surrounding pink polygons are parts of the ground plane; white stands for SiO_2. **(b)** The deepest reflectance curve for the resonant circuit in (a) is obtained for a port $\boxed{2}$ resistance of 16.2 kΩ, thus $R_{\mathrm{match}} = 16.2\,\mathrm{k}\Omega$.

Initial geometries tried to separate inductor from capacitor. To do that, the spacing between the spiral inductor and the ground plane was increased up to values beyond which calculations did not change anymore. The existence of this limit is justified by the logarithmic-like distance dependence of the capacitance between two coplanar plates. Even at these spacing values, a shunt distributed capacitance between the coil and ground still subsists; we refer to such an inductor by the label *minimally shunted coil*. The calculated self-resonance of the coil can easily lay in the GHz range.

Thus, we designed minimally shunted spiral coils that resonated at ∼3 GHz, videlicet in the absence of a separate capacitor. Having obtained the desired approximate resonance frequency (given by the LC product), we still had to improve the characteristic impedance (given by the L/C ratio. But increasing the effective inductance, L, by adding turns to the spiral, could not be achieved with a simultaneous decrease of the effective shunt capacitance to ground, C. Indeed, simulations did not show an improvement when simultaneously adding a spiral winding and reducing the coil wire width.

The Sonnet design taken further to fabrication is presented in fig. 4.1a. The coil wire is 2-μm wide. The perfect conductor film has zero height, a good enough approximation of the later sputtered ∼100-nm Nb films. A background plane lies below the 500-μm-thick undoped Si substrate. The airbridge, placed at 150 μm above the plane, is connected to the microwave signal port. At the other end of the coil, the variable-resistance port 2 substitutes the quantum device. By sweeping the resistance of this port, one can find the matched value: the resistance for which the reflectance curve is deepest, fig. 4.1b. Therefore, this design predicts $R_{\mathrm{match}} = 16.2\,\mathrm{k\Omega}$ ($G_{\mathrm{match}} = 62\,\mu\mathrm{S}$), in other words $Z_{\mathrm{c}} = 0.9\,\mathrm{k\Omega}$.

4.1.2. How could one still improve Z_{c}?

We could wonder if, with greater-diameter inductors, one can obtain resonators of higher characteristic impedance, but of same resonance frequency. We neglect the capacitive influence of the ground below the 500-μm dielectric substrate, since it is almost one order of magnitude farther. Upsizing the resonator plane by a factor ζ multiplies inductances with ζ^2 (like encompassed areas) and capacitances with ζ (like an area divided by a distance). Thus at first sight, Z_{c} increases by a factor $\zeta^{1/2}$, but ω_0 decreases, by $\zeta^{3/2}$. To keep the resonance frequency unchanged, one could in addition readjust (by ζ^3) the area of the coil turns, by going back to a narrower coil wire; this leaves coil encompassed areas, and L, unchanged. Consequently, a schematic recipe for improving Z_{c} has loomed. It doubles Z_{c} by a fourfold upsizing of the design, then it corrects the resonance frequency and doubles Z_{c} again by shrinking the coil wire width eight times. This design limit has major disadvantages: it corresponds to a geometry where the background plane should matter, it is considerably harder to calculate in Sonnet and more difficult to fabricate.

Moreover, at second sight, a new ingredient kicks in. The geometry of a spiral coil also includes the inter-turn capacitance, which builds up the effective feed-forward capacitance, C_{f}, introduced in 1.2.2. This ingredient takes part, under the form $\chi = C_{\mathrm{f}}/C$, in the effective inductance value, as shown in equations 1.20, 1.23. Because the recipe constructed above modifies χ, it will also change the the effective inductance and thus the resonance frequency. The recipe can be corrected with an extra step: readjusting the inter-turn gap so that it is not affected by the coil wire shrinking.

Another recipe arises from solely the framework of the feed-forward capacitance. It is obvious that reducing C automatically enlarges χ, thus the effective inductance. Hence, Z_{c} increases, but ω_0 is rather stable. The algorithm that keeps ω_0 unchanged is composed of the following steps: (i) retrieve the value of χ by fitting the Sonnet-provided reflectance curve, (ii) diminish by a fraction x the coil width in order to decrease C, (iii) calculate, from the known quantities χ and x, the new inter-turn gap with which the product LC stays constant, (iv) validate with a Sonnet simulation.

Unfortunately, evidence of the LCC_{f}-model applicability first appeared during the analysis phase that followed the execution of the main experiment. We did not have the occasion to experimentally validate planar spiral resonators redesigned with the above algorithms.

4.2. Fabrication

We fabricated coils with two types of bridges: sputtered on a support or bonded. We favored in the end the bonded-bridge type, essentially because it involves less fabrication steps and a higher yield. For characterization purposes, we also made secondary devices, called *hangers*, where a resonators were coupled or connected to a transmission line (see appendix A).

4.2.1. Bonded-bridge coils

The fabrication of an on-chip superconductor resonator like in the computer-aided design (fig. 4.1) starts with preparing a region on the undoped Si/SiO_2 ($500\,\mu m/170\,nm$) substrate where carbon nanotubes will be placed. The Si crystal parameters are: orientation $\langle 100\rangle$, $\rho > 100\,\Omega m$. Thus, we first evaporate Ti/Au ($10\,nm/30\,nm$) for markers and partial contacts in a square area (fig. 4.2a). We then protect it with a PMMA/HSQ bilayer resist. Afterwards, we sputter 100 nm of Nb and lift the protection bilayer resist off (fig. 4.2b). Subsequently, we e-beam-pattern bonding pads and the desired inductor in a new PMMA resist layer, then etch the Nb film with an Ar/Cl_2 inductively coupled plasma; the surrounding Nb becomes the ground plane.

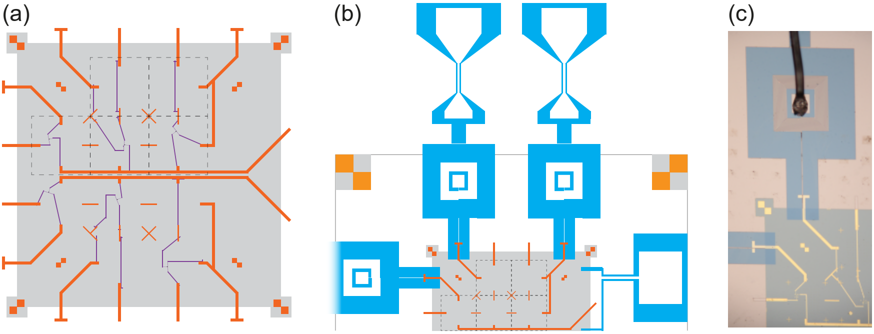

Figure 4.2. **(a)** $1\,mm^2$ region of SiO_2 where CNTs will reside. Markers and partial contacts (orange) are evaporated in the first step. Fine contacts (purple) to selected CNTs are evaporated in a later step. **(b)** With the square window in (a) protected by an HSQ film, we sputter a Nb film (white), then etch in this film spiral coils and contact pads. After that, we lift the HSQ off, stamp CNTs in the square window, and eventually evaporate the fine contacts. **(c)** The last fabrication step is bonding metallic wire from contact pads into the inner pad of the resonators. We use Al wire, visible in this optical photography.

Next, we stamp CNTs [7, 13, 65] in the predefined region, like in fig. 4.3. We locate the stamped CNTs using a scanning electron microscope (SEM) and contact the chosen CNT in one Ti/Au evaporation step to the coil and to ground (fine contacts in fig. 4.2a). In the same lithography step, a side gate is created at a distance of ∼300 nm from the CNT.

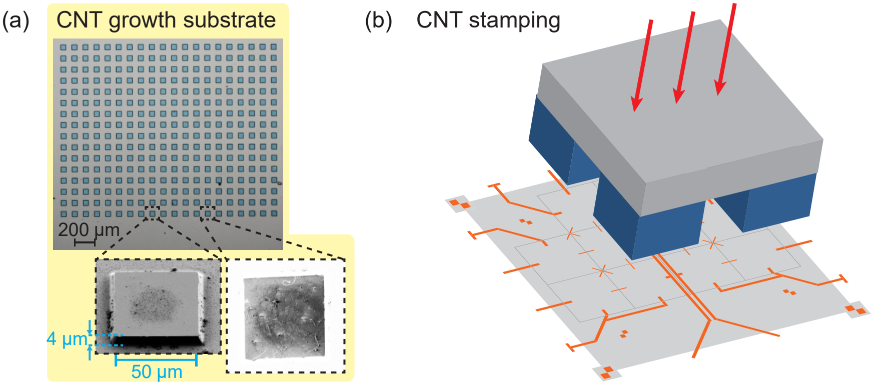

Figure 4.3. **(a)** CNTs are grown on a patterned substrate. Taken from [13]. **(b)** The stamping procedure takes place in a mask aligner, where the CNT stamp resulted in (a) and glued under a glass plate is pressed against the sample.

Finally, with the device glued onto a sample holder, we use Al wire to bond the remaining end of the coil to a neighboring bigger pad (fig. 4.2c). Due to the relatively small size of the inner pad ($70 \times 70\,\mu\text{m}^2$, barely larger than the bonder wedge), the man-operated bonding is delicate In the very end, we connect the latter pad to the microwave line of the printed circuit board sample holder. Furthermore, the Nb ground plane of the sample is bonded with multiple wires along the wafer edge to the sample holder ground plane.

The square spiral inductor used in the main experiment has an outer dimension of $210\,\mu$m, 14 turns with width $w = 2\,\mu$m and spacing $s = 2\,\mu$m. In the device investigated here, two of the turns are shorted, lowering the effective inductance and thus shifting up the resonance frequency by several percents.

4.2.2. Coils with bridge support

Previous versions of planar spiral coils had, instead of bonded Al airbridges, Nb bridges sputtered over a 500-nm-thick crosslinked-PMMA support (fig. 4.4b). The additional fabrication steps were intercalated before CNT stamping. Thus, the PMMA-coated sample is intensely exposed to e-beam ($\sim 3000\,\mu\text{C/cm}^2$), such that a strip forms between the coil inner end and an outer pad. This strip stays after the PMMA liftoff and can serve as a bridge support. Then, the Nb bridge is patterned and sputtered. Only afterwards, CNTs can be stamped, localized, and contacted, as already described.

The yield of this recipe suffers from bridge defects. A Nb bridge can be broken where it descends from its support onto the contact pad (fig. 4.4a). Avoiding this risk by making thinner bridge supports leads to important capacitive effects involving bridge and coil turns. Sometimes, the lateral margins of the bridge are several times higher (fig. 4.4b) and, if they detach during liftoff, they usually create inter-turn shorts in the coil.

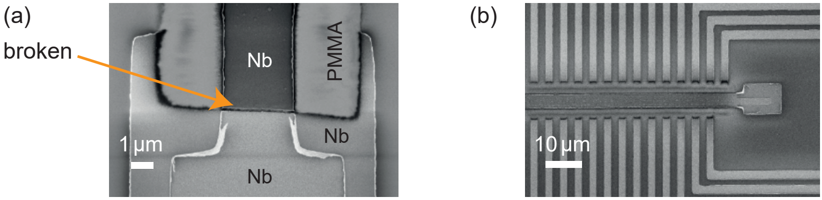

Figure 4.4. **(a)** Contact between Nb bridge and outer pad. The bridge is broken where its support ends. **(b)** SEM micrograph of a supported bridge crossing several coil turns. The end of the bridge presents tall margins.

4.3. Experimental setup

Minimizing the thermal energy of the studied devices is an important condition in the precise measurement of their interesting features. For instance, sharp Coulomb diamonds in quantum dots necessitate negligible thermal broadening. Millikelvin temperatures are produced in dilution refrigerators, that use a mixture of ^{3}He and ^{4}He. At 100 mK, the thermal energy, $k_\mathrm{B}T$, descends under 0.1 meV, much lower than the charging energy of a QD, $\sim$10 meV.

Our measurements are carried in a Triton cryostat produced by Oxford. This is a cryogen-free system or a *dry* dilution refrigerator: ^{3}He is precooled *not* by consumable, cryogenic agents (viz. N_2 at 77 K followed by ^{4}He at 4.2 K, like in wet dilution refrigerators), but by cryocoolers (here, pulse tube coolers, PT). After precooling, the dilution cycle of the lower plates brings temperatures down to 20 mK. The setup is schematized in fig. 4.5c.

The Triton cryostat was wired by our research group during previous microwave projects [13]. The dc loom (fig. 4.5c) is filtered from rf frequencies and reaches the multi-pin nanoconnectors of the sample holder. One cable of the dc loom is additionally low-pass filtered and connected, via a bias tee, to an SMP (rf) connector of the sample holder (marked with a blue arrow in fig. 4.5d). The rf wiring has a descending line, excited by an external *vector network analyzer* (VNA). Attenuated at each plate of the cryostat, the microwave signal is reflected at the sample and deviated by a directional coupler onto the ascending rf line. This line encounters a cryoamplifier, before entering a different port of the VNA.

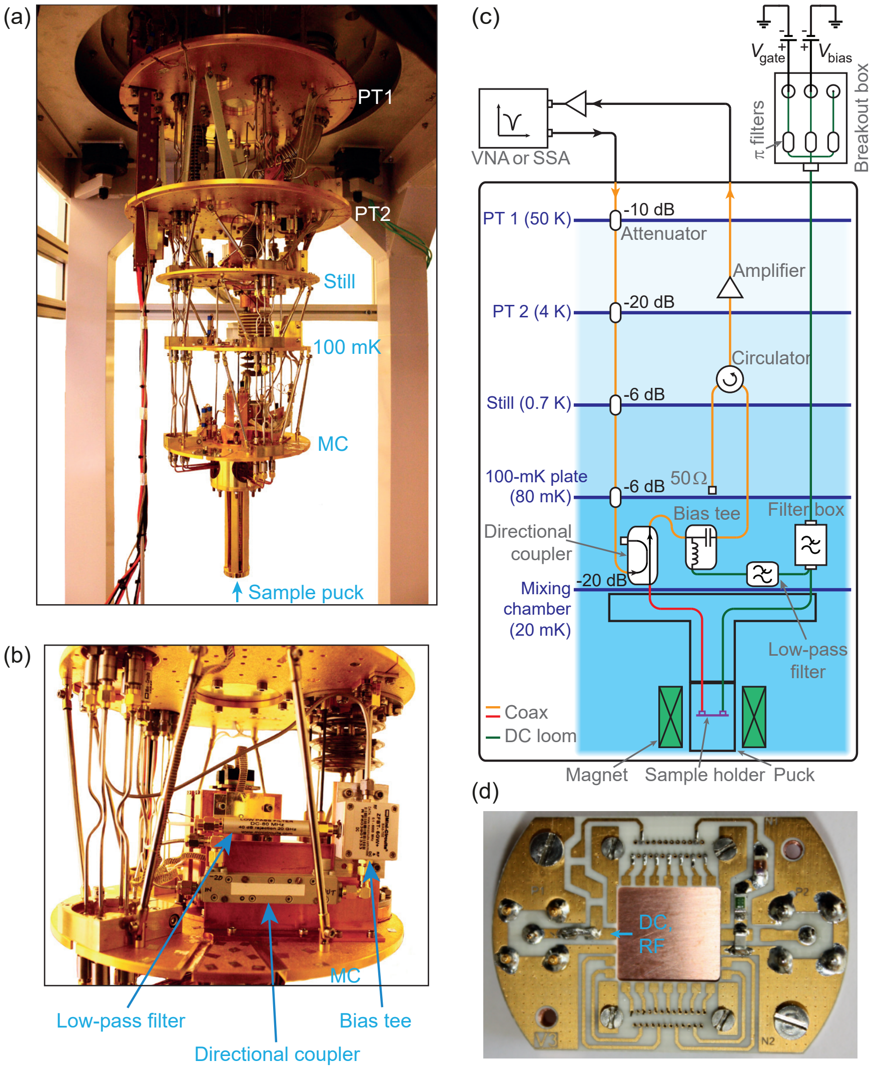

Figure 4.5. Adapted from [13]. **(a)** Picture of the opened Oxford Triton cryostat, without cans or magnet. **(b)** Photograph of the mixing chamber plate. Its diameter is ∼40 cm. **(c)** Sketch of the cryogenic setup, connected to external rf instruments (VNA or SSA) and dc sources. **(d)** Sample holder. The sample is to be glued and bonded on the central copper ground plane surrounded by the printed circuit board. Two SMP connectors and two multi-pin nanoconnectors, placed on the opposite side, attach the sample holder to the puck.

A circulator with a 50-Ω termination recuperates eventual reflections from the cryo-amplifier, in the frequency range 2.5 GHz – 3.5 GHz.

For noise measurements, the rf wiring functions slightly differently: the descending rf line is not connected, the microwave signal is the noise emitted by the sample, and the same ascending rf line as above takes the sample noise to a *signal and spectrum analyzer* (SSA). A second room temperature amplifier is added in front of the SSA port. The total gain of the amplification chain, g, is important later in retrieving the sample noise values from the SSA-measured noise power. This gain was previously measured by our team with the help of a gold wire in the hot-electron regime. Knowing both the Fano factor of this regime, $F = \sqrt{3}/4$, and the conductance of the wire, as well as and the temperature of the mixing chamber (MC), the gain was obtained by simply comparing the SSA-collected noise power to the current noise of the wire. The method is detailed in [7]. Therefore, the amplification chain has a gain $g = 94.6\,\mathrm{dB}$.

4.3.1. RF measurements at 4.2 K

Measurements of characterization samples, e.g. superconducting resonators, are carried in a helium dewar at 4.2 K. For this, we use a dipstick with coaxial cables, presented in fig. 4.6. With one end of the dipstick in the ^{4}He bath and the other end connected to a VNA, we acquire transmission or reflection curves in the 100 kHz – 8 GHz frequency domain.

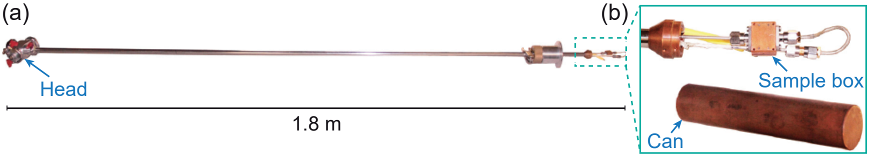

Figure 4.6. **(a)** RF dipstick for 4.2 K measurements in a He dewar. **(b)** Zoom of the open dipstick end. Taken from [13].

5 Measurement

In this chapter, we present measurements of a quantum dot with an impedance-matching LC resonator, fabricated according to the methods explained in chapter 4. First, we reveal raw data for dc current and rf reflectance, then we produce the appropriate calibrated conductance data. Second, we calculate the parameters of the LC resonator. Third, we present raw noise data and subsequently deduce the calibrated, QD shot noise.

The measurements are done at a frequency of about 3 GHz, where the $1/f$ noise is insignificant and the quantum noise is still negligible.

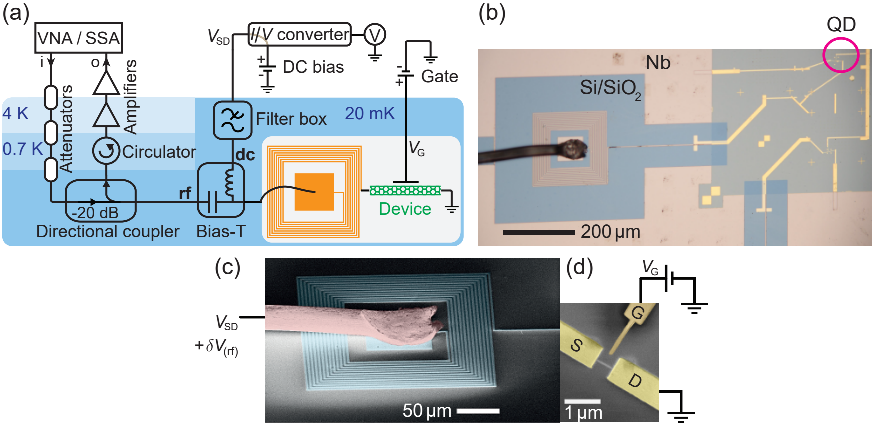

Figure 5.1. **(a)** Measurement setup sketch. The microwave (rf) input and output lines are marked with “i” and “o”, respectively. **(b)** Optical picture of the device under test. The quantum dot is inside the red circle. **(c)** False-color scanning-electron micrograph (SEM) of the bonded coil. **(d)** False-color SEM of the carbon nanotube quantum dot. The source and drain are marked with S and D; the gate is noted with G.

The device under test (DUT), consisting of a QD and a coil (fig. 5.1bcd), is connected electrically to both a dc circuit and an rf circuit (fig. 5.1a). In the DUT, a direct current flows on which a relatively small alternating current is superimposed. The dc-connected DUT is schematized in fig. 5.2a. The rf circuit with the DUT is sketched in fig. 5.2b. The DUT is modeled with lumped elements: L is the inductance of the coil, C its capacitance to ground, and R_{loss} the effective loss resistance, accounting for the rf loss of the superconducting material and the dielectric loss in the substrate.

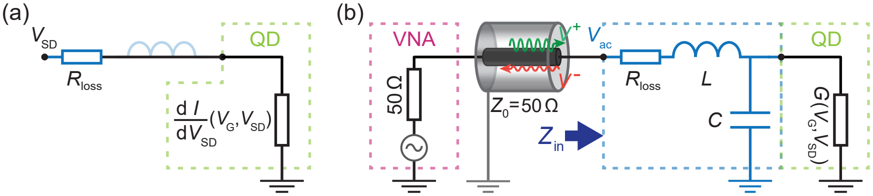

Figure 5.2. **(a)** Schema for the dc circuit. **(b)** Simplified schema for the rf circuit, in reflectometry mode. $V_{\text{ac}} = V^+ + V^-$ is the ac signal sensed by the DUT. The QD admittance is considered to be purely real: $G(V_{\text{G}}, V_{\text{SD}})$.

The current is measured in the dc circuit, in a sweep of the gate and bias voltages, V_{G} and V_{SD}, with V_{SD} being swept for each value of V_{G}. The measured current, $I(V_{\text{G}}, V_{\text{SD}})$, is differentiated numerically along the fast axis and the resulting differential conductance, dI/dV_{SD}, is shown in fig. 5.3a. This is a charge stability diagram, in which Coulomb diamonds are evident.

5.1. Reflectometry

In the rf circuit (fig. 5.1), the microwave signal sent by the vector network analyzer (VNA) ac source[1] travels to the DUT; the signal reflected by the DUT is farther deviated by the directional coupler onto a distinct line, reaching a different port of the VNA. The initial ac signal undergoes:

(i) a total attenuation a, $a(\text{dB}) \approx -87\,\text{dB}$, then

(ii) a reflection at DUT of coefficient Γ and finally

(iii) an amplification of gain g_{r}, $g_{\text{r}}(\text{dB}) \approx 60\,\text{dB}$.[2]

Therefore, the VNA perceives an effective reflection coefficient, $\Gamma_{\text{VNA}} \equiv V_{\text{o}}/V_{\text{i}}$, different from Γ. The measured effective reflectance, $|\Gamma_{\text{VNA}}|^2 = a|\Gamma|^2 g_{\text{r}}$, is mapped in fig. 5.3b. The frequency at which the reflectance map is recorded, $f_{\text{m}} = 3.23\,\text{GHz}$, is chosen with the attempt of reaching the deepest reflectance values for any voltage point $(V_{\text{G}}, V_{\text{SD}})$.

---

[1] We use a VNA signal of $-25\,\text{dBm}$.

[2] The complete amplification chain used in noise measurements has a well-determined gain, $g(\text{dB}) = 94.6\,\text{dB}$. In reflectometry measurements, a room temperature amplifier of $\sim$35 dB is not used.

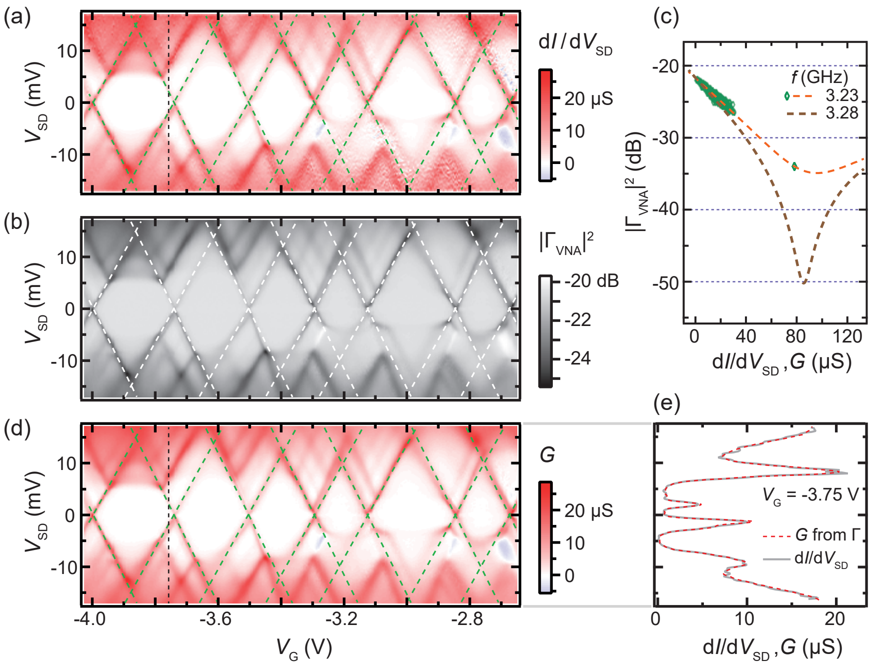

Figure 5.3. **(a)** Derivative of the dc current (dI/dV_{SD}) as a function of the gate and source-drain voltages. The contour of the Coulomb diamonds is highlighted by the dashed line. **(b)** Reflectance measured at $f = 3.23\,\mathrm{GHz}$, with the same contour as in (a). **(c)** Points of the (a),(b) maps are pinned as a scatter plot (green diamonds). An extra point, near impedance matching, is added to the plot. The fit of plot (dashed orange) reveals the LC-circuit parameters. With them, the reflectance-conductance dependence at resonance is built (dashed brown), too, and its minimum corresponds to G_{match}. **(d)** The rf conductance, G, deduced from the reflectance $|\Gamma_{\mathrm{VNA}}|^2\,(V_{\mathrm{G}}, V_{\mathrm{SD}}, f{=}3.23\,\mathrm{GHz})$ by using the fitting curve, $|\Gamma_{\mathrm{VNA}}|(G)$, form (c). **(e)** Cuts in the (a),(d) maps, showing the overlap of low- and high-frequency differential-conductance values.

The reflectance map, $|\Gamma_{\mathrm{VNA}}|^2(V_{\mathrm{G}}, V_{\mathrm{SD}})$, looks also like a charge stability diagram. Compared with the current or differential-conductance map (fig. 5.3a), its acquisition is faster and it is less noisy, i.e. it exhibits clearer features. Γ_{VNA} is the DUT reflection coefficient, $\Gamma = V^-/V^+$ (fig. 5.2b), downshifted in logarithmic scale by a baseline, b:

$$\Gamma_{\mathrm{VNA}} = b\Gamma \quad \text{with} \quad |b|^2 = a g_{\mathrm{r}}. \tag{5.1}$$

When using decibels, this equation rewrites as $|\Gamma_{\mathrm{VNA}}|^2(\mathrm{dB}) = |b|^2(\mathrm{dB}) + |\Gamma|^2(\mathrm{dB})$, with $|b|^2(\mathrm{dB}) = a(\mathrm{dB}) + g_\mathrm{r}(\mathrm{dB})$. Over larger frequency ranges, one often sees a frequency dependence of the baseline, $b = b(f)$, usually due to changes in a and g_r. Because Γ depends on the QD rf admittance, G, through the relations

$$\Gamma = \frac{Z_\mathrm{in} - Z_0}{Z_\mathrm{in} + Z_0} \tag{5.2}$$

and

$$Z_\mathrm{in} = R_\mathrm{loss} + i\omega L + \frac{1}{G + i\omega C}, \tag{5.3}$$

our first task is to retrieve $G(V_\mathrm{G}, V_\mathrm{SD})$ from the reflectance map, $\Gamma_\mathrm{VNA}(V_\mathrm{G}, V_\mathrm{SD})$.

We reasonably assume that the QD admittance is purely real and we consequently call it directly rf conductance. With this assumption, the rf conductance of the QD and its dc conductance coincide[3], $G = dI/dV_\mathrm{SD}$, like in [6, 7]. Thus, we can plot in the plane $|\Gamma_\mathrm{VNA}|^2 \times G$ (fig. 5.3c) the pairs $(|\Gamma_\mathrm{VNA}|^2, dI/dV_\mathrm{SD})(V_\mathrm{G}, V_\mathrm{SD})$ picked from the reflectance and the differential-conductance maps. We fit these points[4] on a theoretical curve, $|\Gamma_\mathrm{VNA}|^2(G)$, given by equations 5.1, 5.2, 5.3. The fit parameters are: L, C, $b(f_\mathrm{m})$. The loss resistance was neglected and we justify this choice in the appendix A. The fit reveals $L = 37\,\mathrm{nH}$, $C = 63\,\mathrm{fF}$. Therefore, the resonance frequency of the lossless resonator is $f_0 = 1/(2\pi\sqrt{LC}) = 3.28\,\mathrm{GHz}$ and its characteristic impedance is $Z_\mathrm{c} = \sqrt{L/C} = 766\,\Omega$. Also in fig. 5.3c we build, with the help of the newly found circuit parameters, the reflectance-conductance dependence at the resonance frequency, f_0. We can see here that $\Gamma_\mathrm{VNA}(G, f_0)$ has two branches: it first decreases to reach almost zero reflectance at the matching point, $G = G_\mathrm{match}$, then increases back for $G > G_\mathrm{match}$.

Once we determined the $\Gamma_\mathrm{VNA}(G)$ curve, we can invert the descending branch of $G(|\Gamma_\mathrm{VNA}|)$, either analytically or by means of a lookup table. This function, applied to the reflectance map (fig. 5.3b), provides the QD rf-conductance map, $G(V_\mathrm{G}, V_\mathrm{SD})$, see fig. 5.3c. This map is visibly equivalent to $dI/dV_\mathrm{SD}(V_\mathrm{G}, V_\mathrm{SD})$, but has an improved resolution. This equivalence is illustrated by cuts in the two maps (fig. 5.3e).

5.2. Noise measurement and calibration

When a dc current flows through the DUT, the current noise is transferred by the bias tee into the rf circuit. At the end of the rf-circuit output line, we place

---

[3] Because here the rf signal, δV, is equivalent to a perturbation of the dc signal, V, one can write $\delta I = \frac{dI}{dV}\delta V$ and conclude with $G = dI/dV$, i.e. the rf conductance is the differential dc conductance. However, at GHz frequencies, the QD admittance has *a priori* an imaginary part, B. If $B \ll G$, then we can use $G = dI/dV_\mathrm{SD}$.

[4] For a better precision, we use an extra point $(|\Gamma_\mathrm{VNA}|^2, dI/dV_\mathrm{SD})(V_\mathrm{G}, V_\mathrm{SD})$, not belonging to the two maps. This point is the lowest reflectance value we measured, in a QD regime $(V_\mathrm{G}, V_\mathrm{SD})$ exhibiting a conductance $G \approx G_\mathrm{match}$ close to the one matched by the LC network.

a signal spectrum analyzer (SSA) instead of the VNA. As opposed to the reflectometry mode, in the noise measurement mode the input ("i" port in fig. 5.1a) is not used. The simplified rf circuit is shown in fig. 5.4a.

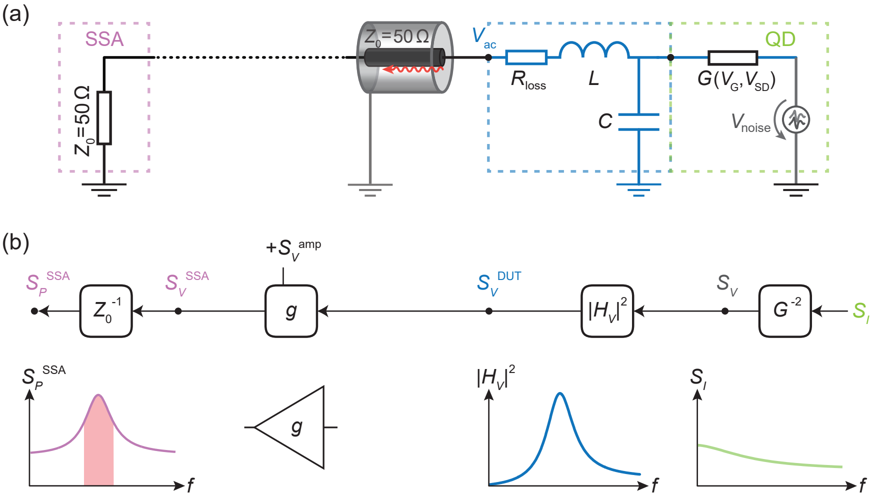

Figure 5.4. **(a)** Simplified schema for the rf circuit, in noise measurement mode. **(b)** Noise transfer chain. Each square box is a multiplier. g is the total gain of the amplifiers.

Let us calculate, from the SSA-measured noise, the spectral density of the noise power produced by the QD. The noise power originated in the QD is transferred over the DUT, transmission lines, and microwave components to the 50-Ω impedance of the SSA port (fig. 5.4b). A voltage transfer function is generally defined for a two-port box, as the ratio between the output and the input voltage. The transfer function of the DUT reads

$$H_V(i\omega) = \frac{V_{\rm ac}}{V_{\rm noise}}$$

and is easily calculated in this LC model to be:

$$H_V(i\omega, G) = \frac{G Z_0}{1 + \frac{Z_0 + R_{\rm loss}}{R} + i\frac{\omega}{\omega_0}\left(\frac{Z_0 + R_{\rm loss}}{Z_c} + \frac{Z_c}{R}\right) + \left(i\frac{\omega}{\omega_0}\right)^2}, \tag{5.4}$$

where $\omega_0 = 1/\sqrt{LC}$ is the angular resonance frequency of the lossless LC network and $R = G^{-1}$. Given that $\omega = 2\pi f$, we often use the notation $H_V(if)$ instead. This function is plotted for several QD conductance values in fig. 5.5a.

Consequently, the voltage noise, $S_V = S_I/G^2$, is transferred to the rf circuit as $H_V(if,G)^2 S_V$ and, after amplification, it arrives at the SSA as $S_V^{\mathrm{SSA}}(f) = gH_V(if,G)^2 S_V + S_V^{\mathrm{amp}}$, where S_V^{amp} is the voltage noise added by the amplifier. This noise transfer chain is sketched in fig. 5.4b. The power noise spectral density sensed by the SSA is $S_P^{\mathrm{SSA}} = \frac{1}{Z_0}|S_V^{\mathrm{SSA}}(f)|$, where $Z_0 = 50\,\Omega$ is the impedance of the SSA port. Because we measure in a frequency bandwidth $\mathrm{BW} = 50\,\mathrm{MHz}$ around $f_{\mathrm{m}} = 3.23\,\mathrm{GHz}$, the value we collect is:

$$\boxed{\delta P} = \int_{\mathrm{BW}} \frac{1}{Z_0}|S_V^{\mathrm{SSA}}|df = \boxed{\frac{S_I}{Z_0} g \int_{\mathrm{BW}} \left|\frac{H_V(if,G)}{G}\right|^2 df + \delta P_0.} \tag{5.5}$$

Here above, the only extra noise source considered, S_V^{amp}, is the amplifier chain. However, the system contains other noise sources too, e.g. thermal noise in the lines or in the microwave components. We capture all these setup spurious contributions in the term δP_0 of eq. 5.5. δP_0 is the noise power measured at zero bias, where the lack of dc current in the DUT, as well as negligible thermal and quantum noise, gives $S_I = 0$. With thermal and quantum noise neglected in the QD, S_I is purely shot noise.

Extracting the noise of the QD from the measured noise power is now straightforward: $S_I = k(G) \times (\delta P - \delta P_0)$, where $k(G)$ is the calibration coefficient:

$$k(G) = \frac{Z_0}{g \int_{\mathrm{BW}} \left|\frac{H_V(if,G)}{G}\right|^2 df}.$$

In fig. 5.6, we present the measured noise power, the calibration coefficient map, and the extracted (*calibrated*) noise, i.e. the current noise of the QD.

In the endeavor of mapping the QD sub- and super-Poissonian noise, we compare the extracted shot noise with the Poissonian reference, $|2e\langle I\rangle|$, also known as

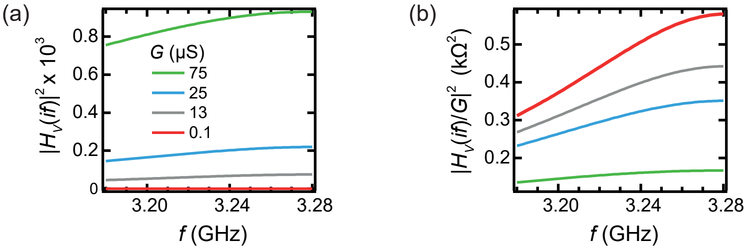

Figure 5.5. (a) Voltage transfer function, $H_V(if)$, for several QD conductance values. **(b)** Current-to-voltage transfer function, $H_V(if)/G$, for the same QD conductance values as in (a). In both (a) and (b), the frequency domain is the range over which the SSA is set to collect noise power.

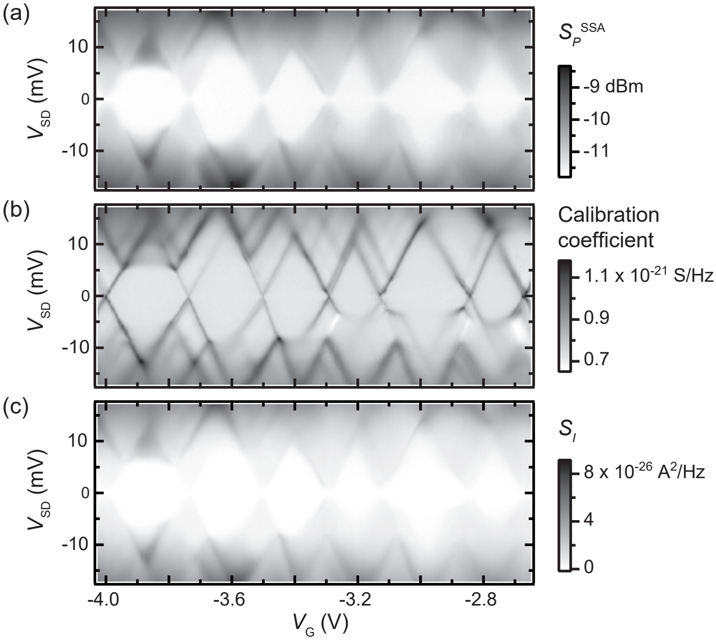

Figure 5.6. **(a)** Noise power measured by the signal spectrum analyzer (SSA) in a bandwidth of 50 MHz around the central frequency, 3.23 GHz. **(b)** Calibration coefficient, $k(V_G, V_{SD})$, for the noise map depicted in (a). **(c)** Shot noise spectral density, S_I, obtained from (a) and (b).

Schottky noise. In order to use a better-resolution current map, we rebuild it from the conductance, $G = dI/dV_{SD}$, retrieved in reflectometry: $I = \int_0^{V_{SD}} G \cdot dV_{SD}$. Fig. 5.7ab presents the Schottky noise spectral density, $|2e\langle I\rangle|$, and the excess noise, $S_I - |2e\langle I\rangle|$, at the measurement frequency, $f_m = 3.23$ GHz. In the latter, one can already distinguish super-Poissonian noise from sub-Poissonian noise.

We finally illustrate the Fano factor the Fano factor, $F = S_I/|2e\langle I\rangle|$, in the map of fig. 5.7c. Its highest values, $F \approx 8$, are present in the cut $V_{SD} = -3.82$ V, plotted in fig. 5.7e.

5.3. Alternative model in reflectance fitting and noise calibration

Heretofore, the matching network we use was characterized as an LC circuit (fig. 5.2a). The extracted parameters of the LC circuit reproduce correctly the $\Gamma(G, f = f_m)$ dependence at the measurement frequency, $f_m = 3.23$ GHz.

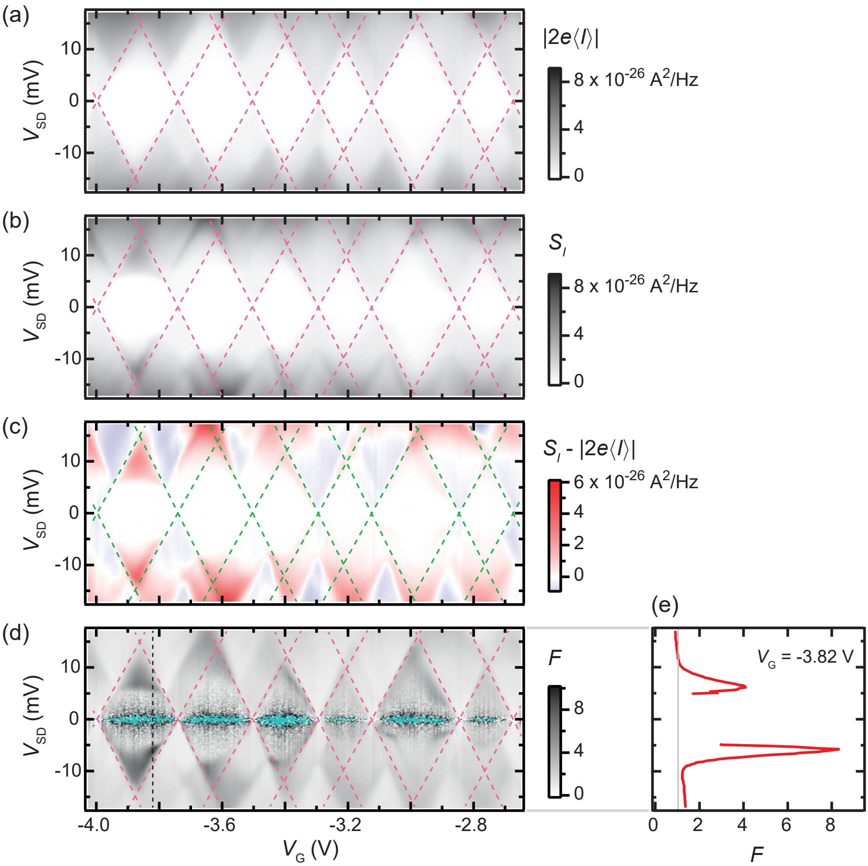

Figure 5.7. **(a)** Schottky noise, $|2e\langle I\rangle|$, calculated from the measured dc current, I. The Coulomb diamond contours (dashed lines) are copied from the conductance plot in fig. 5.3c. **(b)** Shot noise spectral density, S_I, as a function of V_G and V_{SD}, obtained from the SSA-measured noise power, $\langle\delta P\rangle$. **(c)** The excess noise, $S_I - |2e\langle I\rangle|$, shows super-Poissonian noise in red and sub-Poissonian noise in blue. **(d)** Fano factor, $F = S_I/|2e\langle I\rangle|$. Instead of $F = 1$ proper to elastic cotunneling, the low-bias cyan regions indicate erroneously calculated values emerging from the division of a "noisy" number by a very small current value. These regions need to be discarded. A cut at the black dashed vertical is depicted in **(e)**. The observed highest Fano factor is $F \approx 8$.

Nonetheless, they fail to reproduce the frequency dependence of the reflection coefficient, $\Gamma(G, f)$, and fig. 5.9a shows this misfit.

An LC-network model that succeeds in reproducing the frequency dependence $\Gamma(G, f)$ is the LCC_f model, which consists of an LC tank circuit with a feed-forward capacitor (C_f) in parallel with the inductor (L), see section 1.2.2. The electrical schema of the new model is given in fig. 5.8. The impedance of the device is now:

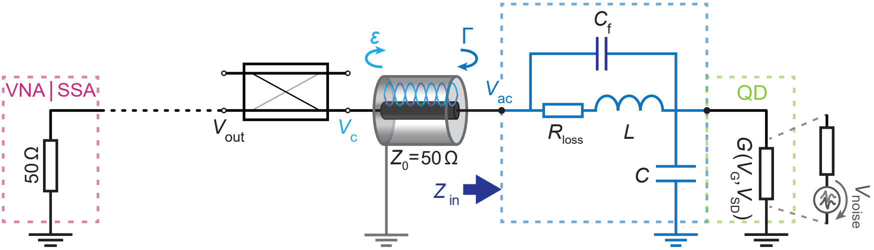

Figure 5.8. Simplified schema for the rf circuit in the LCC_f model, with the faulty directional coupler producing a reflection of coefficient ϵ. The Fabry-Pérot-like cavity is depicted as a coaxial cable with reflections at both ends (ϵ, Γ) and it emerges between the directional coupler and the DUT.

$$Z_\mathrm{in} = \frac{1}{(R_\mathrm{loss} + i\omega L)^{-1} + i\omega C_\mathrm{f}} + \frac{1}{G + i\omega C}. \tag{5.6}$$

This model manages to fit considerably better the bandwidth and depth of the reflectance curve (fig. 5.9b). In order to also reproduce the standing-wave background (fig. 5.9c), that shifts the $|\Gamma|^2$ minima towards smaller frequencies, we add to the model a Fabry-Pérot-like cavity of electrical length d produced by a defect on the rf line (see section 1.3.1). The defect model successful in reproducing our standing-wave pattern is that of an erroneous directional coupler.

The fitting procedure was applied onto a $\Gamma(f, V_\mathrm{SD})$ map (fig. 5.10a) at a fixed gate voltage, so that the conductance, $G = dI/dV_\mathrm{SD}$, is known. The fitting function corresponds to eq. 1.33, multiplied with a constant baseline. In fitting, giving more weight to a small interval around f_m enforces $G(\Gamma_\mathrm{VNA}, f_\mathrm{m}) \approx dI/dV_\mathrm{SD}$ at f_m, which is important in the noise calibration precision.

The extracted fit parameters are: $L = 10.2\,\mathrm{nH}$, $C = 66.4\,\mathrm{fF}$, $\chi \equiv C_\mathrm{f}/C = 2.56$, $R_\mathrm{loss} = 0.16\,\Omega$, $d = 0.84\,\mathrm{m}$, and $74.3\,\Omega$ for the port impedance of the faulty directional coupler, i.e. $\epsilon = 20\%$. It results a resonance frequency $f_0 = 3.24\,\mathrm{GHz}$. The effective inductance, $L_\mathrm{f} = (1 + \chi)L = 36.3\,\mathrm{nH}$, and the capacitance are very close to the values obtained with the LC model.

The new circuit model gives rise to a different structure of the voltage transfer function $H_V(i\omega)$ and to the additional transfer components $H_V^\mathrm{cavity}(i\omega)$ and $H_V^\mathrm{dircoupler}$. We calculate these transfer functions to be:

$$H_V(i\omega) = \frac{G}{G + i\omega C + \frac{1}{Z_0}\frac{1+[G+i\omega(C+C_\mathrm{f})](R_\mathrm{loss}+i\omega L)}{1+i\omega C_\mathrm{f}(R_\mathrm{loss}+i\omega L)}},$$

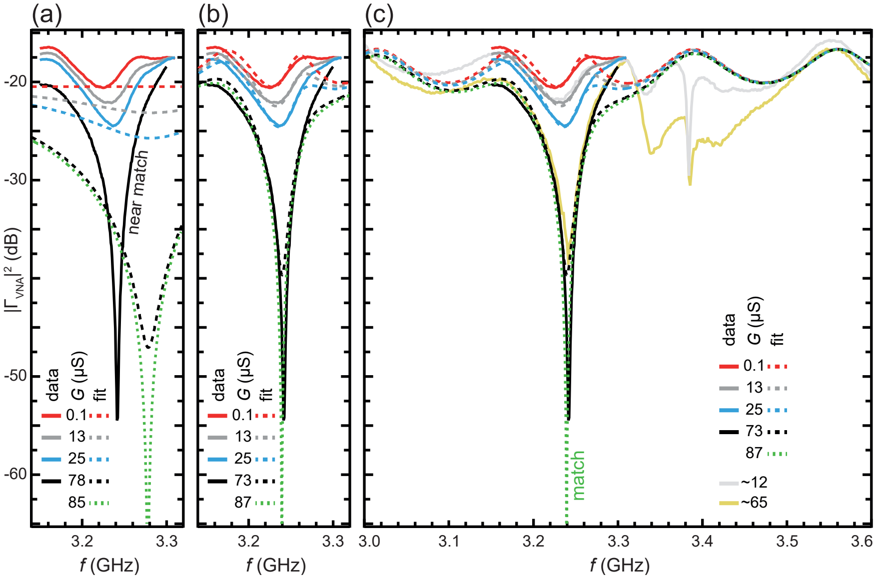

Figure 5.9. Frequency dependence of reflectance, for several conductance values. **(a)** The dashed curves are built with the fit parameters obtained within the *LC* model, by fitting data collected at 3.23 GHz. These “fitting” curves concord with the data curves only around this frequency. **(b)** The fitting curves are obtained within the LCC_f model, from data collected in the [3.150, 3.266] GHz range. **(c)** Extrapolated over a larger frequency range, the fit result from (b) reproduces the observed standing-wave pattern. A spurious effect characterized by deeper reflectance values at 3.38 GHz is not captured by the model.

$$H_V^{\text{cavity}}(i\omega) = \frac{e^{-ikd}}{1-\delta\Gamma(i\omega)e^{-i\cdot 2kd}},$$

$$\left|H_V^{\text{dircoupler}}\right|^2 = 1 - c^2 - \delta^2 \approx 1 - \delta^2$$

and we plot them in fig. 5.11. We observe that the power transfer in the LCC_f model is reduced, compared with the *LC* model, in a fraction of the measurement interval. Hence, noise calibration reveals a higher Fano factor than in the *LC* model (maxima up to +50%, while $F \approx 1$ values do not change), as selectively shown in fig. 5.12.

5.3.1. Which model is better?

Both the *LC* and the LCC_f model presented above are variants of a π model of a planar spiral coil [9]. Connected to our measurement setup, the left capacitor in

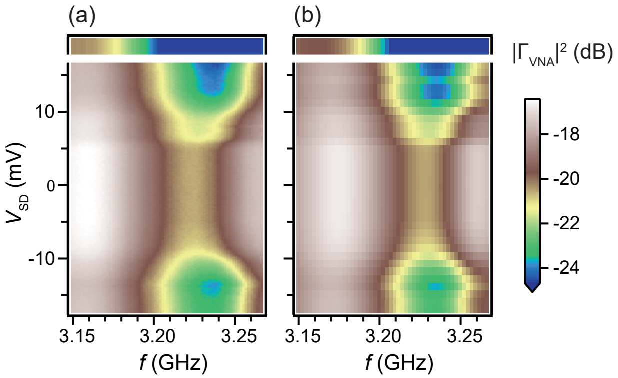

Figure 5.10. **(a)** Frequency dependence of reflectance, $|\Gamma_{\text{VNA}}|^2(f)$, at a fixed gate voltage ($-3.88\,\text{V}$) and a varying bias voltage, V_{SD}. Sweeping V_{SD} gives access to different conductance values. The top rows belong to a distinct acquisition, in which the low reflectance (down to $-54\,\text{dB}$) indicates that $dI/dV_{\text{SD}} \approx 75\,\mu\text{S}$ is close to the matched conductance. **(b)** Fitting map of the data in (a). The fitting curves of fig. 5.9b are V_{SD} cuts in this map.

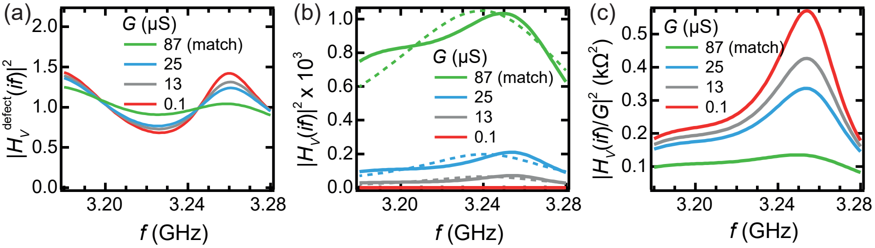

Figure 5.11. **(a)** Voltage transfer function of the "defect", $H_V^{\text{defect}} = H_V^{\text{cavity}} H_V^{\text{dircoupler}}$, for several QD conductance values. **(b)** Voltage transfer function, from the QD to the output port of the directional coupler (solid curves). Dashed curves: voltage transfer function of the DUT only. **(c)** Current-to-voltage transfer function, $H_V(if)/G$, from the QD to the output port of the directional coupler.

fig. 5.13 experiences relatively high losses due to the parallel resistor $Z_0 = 50\,\Omega$ that the setup transmission lines embody. With this capacitor neglected, it is now easy to visualize the two variants: LC for $C_\text{f} = 0$ and LCC_f for $C_\text{f} > 0$.

Technically, the LC model is easier to utilize, because it involves less fit parameters. However, it introduces inexactness in the extracted shot noise, through the voltage transfer function.

Physically, the LCC_f model is more precise. However, it is not accurate enough

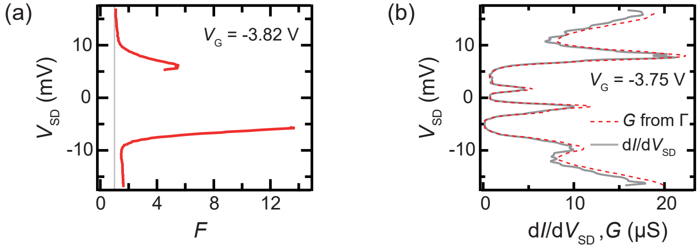

Figure 5.12. (a) Fano factor at fixed gate voltage and varying bias voltage, extracted with the LCC_f model. Higher noise values are retrieved than in the LC model. **(b)** Comparison between the calculated conductance and dI/dV_SD, after fitting with the LCC_f model.

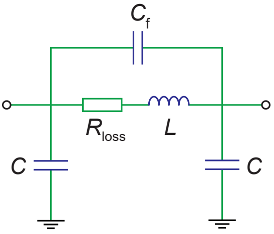

Figure 5.13. The π model of a spiral planar coil contains two lateral shunt capacitors (C and C in the symmetric version) and a feed-forward capacitor (C_f).

in the presence of a frequency-dependent background. Hence, the standing-wave pattern seemingly produced by the faulty directional coupler necessitates a further extension of the model, thus more fit parameters. In consequence, fitting is more unstable—relatively to the initial guess or to local domains of apparent convergence.

Although the combination of the LCC_f model and the proper microwave defect model do produce a preciser fit, the noise calibration initially obtained with the LC model is still qualitatively valid. Although the quantitative results have different scales, Poissonian noise ($F = 1$) is retrieved by both methods in the same places. Therefore, it is not wrong to further analyze the data processed with the LC model.

6 Blocking States in Quantum Dots

The remarkable features of our data, presented in the previous chapter, are combinations of super-Poissonian noise with:

- relatively high conductance, inside several Coulomb diamonds (e.g. the first and fifth diamonds in the charge stability diagrams of the previous chapter, see figures 5.3d and 5.7d) or
- relatively low conductance, in the vicinity of a Coulomb diamond (e.g. the fourth and sixth diamonds in the same charge stability diagrams), often delimited by segments of negative differential conductance.

This chapter presents the analysis of these two categories. Both analyzed cases highlight quantum dot transport mechanisms involving blocking states. Such a state is one in which the QD is trapped; when a QD is in a blocking state, the electric current is switched off.

The analysis is supported by numerical simulations using a master equation approach in the framework of full counting statistics. The closing section discusses the overlap between super-Poissonian noise and negative differential conductance.

6.1. Data investigation supported by numerical simulations

The analysis presented in this section is published in our *Physical Review B* article [66]. In addition, we detail how blocking is lifted.

6.1.1. Data selection

First, we pick out data candidates for analyzing the two evoked categories. The study candidate for the first category is the first Coulomb diamond (CD) in fig. 5.3 and fig. 5.7, as it exhibits the highest Fano factor values. The study candidate for the second category could have been either the fourth or the sixth CD, but we eventually utilized the data of a supplemental measurement carried out in our group[1] (see appendix B), due to a better contrast in noise and negative differential conductance (figures 6.1f,h). Therefore, we further refer to the first candidate as *device A* and to the second candidate as *device B*.

---

[1] This related measurement was effectuated by Roy Haller and Vishal Ranjan.

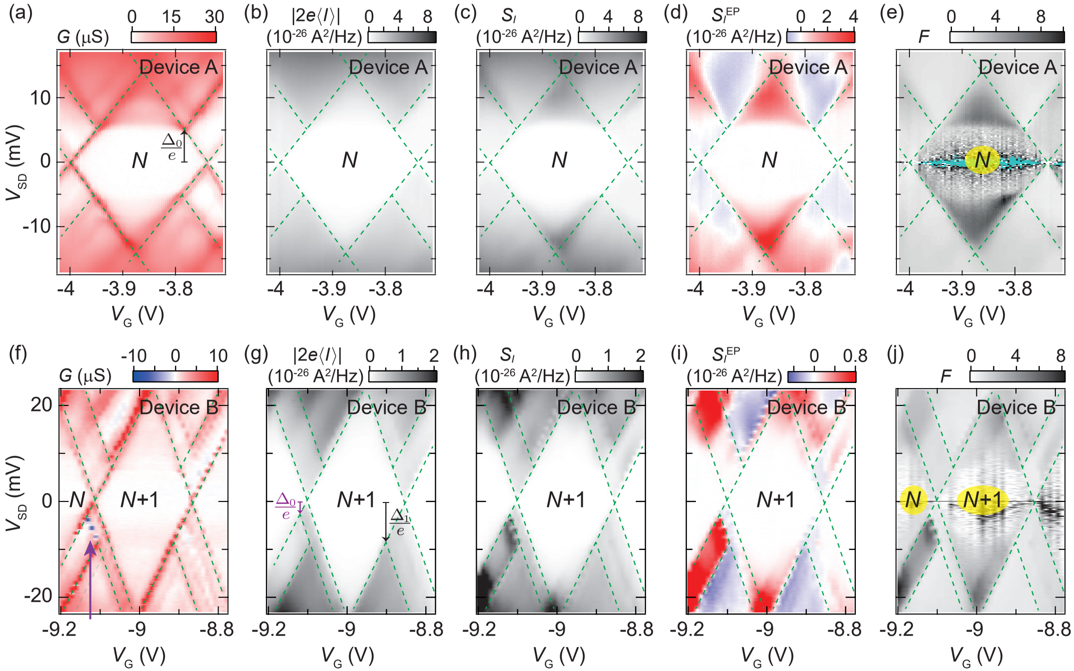

Figure 6.1. Conductance and noise measurements of device A (a-e) and device B (f-j). **(a),(f)** Differential conductance deduced from rf reflectance, as a function of bias voltage V_{SD} and side gate voltage V_{G}. Dashed green lines serve as guides for the eye; the same guides are overlaid in the remaining panels. The purple arrow in (f) points to a segment of negative differential conductance. **(b),(g)** The Schottky noise, $|2e\langle I\rangle|$, provides a comparison reference for current noise. **(c),(h)** Measured current noise spectral density, S_I. **(d),(i)** The excess noise, $S_I^{\mathrm{EP}} = S_I - |2e\langle I\rangle|$. **(e),(j)** The Fano factor, $F = S_I/|2e\langle I\rangle|$. Cyan areas inside the diamonds represent divergent domains, where uncertain noise values are divided by small currents.

The data of device A are plotted in figures 6.1a-e. Specifically, fig. 6.1a shows the differential conductance, as a function of bias voltage, V_{SD}, and side gate voltage, V_{G}. Fig. 6.1b depicts the noise spectral density reference, $S_{\mathrm{Poisson}} = |2e\langle I\rangle|$. This reference is calculated by scaling the measured current $\langle I\rangle$ with $2e$. Fig. 6.1c presents the measured noise spectral density, S_I, of the QD. Further, the enhanced noise is illustrated in two ways: the QD excess noise, $S_I^{\mathrm{EP}} = S_I - |2e\langle I\rangle|$, appears in fig. 6.1d and the Fano factor, $F = S_I/|2e\langle I\rangle|$, is mapped in fig. 6.1e.

Analogously, the data of device B are plotted in figures 6.1f-j.

Guides for the eyes highlight the main lines of the differential conductance maps. Both measurements show Coulomb diamonds, from the height of which we extract a charging energy of $U_{\mathrm{c}} \approx 15\,\mathrm{meV}$ (device A) and $U_{\mathrm{c}} \approx 20\,\mathrm{meV}$ (device B). The diamonds are labeled with the electron occupation number (e.g. N). Current through QDs usually consists of sequences in which one electron tunnels from a lead into the dot, increasing N by one, then tunnels out to the other lead, decreasing the charge of the QD—that is sequential tunneling. Each such electron hopping is called a first-order tunneling event. Inside the diamonds, as first-order tunneling is prohibited, the system is in Coulomb blockade.

Outside the diamonds, the blockade is lifted. Also here, the conductance plots exhibit high-G lines starting at a finite bias: about 5 mV (device A) and approximately 2 mV, 8 mV (device B). These lines originate from excited states at a fixed electronic occupation and their threshold bias corresponds to the excitation energy, provided by the bias voltage: $|eV_{\mathrm{SD}}| = \Delta_{0,1}$. We designate excited states with a star superscript, e.g. $|N^*\rangle$. Therefore, $\Delta_0 \approx 5$ meV for state $|N^*\rangle$ in device A and $\Delta_0 \approx 2$ meV, $\Delta_1 \approx 8$ meV for states $|N^*\rangle$, $|(N+1)^*\rangle$ in device B.

We now focus on device A. Inside Coulomb diamond N, in the absence of first-order tunneling, a low current still flows due to second-order tunneling (i.e. cotunneling). Cotunneling means that one charge passes coherently, in one event, through both tunnel barriers of the QD. In this process, the charge state of the QD is preserved. Elastic cotunneling does not change the final state of the QD and is possible at any value of the bias voltage. In contrast, inelastic cotunneling (IEC) alters the QD state, e.g. $N \to N^*$, the needed energy being provided by the bias voltage, $|eV_{\mathrm{SD}}| \geq \Delta_0$. Here, because we observe a conductance increase at the excitation bias, $|eV_{\mathrm{SD}}| = \Delta_0$ (fig. 6.1a), the crucial role is played by IEC. The IEC regime inside the Coulomb diamond appears also in the noise-related maps (fig. 6.1c-e), with a strong Fano factor enhancement of up to $F \approx 8$. Outside the Coulomb diamond, below the excited state lines one observes mostly $0.5 < F < 1$, as it is expected for transport in a double tunnel barrier [7, 61].

In the case of device B, the same Coulomb diamond inner structure can be observed as in device A, but the increase of conductance due to IEC is weaker. Another difference is the very pronounced line of negative differential conductance (NDC) starting from the Coulomb diamond N and here depicted in blue. While typically the current rises when the absolute bias voltage increases and a transition enters the bias window, as in device A, here the current is suppressed.

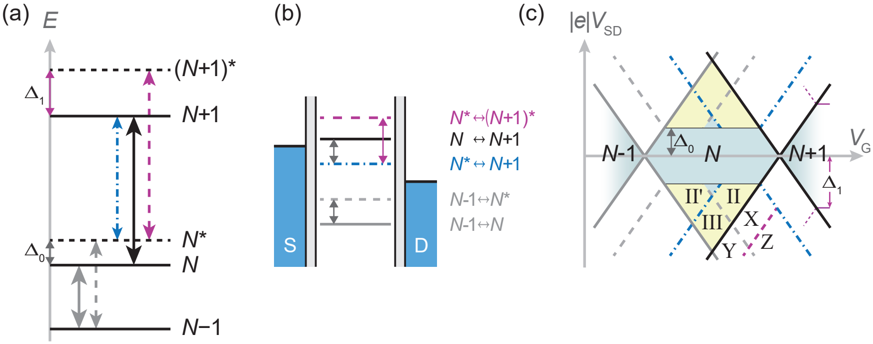

Figure 6.2. **(a)** Energy levels in the considered model, with transitions marked as arrows. **(b)** QD transitions represented as electrochemical-potential levels, whose positions are determined by the lengths of the transition arrows in (a). **(c)** Schematic stability diagram with relevant transitions. Positive- (negative-) slope lines depict resonances of the source (drain) Fermi level with the QD levels depicted in (b). The dashed arrows are excited lines.

However, the NDC ridge is confined to a segment, between the Coulomb diamond edge and a parallel line of high conductance. Regarding the noise produced in device B, the striking feature is the enhanced $F \approx 6$ just outside Coulomb diamond N, at negative bias. By comparing the the conductance and Fano factor maps, one can see that this region of enhanced noise is a band bordered by the NDC ridge and parallel to the Coulomb diamond edge.

To summarize, our two key findings are: (i) in device A, strongly super-Poissonian noise inside the Coulomb blockade, above a threshold voltage determined by an excited state and (ii) in device B, strongly super-Poissonian noise outside the Coulomb blockade, involving excited states. The origin of these two findings will be detailed in the following.

6.1.2. Model

In this section, we detail a simple model for our QDs, similar to the model used in ref. [67], and show how it is projected onto electrochemical-potential diagrams and further onto charge stability diagrams. Lastly, we place transport mechanisms on the stability diagram.

The QD is described by a spinless model, with states labeled by the electronic occupation number:

$$|N-1\rangle,\ |N\rangle,\ |N^*\rangle,\ |N+1\rangle,\ |(N+1)^*\rangle. \tag{6.1}$$

The star superscript denotes an excited state, e.g. $|N\rangle$ is a ground state, $|N^*\rangle$ is an excited state, and both states have N electrons. The corresponding QD energies are:

$$E_{N-1} = 0, \tag{6.2}$$

$$E_N = \epsilon_0, \qquad E_{N^*} = \epsilon_0 + \Delta_0, \tag{6.3}$$

$$E_{N+1} = 2\epsilon_0 + U_\mathrm{c}, \qquad E_{(N+1)^*} = 2\epsilon_0 + U_\mathrm{c} + \Delta_1, \tag{6.4}$$

where ϵ_0 is the kinetic and confinement energy of an additional charge and U_c is the charging energy for double occupancy. The excitation energies Δ_0 and Δ_1, differ from each other by virtue of many-body effects, are free parameters in our model.

Fig. 6.2a illustrates the energy levels (horizontal lines) and possible transitions between them. We order these transitions like in fig. 2.6 of chapter 2. The result of their ordering is fig. 6.2b, showing the chemical-potential diagram of the QD. The transitions pictured in a chemical-potential diagram are involved in tunneling; not drawn here, the internal excitation or relaxation are transitions between same-charge states, that do not involve tunneling.

Depicting transitions in a charge stability diagram is the aim of fig. 6.2c. Here, we remind the significance of various lines in the $(V_\mathrm{G}, V_\mathrm{SD})$ maps. Remark first the N-labeled Coulomb diamond. The underlying lines of this diamond's edges correspond to transitions to and from state $|N\rangle$: the left (right) edges represent transitions between $|N\rangle$ and $|N-1\rangle$ ($|N+1\rangle$). All sketched lines mark the alignment (resonance) of a chemical potential (fig. 6.2b) with the Fermi level of a lead: positive-slope lines indicate resonance with source, negative-slope lines indicate resonance with drain, as further exemplified in fig. 6.2e. Line graphic styles in fig. 6.2c are replicated from corresponding transitions in fig. 6.2b.

Before placing significant transport mechanisms on the stability diagram, we define several distinct regions delimited by excited lines, i.e. dashed lines, corresponding to transitions that involve the excited state $|N^*\rangle$. The typical excited lines are the lead-resonant $N \pm 1 \leftrightarrow N^*$ transitions. Outside the Coulomb diamond, they start at voltage biases $|eV_\mathrm{SD}| = \Delta_0$. Inside the diamond, together with the horizontal line $|e|V_\mathrm{SD} = -\Delta_0$, the excited lines form the regions II, II', III [55].

A particular excited line in fig. 6.2c is the purple one below diamond N. It corresponds to the source-resonant $N^* \leftrightarrow (N+1)^*$ transition. This excited line, together with its neighboring gray and blue excited lines, define below diamond N the regions X, Y, Z. One can establish that the right corner of X is situated at a bias $|e|V_\mathrm{SD} = -\Delta_1$. Indeed, in the charge stability diagram, two lines intersect at a bias given by their level difference in fig. 6.2b.

According to chapter 2, regions II and III exhibit *cotunneling-assisted sequential tunneling* (COSET) [55]. Indeed, they allow sequential tunneling because in the cone of transition $N^* \leftrightarrow N+1$. Moreover, the excited state $|N^*\rangle$, depopulated by relaxation, is repopulated at a strong enough rate by inelastic cotunneling, IEC. Detailed in fig. 2.8c,d, IEC is concisely denoted as $N \xrightarrow{N\pm1} N^*$. Between an IEC event and relaxation, the sequence undergone here by the QD state is $N^* \to N{+}1 \to N^* \to N{+}1 \to \ldots$ A similar reasoning can be done for regions II' and III. The regions II+III and II'+III, as well as their counterparts in positive bias, are COSET bands.

Region X, entirely laid under the cone of the lead-resonant $N \leftrightarrow N{+}1$ full black lines, is another example of domain with possible sequential tunneling.

6.1.3. Interpretation

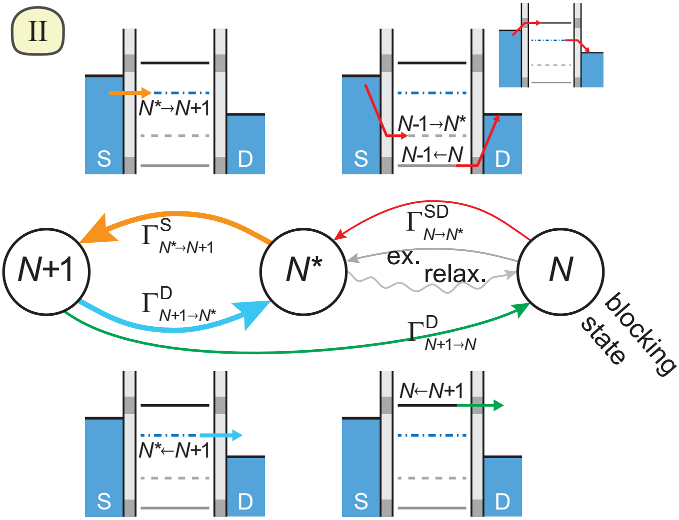

Figure 6.3. Quantum state graph with associated electrochemical-potential diagrams, for device A, region II. The gray rectangles in tunnel barriers stand for weaker tunneling via the neighboring transition. $|N\rangle$ is a blocking state, from which the quantum dot can escape only by low-rate processes (inelastic cotunneling in the second diagram; excitation). Elastic cotunneling is not displayed. In the bottom-right chemical-potential diagram, tunneling into S is equally possible.

We further investigate our noise data within the model, by looking for transitions through which tunneling is relatively weak. These may indicate a delayed-escape path from a reachable state. Such a particular state is referred below as a blocking state.

First, we match the large-Fano-factor data of the two devices onto labeled regions of fig. 6.2d. For device A, we expect inside diamond N the existence of regions II, II', III. For device B, we argue that the band below diamond N is region X. The involved processes are summarized in Figs. 6.3 and 6.4.

Inside the Coulomb diamond N of device A, IEC triangles are indicated by current and by differential-conductance lines (fig. 6.1b,a). The triangles are entirely covered by the COSET sidebands, composed by regions II, II', III. Hence, both IEC and sequential tunneling are present. Fig. 6.3 specifically illustrates that IEC breaks the blockade ($N \xrightarrow{N\pm1} N^*$, red arrow), being followed by sequential tunneling ($N^* \overset{\mathrm{S}}{\to} N{+}1 \overset{\mathrm{D}}{\to} N^* \overset{\mathrm{S}}{\to}$ etc., orange and blue arrows). The transport sequence is interrupted by spontaneous relaxation (wavy gray arrow) or by the $N+1 \to N$ transition (green arrow), both resulting in a return to the blocking state, $|N\rangle$. Because cotunneling is a second-order process, the IEC rate, $\Gamma^{\mathrm{S}D}_{N\to N^*}$, is relatively weak, hence the blocking time is relatively long. Thus, electronic-flow periods alternate with zero-current periods, implying telegraphic transport, i.e. augmented noise. This is indeed what the Fano factor map (fig. 6.1e) reveals. We stress here that the relaxation rate (wavy gray arrow) should be lower than the sequential-tunneling rates (orange and blue arrows) in order allow alternation of current and blocking periods, i.e. super-Poissonian noise.

Therefore, for device A we have pointed out a blocking state, $|N\rangle$, connected to other QD states by a low-rate tunneling process, IEC. The IEC rate is usually weak enough to assure an increased Fano factor. In the simple case of all-identical tunneling couplings, and zero relaxation rate, a theoretical value $F = 2$ is predicted [67]. Furthermore, F can be substantially boosted by reducing the IEC rate, e.g. when weakening the tunneling via transitions involved in IEC. The slower IEC escape keeps the QD in the blocking state a longer time and thus increases the transport telegraphicity. Impeded tunneling, resulting in rarer IEC, is graphically suggested in the chemical-potential diagrams of fig. 6.3 by gray rectangles in the two tunnel barriers, at the heights of the $N \leftrightarrow N \pm 1$ transitions.

Device B exhibits its highest Fano factor below diamond N, in a range that we will show corresponds to region X. The bias window of this region contains two transitions, $N^* \to N + 1$ and $N \to N + 1$ (see the chemical-potential diagrams in fig. 6.4X). Like for the other device, we explain, by means of a blocking state, the telegraphic transport signaled by the strong Fano factor. For that, we can suppose that one of the tunneling rates shown in the graph is weak. We assume for the moment that tunneling from source via transition $N^* \to N + 1$ is slow. Provided that the relaxation of $|N^*\rangle$ is slower or of same order, $|N^*\rangle$ becomes a blocking state. Leaving the blocking state through the transition $N^* \to N{+}1$ (magenta arrow) or through relaxation (gray arrow) triggers sequential tunneling (the transport sequence $N{+}1 \overset{\mathrm{D}}{\to} N \overset{\mathrm{S}}{\to} N{+}1 \overset{\mathrm{D}}{\to}$ etc., suggested by orange and blue arrows), ended when the systems falls back into $|N^*\rangle$. As opposed to COSET, the escape path to transport is not a second-order process (IEC), but a weakly lead-coupled tunneling event or internal relaxation. Because the blocking state is due to the weakly coupled tunneling, we are naming this phenomenon *sequential tunneling intermitted by weak coupling*, SETWEC. As in COSET, the telegraphic character of the transport induces an enhanced Fano factor.

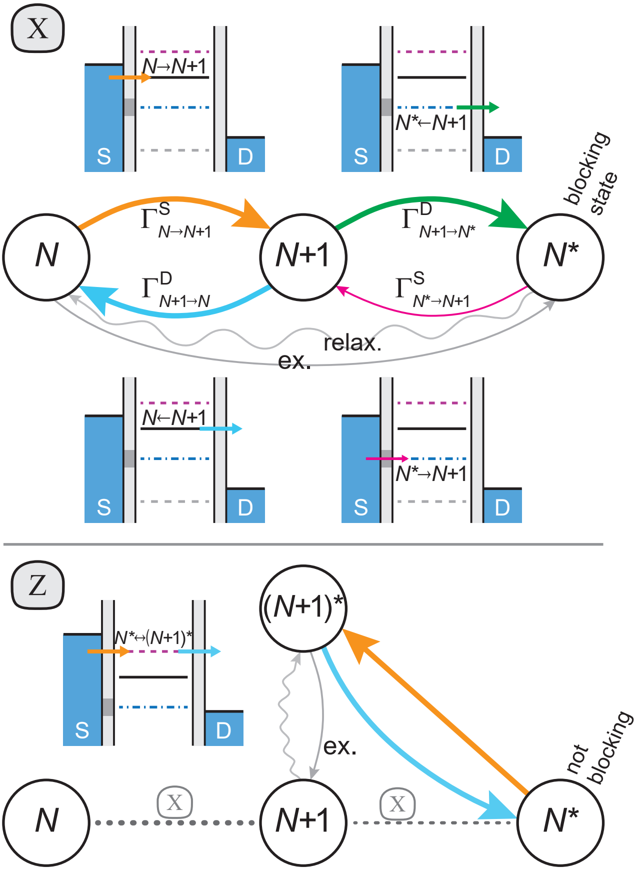

Figure 6.4. Quantum state graph with associated electrochemical-potential diagrams, for device B, regions X and Z. **(X)** $|N^*\rangle$ is a blocking state if the main escape process, namely tunneling from S via transition $N^* \to N{+}1$, is hindered (marked with a gray rectangle in the tunnel barrier). Cotunneling transitions are not displayed. **(Z)** In device B, region Z, an extra transition level enters the bias window, opening a high-rate escape path from state $|N^*\rangle$. This transition, $N^* \leftrightarrow (N+1)^*$ (orange and cyan arrows), is a SET channel. Hence, blocking is lifted.

We now justify for device B the choice of lowering $\Gamma^{\mathrm{S}}_{N*,N+1}$, over the other three options in the quantum state graph. For example, if $\Gamma^{\mathrm{D}}_{N*,N+1}$ were chosen, then the QD would not have a blocking state[2] (indeed, it would not stay in $|N+1\rangle$,

---

[2] Nonetheless, were the rate $\Gamma^{\mathrm{D}}_{N*,N+1}$ weak, a high-F band would rather appear in the

but would oscillate between $|N+1\rangle$ and $|N\rangle$). A similar situation would occur if $\Gamma^{\mathrm{D}}_{N,N+1}$ were lowered. However, if $\Gamma^{\mathrm{S}}_{N,N+1}$ were chosen instead, the QD would have $|N\rangle$ as a blocking state, instead of $|N^*\rangle$. This statement can immediately be explained by the symmetry of N and N^* in the graph of the QD states (fig. 6.4X). The difference between the two candidates is the transition that lifts the blocking state if entering the bias window: $|N^{(*)}\rangle$ is lifted by a transition from this state, namely the source-resonant $N^{(*)} \to (N+1)^*$. This transition is also the bottom-right edge of the high-F band. Our choice, leading to the edge $N^* \to (N+1)^*$, is therefore the correct one. We remind that the right corner of region X and that of the measured high-F band are the same bias, $|e|V_{\mathrm{SD}} = -\Delta_1$.

Lifting of the blocking state

We extend the discussion over the blocking state in device B, by analyzing where it is lifted.[3] in general, blocking is due to the low rate of the escape paths from a certain state. Adding a high-rate escape path, through e.g. a new transition level in the bias window, is logically expected to lift blocking. The SETWEC region of device B lies between the Coulomb diamond and a region of sub-Poissonian noise—region Z. The noise level of region Z indicates that the blocking is lifted. We schematize the new transport processes of this region in fig. 6.4Z. We show that the extra transition involves the initially blocking state, $|N^*\rangle$, and the excited state of the next diamond, $|(N+1)^*\rangle$. Thanks to it, an alternative escape path from $|N^*\rangle$ is available. Moreover, the new transition allows sequential tunneling and thus reestablishes transport through the QD. Further numerical simulations confirm this interpretation.

We retain that the SETWEC band apposed to a Coulomb diamond (CD) is delimited by the next available line involving the blocking state. The next chapter will detail a similar finding, but in the case of COSET.

Occurrence of negative differential conductance

Subsequently, we discuss qualitatively the presence of the differential conductance at some boundaries of the studied regions. For device A, we place ourselves in region II. If the bias voltage increases such that transition $N \leftrightarrow N+1$ enters the bias window, one goes outside region II, across the Coulomb diamond edge. In consequence, the quantum state graph (fig. 6.3) gains one arrow, from $|N\rangle$ to $|N+1\rangle$. The electronic transport consists now not only of rare cotunneling events (e.g. $N \to N^*$, red arrow) and sequential tunneling through level $N^* \leftrightarrow N+1$ (loop of orange and cyan arrows), but also sequential tunneling through level $N \leftrightarrow N+1$ (loop formed by the green arrow and the newly added arrow). The orange-cyan loop is faster than the new loop because of higher tunneling

---

positive-bias domain.

[3] Credits go to Roy Haller and Gergő Fülöp, with whom I analyzed blocking states.

rates; indeed, transition $N^* \leftrightarrow N+1$ is more strongly connected to leads than $N \leftrightarrow N+1$. If including the latter in the bias window would only result in the replacement of some faster sequences by slower sequences, then the current would diminish (and the Coulomb diamond edge would exhibit NDC). However, below region II, current grows (meaning positive differential conductance on the Coulomb diamond edge) because access to the fast, orange-cyan loop solidly increases: in region II, this access is granted by inelastic cotunneling (red arrow) and excitation; below region II, it is substantially raised by transition $N \to N+1$.

For device B, transport in region X (fig. 6.4) is carried by fast and slow tunneling sequences (orange-cyan and green-red loops, respectively). If the bias voltage decreases such that the weakly coupled transition, $N^* \to N+1$, exits the bias window, only the fast, orange-cyan loop remains in the quantum state graph. Hence, each slow tunneling sequence is substituted by several fast sequences. Therefore, the bias voltage decrease results in a current increase, synonym to NDC on the crossed boundary of region X. In a charge stability diagram, this boundary is the line given by the resonance between level $N^* \to N+1$ and the drain. If the weakly coupled transition were $N \to N+1$ instead of $N^* \to N+1$, then the NDC line candidate would be a different boundary of region X, namely the Coulomb diamond edge; yet, NDC would not occur here, for reasons exposed for device A, region II.

6.1.4. Numerical simulations

In order to validate our interpretations, we run numerical simulations. To calculate the conductance and the current noise, we employ the master equation approach developed in ref. [67]. The master equation describes transitions between the QD states due to (a) first- and second-order tunneling trough the barriers of the QD and (b) internal relaxation and excitation. The transition rates can be found in [67].

For both devices, we simulate three Coulomb diamonds, labeled again as $N-1$, N, and $N+1$. The charging energy is $U_\mathrm{c} = 1$ meV. We set the temperature $k_B T = 4 \cdot 10^{-3}\ U_\mathrm{c}$. The maximal tunneling rate is symmetrically chosen, $\Gamma^\mathrm{S} = \Gamma^\mathrm{D} = \Gamma_0 = 10^{-3}\ U_\mathrm{c}/\hbar$. (A tunneling rate through lead α is proportional to Γ^α; a cotunneling rate is proportional to $\Gamma^\mathrm{S}\Gamma^\mathrm{D}$.) Tunneling rates are also related to tunneling amplitudes. If $t^\alpha_{N,M}$ is the amplitude of tunneling from lead α into the QD, such that the QD state undergoes the transition $N \to M$ (see formal definition in appendix C), then the corresponding tunneling rate is:

$$\Gamma^\alpha_{N\to M} \propto \Gamma^\alpha |t^\alpha_{N,M}|^2. \tag{6.5}$$

The relaxation rates are $10^{-3}\ \Gamma_0$, unless specified. The excitation rates, proportional to the respective relaxation rates, are described by the Bose-Einstein distribution function.

To reproduce the essential features of our data, our calculation utilizes a minimal number of states and a small number of distinct tunneling amplitudes. A more detailed reproduction can be further obtained with more parameters.

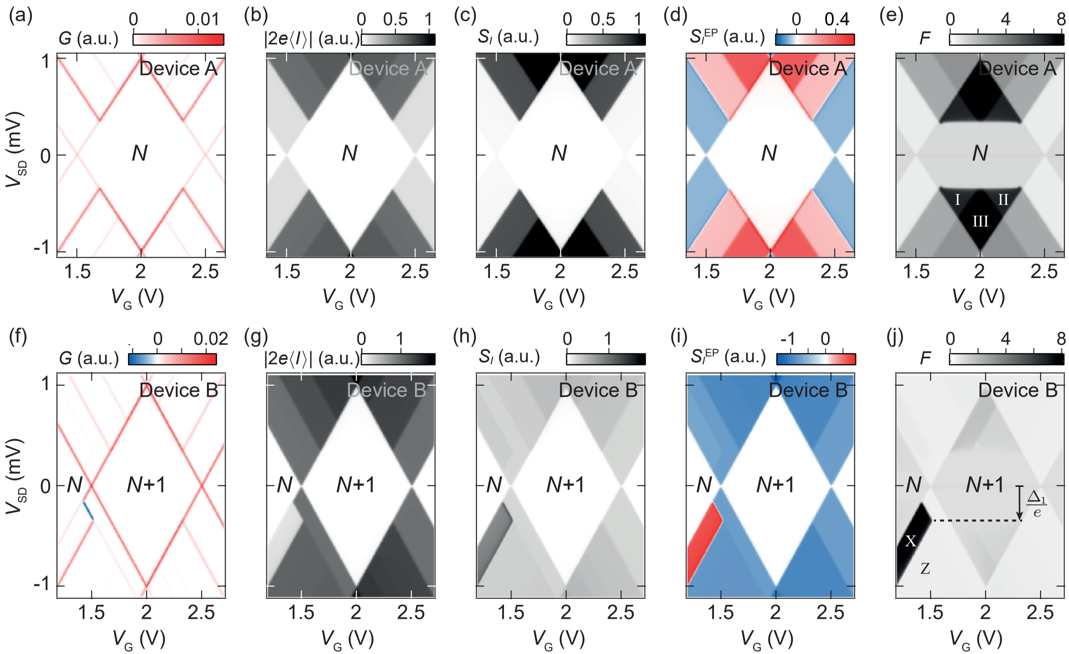

Figure 6.5. Numerical calculations of conductance G and Fano F factor for **(a-e)** device A ($t^{\mathrm{S|D}}_{N,N\pm1} = 0.33$) and **(f-j)** device B ($t^{\mathrm{S}}_{N*,N+1} = 0.1$, $t^{\mathrm{D}}_{N*,N+1} = 0.4$, the relaxation rate for the excited state of N+1 is Γ). All other t amplitudes are 1. The maximal tunneling rates are $\Gamma^{\mathrm{S|D}} = \Gamma = 10^{-3}\ U_{\mathrm{c}}/\hbar$ and the relaxation rate is $10^{-3}\ \Gamma$. In device A, F is enhanced in regions I, II, III. In device B, F is significantly high in region X, whose top corner is characterized by a bias voltage $-\Delta_0/|e|$ and right corner by $-\Delta_1/|e|$.

For the simulation of device A (fig. 6.5a-e), an excited state is introduced at $\Delta_0 = 0.35 \cdot U_\mathrm{c}$ above the ground state $|N\rangle$. We weaken tunneling for ground-state transitions ($t^{\mathrm{S|D}}_{N,N\pm1} = 0.33$, while all other t amplitudes are 1) to obtain high Fano factor values, $F > 8$, inside Coulomb diamond N at absolute bias voltages greater than $\Delta_0/|e|$. The maximal value of F is therefore in good agreement with the measurement. The simplicity of the tunneling amplitude set of values wipes out only some nuances of the measured data.

For the simulation of device B (fig. 6.5f-j), an excited state is defined at $\Delta_0 = 0.15 \cdot U_c$ above the ground state $|N\rangle$ and another one at $\Delta_1 = 0.35 \cdot U_c$ above the ground state $|N+1\rangle$. By relatively weakening the source-QD tunneling via transition $N^* \leftrightarrow N+1$ ($t^{\mathrm{S}}_{N^*,N+1} = 0.1$, versus $t^{\mathrm{D}}_{N^*,N+1} = 0.4$), an enhanced Fano factor region appears beneath the N diamond and an NDC line sets in at the top of this region, exactly as in the measurement. The emerged high-F band, labeled X, has its rightmost corner placed at $V_\mathrm{SD} = -\Delta_1/|e|$ and its southeastern edge situated between diamond N and the excited line $N \leftrightarrow (N+1)^*$; the only transition corresponding to this position is, like in our interpretation, $N^* \leftrightarrow (N+1)^*$. We note that without including the excited state $(N+1)^*$ in the model, this escape process is absent and region X extends infinitely, as shown in [67]. Further parameters were tuned in the calculation for the secondary purpose of reducing the conductance of the excited line $N \leftrightarrow (N+1)^*$ resonant with the source: $t^{\mathrm{S}}_{N,(N+1)^*} = 0.1$.

Obtaining Fano factor values beyond certain thresholds is not possible without an extra ingredient, on which we elaborate here. As derived in ref. [32], the Fano factor of the super-Poissonian noise in a telegraphic system is described by the expression

$$F = 1 + 2\langle n\rangle P_\mathrm{off}^2, \tag{6.6}$$

where $\langle n\rangle$ is the average number of electrons in a sequential-tunneling bunch and P_off the occupation probability of the blocking state. A simple analysis, done in the absence of internal relaxation and excitation, is presented in section 6.2. It shows that a higher P_off is produced when the blocking-state escape rate is lower than the other tunneling rates. P_off approaches 1 in the case of a strongly blocking state. The additional ingredient, $\langle n\rangle$, is given by the relative strength of the tunneling path that keeps the current on. Concretely, we demonstrate that $\langle n\rangle$ is the ratio of the rates illustrated by the cyan and the green arrow respectively (Figs. 6.3, 6.4). With all tunneling rates equal except for the escape path, Eq. 6.6 leads to $F \leq 3$. A simulation of device B confirms the limit $F \simeq 3$ in the special case $P_\mathrm{off} \simeq 1$ (namely, when tunneling out of the blocking state is extremely low). Our general calculations do reach Fano factors above 3 because of the risen number of charges in a bunch, caused by the tunneling imbalances $t^{\mathrm{D}}_{N^*,N+1}/t^{\mathrm{S|D}}_{N,N+1} = 1 : 0.33$ (device A) and $t^{\mathrm{D}}_{N,N+1}/t^{\mathrm{D}}_{N^*,N+1} = 1 : 0.4$ (device B).

6.1.5. Conclusions

We identify Fano factor corresponding to markedly super-Poissonian noise in two devices. We propose a model which allows to explain the observed $F > 1$ regions in a consistent way. In the exposure of the underlying quantum transport processes, we show that the concept of blocking state is central in the occurrence of enhanced noise. Escaping the blocking state leads to electronic flow for a certain time, until the system falls back into the blocking state. This gives rise to a telegraphic pattern of charge transport, consisting of a random set of charge packages, which determines the enhanced Fano factor. We have identified and proven two mechanisms that can generate telegraphic transport: (i) In COSET (cotunneling-assisted electron tunneling) the blocking state is the ground state of the Coulomb blockade and can be left by cotunneling. If it is fled to an excited state, a transport channel may open. (ii) Outside the Coulomb blockade, when the bias window contains two coupled transitions involving the same charge states, e.g. $N \leftrightarrow N{+}1$ and $N^* \leftrightarrow N{+}1$. If one state, e.g. $|N^*\rangle$, is weakly coupled, then it becomes a blocking state, causing again telegraphic transport. We term this process sequential tunneling intermitted by weak coupling (SETWEC). SETWEC can be accompanied by negative differential conductance.

6.2. Telegraphicity, enhanced noise and negative differential conductance

Here, we first explore a quantitative link between telegraphicity and enhanced noise, applicable to the two-level system we analyzed outside the Coulomb diamond. Second, we study the overlap of super-Poissonian noise and negative differential conductance, when a loosely coupled chemical-potential level enters the bias window.

6.2.1. Telegraphic transport and Fano factor[4]

The Fano factor in the telegraphic picture can be written as $F = 1{+}2\langle n\rangle P_{\mathrm{off}}^2$ [32]. Here we apply this formula to a specific case and derive expressions for its two ingredients: the probability of the QD to be off, P_{off}, and the average number of electrons in a bunch, $\langle n\rangle$. A bunch is a package of charge carriers that flow one by one through the QD. The QD is considered to be off when no bunch is flowing through.

We evaluate a QD with states $|N\rangle$, $|N^*\rangle$, $|N+1\rangle$ and transition rates $\gamma_{1,2,3,4}$, as shown in fig. 6.6. This is a simplified model of device B in region X (compare with fig. 6.4). We assume that the transport is unidirectional, i.e. the QD is always filled from the source electrode, and emptied into the drain. This is ensured by the

---

[4] This subsection is part of our *Physical Review B* article [66].

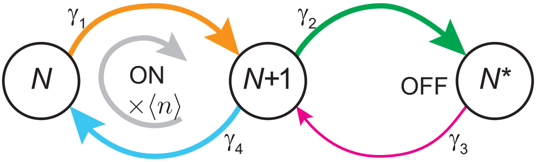

Figure 6.6. Graph of quantum states for a QD that exhibits telegraphic transport. While the QD oscillates in the left loop ($N+1 \leftrightarrow N$), the current is switched on and an average number of $\langle n \rangle$ electrons tunnel sequentially from source into the QD and farther into the drain. $|N^*\rangle$ is the blocking state. Cotunneling and internal excitation and relaxation are not taken into account.

bias voltage. The QD exhibits telegraphic transport if, for instance, the escape rate from state $|N^*\rangle$ is much lower than the rates in the left loop ($N+1 \leftrightarrow N$). We formulate a master equation for the probabilities p_j to be in state $|j\rangle$:

$$\frac{d}{dt}\begin{pmatrix} p_N \\ p_{N^*} \\ p_{N+1} \end{pmatrix} = \begin{pmatrix} -\gamma_1 & 0 & \gamma_4 \\ 0 & -\gamma_3 & \gamma_2 \\ \gamma_1 & \gamma_3 & -\gamma_2-\gamma_4 \end{pmatrix} \begin{pmatrix} p_N \\ p_{N^*} \\ p_{N+1} \end{pmatrix}. \tag{6.7}$$

By solving the master equation in the steady state, $d\mathbf{p}/dt = 0$, we find the occupation probability of state $|N^*\rangle$:

$$p_{N^*} = \frac{\gamma_1\gamma_2}{\gamma_1\gamma_2 + (\gamma_1+\gamma_4)\gamma_3}. \tag{6.8}$$

For an escape rate much smaller than the falling rate, $\gamma_3 \ll \gamma_2$, the off state of the system is equivalent to being in the blocking state: $P_{\text{off}} = p_{N^*}$. Eq. 6.8 already shows that a bigger $P_{\text{off}} = p_{N^*}$ is produced by smaller values of the escape rate, γ_3. With $\gamma_3 \ll \gamma_2$ and $\gamma_4 \lesssim \gamma_1$, one gets

$$P_{\text{off}} \simeq 1 - \frac{\gamma_4}{\gamma_1}\frac{\gamma_3}{\gamma_2} \simeq 1. \tag{6.9}$$

In this limit, essentially the number of electrons in a bunch, $\langle n \rangle$, determines Fano factor.

The average number of electrons in one bunch is

$$\langle n \rangle = \frac{\gamma_4}{\gamma_2} \tag{6.10}$$

and can be derived as follows: In state $|N+1\rangle$, the probability to fall in the blocking state, $|N^*\rangle$, is $p_b = \gamma_2/(\gamma_2+\gamma_4)$, while the probability to go to state $|N\rangle$ is $\tilde{p}_b \equiv 1-p_b$. Therefore, the probability that n electrons sequentially tunnel before blocking is $P(n) = \tilde{p}_b^n p_b$. The average number of electrons in the sequential-tunneling bunch, $\langle n \rangle = \sum_{n=0}^{\infty} nP(n) = p_b \partial_{\tilde{p}_b} \sum_{n=0}^{\infty} \tilde{p}_b^n = \tilde{p}_b/p_b = \gamma_4/\gamma_2$, reads as in Eq. 6.10. In this analysis, the electron that tunnels into the QD and switches it on ($N^* \rightarrow N+1$) is not considered to belong to the consequent bunch. In conclusion, under the condition of slow escape from a blocking state, super-Poissonian noise can still substantially grow from the imbalance of tunneling rates related to the pre-blocking state, $|N+1\rangle$.

A limit case arises when tunneling out of $|N+1\rangle$ is balanced: $\gamma_4 = \gamma_2$. In this situation, super-Poissonian noise is characterized by a Fano factor $F = 1+2P_{\text{off}}^2 \leq 3$. If in addition $\gamma_3/\gamma_2 \rightarrow 0$, then $F \rightarrow 3$.

A similar analysis can be done for a QD described by the state graph of fig. 6.3, in the absence of cotunneling and internal excitation and relaxation.

6.2.2. *F* versus NDC

The question arises if negative differential conductance (NDC) always implies super-Poissonian noise, $F > 1$. To answer this question, we consider a quantum dot with two electro-chemical potential levels, e.g. $N \leftrightarrow N+1$ and $N^* \leftrightarrow N+1$. When both levels are in the bias window, the state graph of the QD is the one pictured by fig. 6.6. When only the $N \leftrightarrow N+1$ transition is in the bias window, the state graph contains only the left loop of fig. 6.6. We redraw these two situations in fig. 6.7. For simplification, we neglect cotunneling, excitation and relaxation; we consider constant tunneling rates.

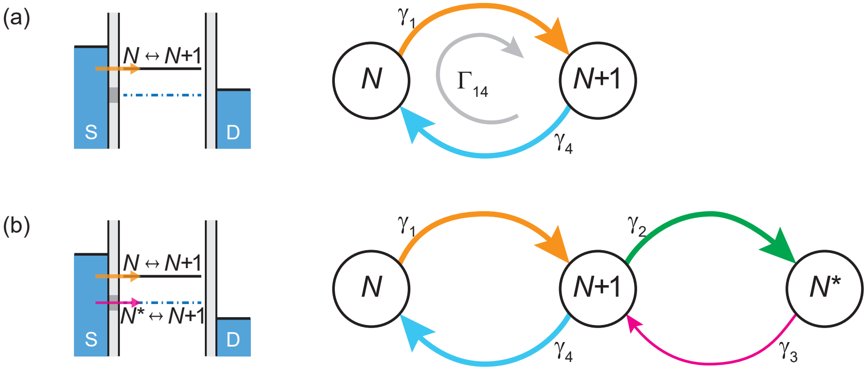

Figure 6.7. Comparison of two bias voltage regimes that differ by one transition level in the bias window. **(a)** Chemical-potential diagram and state graph for a QD with only one available transition. **(b)** Chemical-potential diagram and state graph for a QD with two available transitions. The extra transition level enters the bias window due to a bias increase: $|V_{\text{SD}}^{\text{b}}| > |V_{\text{SD}}^{\text{a}}|$.

NDC emergence

Negative differential conductance occurs if, although the bias increased to include a new transition, the electric current decreases:

$$|I_\mathrm{b}| < |I_\mathrm{a}|. \tag{6.11}$$

The current through the QD can be expressed by looking at the flow through one lead, e.g. the source (S):

$$|I_\mathrm{a}| = p_N\gamma_1|e| \quad \text{or} \quad |I_\mathrm{b}| = (p_N\gamma_1 + p_{N^*}\gamma_3)|e|,$$

with p_j the occupation probability of state $|j\rangle$. The probabilities p_j in the two cases (a and b) can be calculated with master equations. The stationary flow in the one-level case is described by (see graph in fig. 6.7a) $p_N\gamma_1 = p_{N+1}\gamma_4$, with $p_N + p_{N+1} = 1$. Therefore,

$$|I_\mathrm{a}| = \frac{\gamma_1\gamma_4}{\gamma_1 + \gamma_4}|e| = \Gamma_{14}|e|. \tag{6.12}$$

$\Gamma_{14}^{-1} \equiv \gamma_1^{-1} + \gamma_4^{-1}$ is the average time that an electron spends in the one-level QD of fig. 6.7; Γ_{14} is the rate at which one electron is transferred between leads.

The two-level case involves the probabilities given by eq. 6.7 and its corresponding current reads:

$$|I_\mathrm{b}| = \gamma_1\gamma_3\frac{\gamma_2 + \gamma_4}{\gamma_1\gamma_2 + \gamma_3\gamma_4 + \gamma_1\gamma_3}|e|. \tag{6.13}$$

The regime of negative differential conductance is therefore equivalent, by virtue of relations 6.11, 6.12, 6.13, to the inequality:

$$\boxed{\gamma_3 < \frac{\gamma_1\gamma_4}{\gamma_1 + \gamma_4} = \Gamma_{14}.} \tag{6.14}$$

Interestingly, the *falling rate*, γ_2, is not involved in the NDC emergence.

This is a general result in the sense that NDC occurs if and only if the so-called escape rate of the newly included transition is lower than the rate at which an electron was transferred between leads. In terms of time, NDC appears only when the average escape time is larger than the average time spent by the electron in the one-level QD.

If the first level is symmetrically coupled, $\gamma_1 = \gamma_4 = \gamma$, then one deduces from eq. 6.14 that NDC arises from an escape rate

$$\gamma_3 < \frac{\gamma}{2}. \tag{6.15}$$

Rate imbalance and *F*

It is known that the Fano factor, F, of a one-level system lies between $1/2$ and 1 (see chapter 3). Adding one level to the QD changes F. We use full counting statistics to calculate the Fano factor of a two-level QD, for a convenient range of the escape rate, γ_3. We plot the calculated F and investigate where super-Poissonian noise, $F > 1$, arises.

We choose to work in the limit $\gamma_1 = \gamma_4 \equiv \gamma$, i.e. before the addition of the new transition, the bias window contains only one transition, $N \leftrightarrow N+1$, symmetrically coupled to leads (see fig. 6.7). We define the escape rate and the falling rate in relation to γ:

$$\gamma_3 = \frac{\gamma}{m} \quad \text{and} \quad \gamma_2 = \frac{\gamma}{n}.$$

As stated above (ineq. 6.15), NDC exists only at $m > 2$. The dependence $F(m)$ plotted in fig. 6.8 shows that super-Poissonian noise emerges in a more restrictive domain of m. We analyze two cases of falling rates:

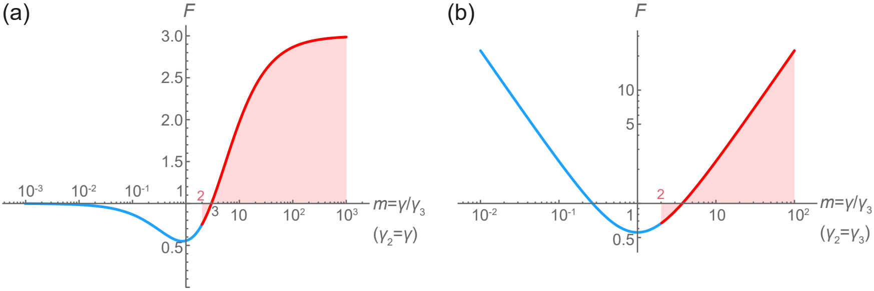

Figure 6.8. The Fano factor as function of the normalized escape time, $m = \gamma/\gamma_3$, where γ is the tunneling rate in the symmetrically coupled first transition. The red part of the curve indicates the NDC domain. **(a)** $F(m)$ for the fixed falling rate $\gamma_2 = \gamma$, that is $n = 1$, in a linear-log plane. **(b)** $F(m)$ for a falling rate, γ_2, equal to the escape rate, i.e. $n = m$. The curve lies in a log-log plane.

- n=1 (from state $|N+1\rangle$, the QD goes with equal probability into $|N\rangle$ and $|N^*\rangle$), illustrated in fig. 6.8a. Super-Poissonian noise sets in at $m = 3$ (i.e. the escape rate from state $|N^*\rangle$ is $\gamma/3$). At a very slow escape ($m \geq 1$), the Fano factor goes asymptotically to 3, as predicted by eq. 6.6 and discussed in subsection 6.2.1.

- n=m (falling into the new state, $|N^*\rangle$, is as likely as escaping from it), illustrated in fig. 6.8b. Super-Poissonian noise emerges at $3 < m < 4$ and the Fano factor is not bound at very low escape rates. The curve is symmetric in logarithmic scale because at high escape rates ($m < 1$), $|N\rangle$ and $|N^*\rangle$ swap places, i.e. the role of blocking state is taken by $|N\rangle$.

In conclusion, not only do NDC and super-Poissonian noise not exactly overlap, but they can also occur independently.

7 Cotunneling outside Coulomb Diamonds

This shorter chapter, built on foundations lied by chapter 6, analyzes a COSET-like triangle that overflows outside the Coulomb diamond (CD). Consider the second CD of our measurement (figures 5.3d, 5.7d), replotted here in the noise map fig. 7.1a. Let us employ again the label $N+1$ for this diamond. Its upper inelastic-cotunneling (IEC) triangle is not delimited, on the left side, by the diamond edge, as it is often the case with other diamonds (e.g. the first diamond, N). This means that the transition $N \leftrightarrow N+1$, when source-resonant or in the bias window, does not offer an alternative, high-rated escape path from $|N+1\rangle$, the blocking state of diamond $N+1$. Hence, the additional escape path on and beyond the discussed diamond edge, $N+1 \overset{\mathrm{S}}{\to} N$, is also very low-rated. In terms of tunneling amplitudes, this reads:

$$\left|t^{\mathrm{S}}_{N+1\to N}\right| \sim \left|t^{\mathrm{DS}}_{N+1\to(N+1)^*}\right| , \tag{7.1}$$

where the last amplitude characterizes IEC in diamond $N+1$ and is relatively low because it describes a a second-order process. We say that the source-resonant line $N \leftrightarrow N+1$ is weak, or weakly coupled.

With the above conclusion, one can try to qualitatively reproduce the data by way of numerical simulations based on full counting statistics (FCS), like in chapter 6. The result of such a simulation is presented in fig. 7.1b, for $t^{\mathrm{S}}_{N\leftrightarrow N+1} = 0.04$ and one excited state per diamond ($|N^*\rangle$, $|(N+1)^*\rangle$). We can see not only the data-like IEC-triangle overflow from diamond $N+1$, but also an IEC-triangle overflow from diamond N across the same weakened line, in the negative bias. In the following, we show how this situation can be transformed into one similar to the measurement.

First, we observe where COSET-related blocking is lifted. Here, blocking does not disappear when crossing the source-resonant ground state line (the diamond edge), since we have weakened it. It is lifted beyond the first resonant line that involves the COSET blocking state (the blocking state in a COSET triangle of diamond M is $|M\rangle$):

- source-resonant line $N^* \leftrightarrow N+1$ lifts the blocking related to overflown COSET triangle $N+1$;
- source-resonant line $N \leftrightarrow (N+1)^*$ lifts the blocking related to simulated overflown COSET triangle N;

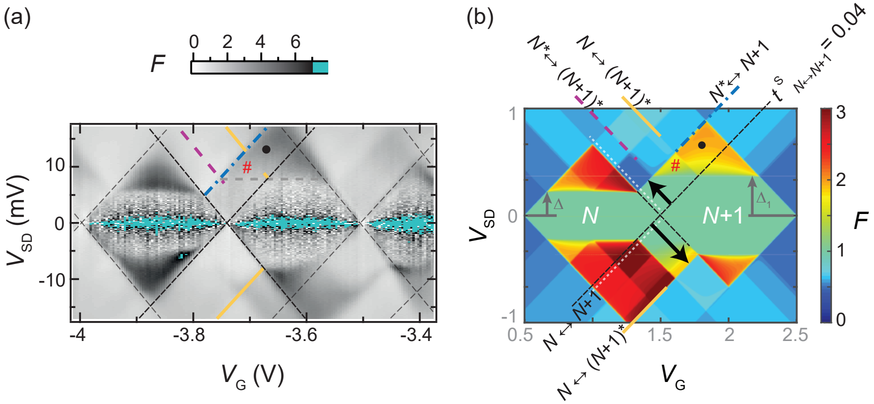

Figure 7.1. **(a)** Fano factor data for the first two Coulomb diamonds of the measurement. Added guide lines are drawn over the diamond edges and several excited lines. The bottom of the overflowing IEC triangle is indicated with a dashed segment. **(b)** Fano factor FCS simulation of two diamonds with excited lines, for a very low source-coupling (t^S) of the ground state transition $N \leftrightarrow N+1$. Several lead-resonant lines are indicated. The two white dashed lines are not related to the simulation.

In last chapter, we met an analogous condition in lifting SETWEC-related blocking, where the blocking state was $|N^*\rangle$ and the SETWEC region was ended by the next available N^* line. Thus, the general pattern is that blocking is lifted at the closest resonant line which is not weak (i.e. the transition is coupled strongly enough to the resonant lead) and which involves the blocking state.

Second, we observe in the conductance data a possible excited line of Coulomb diamond $N+1$, next to the bottom edge of diamond N (fig. 5.3d). Extra features in the left corner of diamond $N+1$ seem to sustain the excited character of the line. Let us denote this additional excited state by $|(N+1)^+\rangle$. On top of the simulated Fano factor map, fig. 7.1b, we mark with white dashed lines the new source- and drain-resonant transitions $N \leftrightarrow (N+1)^+$. With the above finding about blocking lifting, we now understand that the simulated overflown COSET triangle N should end at the source-resonant $N \leftrightarrow (N+1)^+$ line, being therefore barely visible. However, the new state would have no effect on the overflown COSET triangle $N+1$.

Having justified the relation between the weakly source-coupled transition $N \leftrightarrow N+1$ and the existence of only one overflown COSET triangle, we can now detail the transport processes in the COSET band situated outside the Coulomb diamond. For region # we show the graph of quantum states with transitions between them (fig. 7.2). We see that, like inside the CD, $|N+1\rangle$ is the blocking

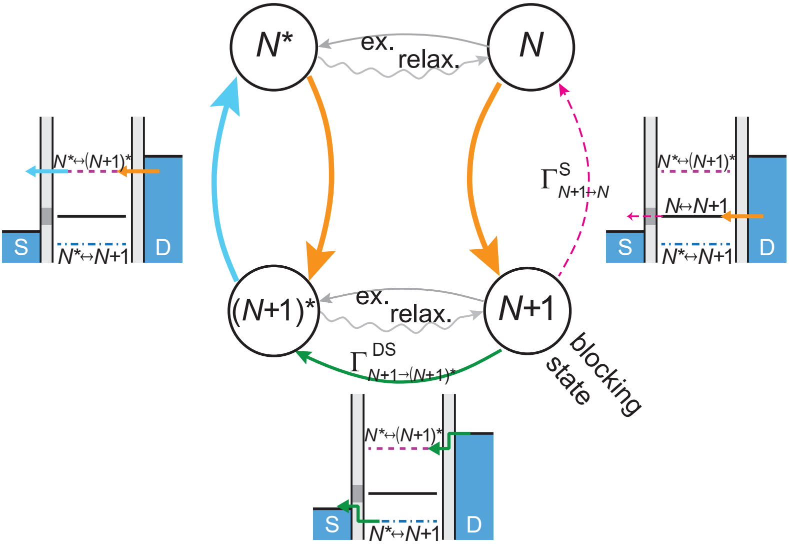

Figure 7.2. Quantum state graph with associated electrochemical-potential diagrams, for region # in the maps of fig. 7.1. Tunneling through source via transition $N+1 \to N$ is graphically marked as slow (gray rectangle).

state. The IEC transition $N+1 \overset{\text{DS}}{\to} (N+1)^*$ is still an escape path, to a state from which SET is possible. The tunneling transition $N+1 \overset{\text{S}}{\to} N$ is another escape path, of low rate (eq. 7.1); it leads to a state from which the QD falls back into the blocking state. In consequence, the transport regime in the # region is still cotunneling-assisted sequential tunneling, COSET.

This graph is valid for the above simulation, but also in the case of an additional excited state, $|(N+1)^+\rangle$: one should either just add $(N+1)^+$ in the circle of $(N+1)^*$ or explicitly replicate this circle with its arrows.

Transport in the region marked with a bullet (•) of the above maps is also based on the state graph of fig. 7.2, to which the SET-allowing transition $N \leftrightarrow (N+1)^*$ should be added. The difference is now that escaping from the blocking state via $N+1 \overset{\text{S}}{\to} N$ can lead to SET transport. Therefore, the bullet-marked region presents a combination of COSET and SETWEC.

A last question to address is why we still measure a Fano factor $F > 1$ in positive bias above diamond $N+1$, but below the marked overflown COSET triangle (fig. 7.1a). This is explained by COSET through the additional excited state, $|(N+1)^+\rangle$. Hence, we reside here in a larger COSET triangle.

Summary and Outlook

Electronic-transport phenomena in a quantum system are most often investigated by measuring the electric-current response of that system when subjected to different voltages. In other words, exploring electrical quantum devices usually starts with building their conductance maps. In such conductance-driven investigations, low-frequency or dc signals are most common. Complementary to conductance, other types of voltage-triggered responses can also be inspected. In this thesis, current noise is measured, at microwave frequencies. We show how both noise and conductance maps shed light on aspects of electron flow in quantum dots, namely on concurrent transport channels.

Carrying experiments in the microwave spectrum adds complexity to the circuit design. Indeed, the typical circuit scale is not short enough for ignoring the wave aspect of the electrical signals. Due to reflections, power transfer between circuit components is affected; this problem is lifted by implementing impedance-matching techniques.

In this thesis, we designed and fabricated lumped-element resonators, for the purpose of integrating carbon nanotube quantum dots into a microwave measurement setup. The on-chip coil had the geometrical constraint of connecting the inner end to the setup, through a bridge. We explored two possibilities: a bridge laying on a support and a bonded airbridge. The second one proved to be simpler to realize and more reliable.

Afterwards, we ran dc current, reflectance, and noise measurements. We selected data with intense noise features and, with the help of numerical simulations based on a master equation, we identified transport phenomena in quantum dots. These phenomena are generated by the existence of blocking states.

At the end, we applied the quantum transport findings in explaining regions of enhanced noise outside the Coulomb diamond (CD), but prolonging a CD-specific region, namely an inelastic-tunneling triangle.

An additional finding emerged in the attempts to fit the measured data. We showed that our resonator is modeled with a feed-forward capacitance across the coil, boosting the effective value of the inductance. This can be used in future designs, in order to improve the characteristic impedance of the resonator.

This work will be continued with the fabrication of resonators in superconducting films with high kinetic inductance [68, 69]. Such an option eliminates the need of a bridge, as the spiral can be replaced with a meander. It can miniaturize further the resonator and increase even more the characteristic impedance.

Bibliography

[1] M. H. Devoret, A. Wallraff, and J. M. Martinis, *Superconducting Qubits : A Short Review*, arXiv (2008), arXiv:0411174v1 [arXiv:cond-mat] .

[2] A. Wallraff, D. I. Schuster, A. Blais, L. Frunzio, R.-S. Huang, J. Majer, S. Kumar, S. M. Girvin, and R. J. Schoelkopf, *Strong coupling of a single photon to a superconducting qubit using circuit quantum electrodynamics*, Nature **431**, 162 (2004).

[3] S. Haroche, *Nobel Lecture: Controlling photons in a box and exploring the quantum to classical boundary*, Rev. Mod. Phys. **85**, 1083 (2013).

[4] V. E. Manucharyan, J. Koch, L. I. Glazman, and M. H. Devoret, *Fluxonium: Single Cooper-Pair Circuit Free of Charge Offsets*, Science **326**, 113 (2009).

[5] G. Puebla-Hellmann and A. Wallraff, *Realization of gigahertz-frequency impedance-matching circuits for nano-scale devices*, Applied Physics Letters **101**, 053108 (2012).

[6] V. Ranjan, G. Puebla-Hellmann, M. Jung, T. Hasler, A. Nunnenkamp, M. Muoth, C. Hierold, A. Wallraff, and C. Schönenberger, *Clean carbon nanotubes coupled to superconducting impedance-matching circuits*, Nat. Commun. **6**, 7165 (2015).

[7] T. Hasler, M. Jung, V. Ranjan, G. Puebla-Hellmann, A. Wallraff, and C. Schönenberger, *Shot Noise of a Quantum Dot Measured with Gigahertz Impedance Matching*, Physical Review Applied **4**, 54002 (2015).

[8] R. Schoelkopf, P. Wahlgren, A. Kozhevnikov, P. Delsing, and D. Prober, *The Radio-Frequency Single-Electron Transistor (RF-SET): A Fast and Ultrasensitive Electrometer*, Science **280**, 1238 (1998).

[9] J. Chen and J. J. Liou, *On-Chip Spiral Inductors for RF Applications: An Overview*, Journal of Semiconductor Technology and Science **4**, 149 (2004).

[10] C. P. Yue, *On-chip spiral inductors for silicon-based radio-frequency integrated circuits*, Ph.D. thesis, Stanford University (1998), p. 36.

[11] W. W. Xue, B. Davis, F. Pan, J. Stettenheim, T. J. Gilheart, A. J. Rimberg, and Z. Ji, *On-chip matching networks for radio-frequency single-electron transistors*, Applied Physics Letters **91**, 093511 (2007).

[12] K. C. Fong and K. C. Schwab, *Ultrasensitive and Wide-Bandwidth Thermal Measurements of Graphene at Low Temperatures*, Physical Review X **2**, 031006 (2012).

[13] T. Hasler, *Microwave Noise Detection of a Quantum Dot with Stub Impedance Matching*, Ph.D. thesis, University of Basel (2016).

[14] V. Ranjan, *Admittance and Noise Detection in Mesoscopic Systems via GHz Impedance Matching*, Ph.D. thesis, University of Basel (2017).

[15] W. W. Xue, *On-chip superconducting LC matching networks and coplanar waveguides for RF SETs*, Ph.D. thesis, Dartmouth College (2010), p. 79.

[16] C. Altimiras, O. Parlavecchio, P. Joyez, D. Vion, P. Roche, D. Esteve, and F. Portier, *Tunable microwave impedance matching to a high impedance source using a Josephson metamaterial*, Applied Physics Letters **103**, 212601 (2013).

[17] A. Stockklauser, P. Scarlino, J. Koski, S. Gasparinetti, C. K. Andersen, C. Reichl, W. Wegscheider, T. Ihn, K. Ensslin, and A. Wallraff, *Strong Coupling Cavity QED with Gate-Defined Double Quantum Dots Enabled by a High Impedance Resonator*, Physical Review X **011030**, 1 (2017).

[18] M. Devoret, S. Girvin, and R. Schoelkopf, *Circuit-QED: How strong can the coupling between a Josephson junction atom and a transmission line resonator be?*, Annalen der Physik **16**, 767 (2007), https://onlinelibrary.wiley.com/doi/pdf/10.1002/andp.200710261 .

[19] C. Beenakker and C. Schönenberger, *Quantum shot noise*, Physics Today **56**, 37 (2003).

[20] Y. Okazaki, S. Sasaki, and K. Muraki, *Shot noise spectroscopy on a semiconductor quantum dot in the elastic and inelastic cotunneling regimes*, Physical Review B **87**, 041302 (2013).

[21] S. Gustavsson, R. Leturcq, B. Simovič, R. Schleser, P. Studerus, T. Ihn, K. Ensslin, D. Driscoll, and a. Gossard, *Counting statistics and super-Poissonian noise in a quantum dot: Time-resolved measurements of electron transport*, Physical Review B **74**, 195305 (2006).

[22] O. Zarchin, Y. C. Chung, M. Heiblum, D. Rohrlich, and V. Umansky, *Electron Bunching in Transport through Quantum Dots in a High Magnetic Field*, Physical Review Letters **98**, 066801 (2007).

[23] E. Onac, F. Balestro, B. Trauzettel, C. F. J. Lodewijk, and L. P. Kouwenhoven, *Shot-noise detection in a carbon nanotube quantum dot*, Physical Review Letters **96**, 1 (2006).

[24] M. Ferrier, T. Arakawa, T. Hata, R. Fujiwara, R. Delagrange, R. Weil, R. Deblock, R. Sakano, A. Oguri, and K. Kobayashi, *Universality of non-equilibrium fluctuations in strongly correlated quantum liquids*, Nature Physics **12**, 230 (2015).

[25] E. V. Sukhorukov, G. Burkard, and D. Loss, *Noise of a quantum dot system in the cotunneling regime*, Physical Review B **63**, 125315 (2001).

[26] U. Hanke, Y. M. Galperin, K. A. Chao, and N. Zou, *Finite-frequency shot noise in a correlated tunneling current*, Physical Review B **48**, 17209 (1993).

[27] S. Hershfield, J. H. Davies, P. Hyldgaard, C. J. Stanton, and J. W. Wilkins, *Zero-frequency current noise for the double-tunnel-junction Coulomb blockade*, Physical Review B **47**, 1967 (1993).

[28] L. Y. Chen and C. S. Ting, *Noise characteristics of sequential tunneling through double-barrier junctions*, Physical Review B **46**, 4714 (1992).

[29] A. Thielmann, M. H. Hettler, J. König, and G. Schön, *Super-Poissonian noise, negative differential conductance, and relaxation effects in transport through molecules, quantum dots, and nanotubes*, Physical Review B **71**, 045341 (2005).

[30] W. Belzig, *Full counting statistics of super-Poissonian shot noise in multi-level quantum dots*, Physical Review B **71**, 161301 (2005).

[31] C. Fricke, F. Hohls, W. Wegscheider, and R. J. Haug, *Bimodal counting statistics in single-electron tunneling through a quantum dot*, Physical Review B **76**, 155307 (2007).

[32] A. Carmi and Y. Oreg, *Enhanced shot noise in asymmetric interacting two-level systems*, Physical Review B **85**, 45325 (2012).

[33] D. Weinmann, W. Häusler, and B. Kramer, *Spin Blockades in Linear and Nonlinear Transport through Quantum Dots*, Physical Review Letters **74**, 984 (1995).

[34] T. Ihn, *Semiconductor Nanostructures* (Oxford University Press Inc., New York, 2010).

[35] D. Pozar, *Microwave Engineering*, 4th ed. (Wiley, 2012).

[36] A. M. Niknejad, *Electromagnetics for High-Speed Analog and Digital Communication Circuits* (Cambridge University Press, 2007).

[37] C. P. Yue, *On-chip spiral inductors for silicon-based radio-frequency integrated circuits*, Ph.D. thesis, Stanford University (1998).

[38] B.-L. Ooi, D.-X. Xu, and P.-S. Kooi, *A comprehensive explanation on the high quality characteristics of symmetrical octagonal spiral inductor*, IEEE Radio Frequency Integrated Circuits (RFIC) Symposium , 2 (2003).

[39] D. Pozar, *Microwave Engineering*, 4th ed. (Wiley, 2012) pp. 196,197.

[40] J. Stiles, *EECS723 - Microwave Engineering - Signal Flow Graphs* (Kansas University, ITTC, 2009).

[41] M. A. Kastner, *Artificial Atoms*, Physics Today **46**, 24 (1993).

[42] M. A. Reed, *Quantum Dots*, Scientific American **268**, 118 (1993).

[43] R. C. Ashoori, *Electrons in artificial atoms*, Nature **379**, 413 (1996).

[44] L. Kouwenhoven and C. Marcus, *Quantum Dots*, Physics World **11**, 35 (1998).

[45] D. Bera, L. Qian, T.-K. Tseng, and P. Holloway, *Quantum Dots and Their Multimodal Applications: A Review*, Materials **3**, 2260 (2010).

[46] E. A. Laird, F. Kuemmeth, G. A. Steele, K. Grove-Rasmussen, J. Nygård, K. Flensberg, and L. P. Kouwenhoven, *Quantum transport in carbon nanotubes*, Rev. Mod. Phys. **87**, 703 (2015).

[47] M. Dresselhaus, G. Dresselhaus, and P. Eklund, *Science of Fullerenes and Carbon Nanotubes: 19.* C_{60}*-Related Tubules and Spherules* (Academic Press, San Diego, 1996) pp. 756–869.

[48] S. Sapmaz, P. Jarillo-Herrero, L. P. Kouwenhoven, and H. S. J. van der Zant, *Quantum dots in carbon nanotubes*, Semiconductor Science and Technology **21**, S52 (2006).

[49] D. H. Cobden and J. Nygård, *Shell Filling in Closed Single-Wall Carbon Nanotube Quantum Dots*, Physical Review Letters **89**, 4 (2002).

[50] S. Bellucci and P. Onorato, *Single-wall nanotubes: Atomiclike behavior and microscopic approach*, Physical Review B **71**, 1 (2005).

[51] J. Cao, Q. Wang, and H. Dai, *Electron transport in very clean, as-grown suspended carbon nanotubes*, Nature Materials **4**, 745 (2005).

[52] G. G. Samsonidze, A. R. Saito, D. A. Jorio, E. M. A. Pimenta, E. A. G. Souza Filho, F. A. Grüneis, D. G. Dresselhaus, and M. S. Dresselhaus, *The Concept of Cutting Lines in Carbon Nanotube Science*, Journal of Nanoscience and Nanotechnology **3**, 431 (2003).

[53] W. Liang, M. Bockrath, and H. Park, *Shell Filling and Exchange Coupling in Metallic Single-Walled Carbon Nanotubes*, Physical Review Letters **88**, 4 (2002).

[54] C. W. J. Beenakker, *Theory of Coulomb-blockade oscillations in the conductance of a quantum dot*, Physical Review B **44**, 1646 (1991).

[55] M. R. Wegewijs and Y. V. Nazarov, *Inelastic co-tunneling through an excited state of a quantum dot*, arXiv (2001), arXiv:cond-mat/0103579 .

[56] S. Kogan, *Electronic Noise and Fluctuations in Solids* (Cambridge University Press, 1996).

[57] H. B. Callen and T. A. Welton, *Irreversibility and Generalized Noise*, Phys. Rev. **83**, 34 (1951).

[58] R. Kubo, *Statistical-Mechanical Theory of Irreversible Processes. I. General Theory and Simple Applications to Magnetic and Conduction Problems*, Journal of the Physical Society of Japan **12**, 570 (1957).

[59] W. Schottky, *Über spontane Stromschwankungen in verschiedenen Elektrizitätsleitern*, Annalen der Physik **362**, 541 (1918).

[60] T. Heikkilä, *The Physics of Nanoelectronics* (Oxford University Press, 2013).

[61] Y. Blanter and M. Büttiker, *Shot noise in mesoscopic conductors*, Physics Reports **336**, 1 (2000).

[62] F. Grover, *Inductance calculations, working formulas and tables* (D. Van Nostrand, 1946).

[63] H. A. Wheeler, *Formulas for the Skin Effect*, Proceedings of the IRE **30**, 412 (1942).

[64] S. S. Mohan, M. del Mar Hershenson, S. P. Boyd, and T. H. Lee, *Simple Accurate Expressions for Planar Spiral Inductances*, IEEE Journal of Solid-State Circuits **34**, 1419 (1999).

[65] J. J. Viennot, J. Palomo, and T. Kontos, *Stamping single wall nanotubes for circuit quantum electrodynamics*, Applied Physics Letters **104**, (2014).

[66] M.-C. Harabula, V. Ranjan, R. Haller, G. Fülöp, and C. Schönenberger, *Blocking-state influence on shot noise and conductance in quantum dots*, Physical Review B **97**, 115403 (2018).

[67] K. Kaasbjerg and W. Belzig, *Full counting statistics and shot noise of cotunneling in quantum dots and single-molecule transistors*, Physical Review B **91**, 1 (2015).

[68] N. Samkharadze, A. Bruno, P. Scarlino, G. Zheng, D. P. Divincenzo, L. Dicarlo, and L. M. K. Vandersypen, *High-Kinetic-Inductance Superconducting Nanowire Resonators for Circuit QED in a Magnetic Field*, Physical Review Applied **5**, 1 (2016).

[69] D. Niepce, J. Burnett, and J. Bylander, *High Kinetic Inductance NbN Nanowire Superinductors*, arXiv (2018), arXiv:1802.01723 .

[70] M. S. Khalil, M. J. A. Stoutimore, F. C. Wellstood, and K. D. Osborn, *An analysis method for asymmetric resonator transmission applied to superconducting devices*, Journal of Applied Physics **111**, 054510 (2012).

A Resonator characterization at 4.2 K

As part of the lumped-resonator fabrication process (chapter 4, subsections 4.2.1, 4.2.2), characterization measurements carried out in liquid helium at 4.2 K followed the principle of the side experiment exposed here.

This appendix presents a supplement to chapter 5, namely a measurement of a bonded-bridge coil for the extraction of the resonator loss at 4.2 K. With the extracted loss value, we use the LC model to refit the main-experiment data and find little variation in the conductance dependence of the reflectance.

A.1. Loss characterization of a wire-bonded coil

We combined same-geometry coils (fig. 5.1bc) and 50-Ω coplanar transmission lines in a “hanger" configuration (fig. A.1a). We then measured at 4 K the power transmission between ports 1 and 2 with $P = -95\,\mathrm{dBm}$ (higher than the excitation power used in the experiment). We then fit the S_{21} curve (fig. A.1b) with the formula [35]:

$$S_{21} = \frac{2}{2 + \frac{Z_{\mathrm{line}}}{Z}}, \quad Z_{\mathrm{line}} = 50\,\Omega \cdot e^{\mathrm{i}\phi}. \tag{A.1}$$

Here, $Z = Z_{\mathrm{in}}(G = 0)$ from eq. 5.2 stands for a series $R_{\mathrm{loss}}LC$ cicuit; ϕ is a fitting parameter [70] that reproduces the asymmetry of the measured curve, caused by external spurious standing waves due to 50 Ω mismatches. The extracted parameters are: $R_{\mathrm{loss}} = 1.26\,\Omega$, $Z_{\mathrm{c}} = 954\,\Omega$, $f_0 = 3.35\,\mathrm{GHz}$, $\phi = 0.56$. The obtained loss resistance at 4 K is a comfortable upper limit of our 20 mK experiment, mainly because the Al bond wire becomes superconducting and Nb superconductivity gets reinforced in the mK range.

The reduced characteristic impedance in the main experiment $Z_{\mathrm{c}} = 766\,\Omega$ as compared to $Z_{\mathrm{c}} = 954\,\Omega$ in the hanger is explained by a decreased inductance from the two-turn short in the coil. However, the frequency (and $L \cdot C$) is very similar, suggesting that a short can also induce an increase in capacitance. The distributed structure of inductive and capacitive elements in a coil could indeed produce this effect.

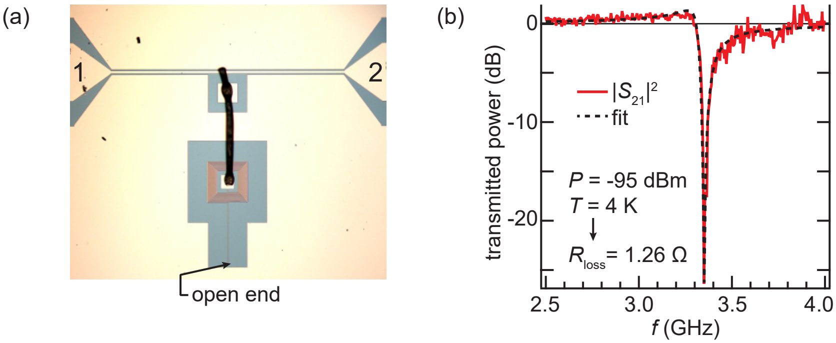

Figure A.1. **(a)** Hanger configuration, i.e. resonator connected to a transmission line. The side of square spiral coil has 210 μm. The bonding wire (black) reaching the inner pad of the coil is evident. The bright color stands for metal. **(b)** The loss resistance of the resonator in (a) is extracted from fitting the transmittance of the hanger, $|S_{21}|^2$.

A.2. Fitting procedure

We extract the unknown circuit parameters L, C, R_{loss}, and $b(f)$ by first fixing a frequency f_{m} close to the resonance frequency. We then plot the measured reflectance values $|\Gamma_{\text{VNA}}|^2$ against the dc-measured dI/dV_{SD} for the same values of V_{G} and V_{SD}. This is shown in fig. A.2 as green diamonds. We next assume that dI/dV_{SD} is equal to G at GHz frequencies. Then we can fit a theoretical dependence to the data points, based on equations 5.3, 5.2. Both the dashed orange and full yellow traces in fig. A.2 are candidate fitting curves. The reflectance values at $G = 0$ and $G \to \infty$ yield the baseline $b(f = f_{\text{m}})$ and R_{loss}; the lack of the latter G value explains why these two parameters cannot be reliably determined simultaneously. We therefore fix $R_{\text{loss}} = 0$; this choice is reasonable also in further noise extraction, as R_{loss} is in series with the much larger characteristic impedance $Z_0 = 50\,\Omega$ of the setup output line. One could be convinced of the low influence of R_{loss} by observing the overlap of the lossless and lossy fits in fig. A.2. In spite of the stability of the extracted parameters in the two fit cases (less than 1 % for L and C), it is important to observe in fig. A.1b and fig. A.2 a ~10 % deviation of the extracted G_{match} value from the measured one (~75 μS). Therefore the accuracy of the extracted S_I is at worst 10 %. In conclusion, working at a fixed frequency outputs effective values of L and C at that specific frequency, while the analysis of a whole frequency range, if possible, should provide more precise circuit parameters.

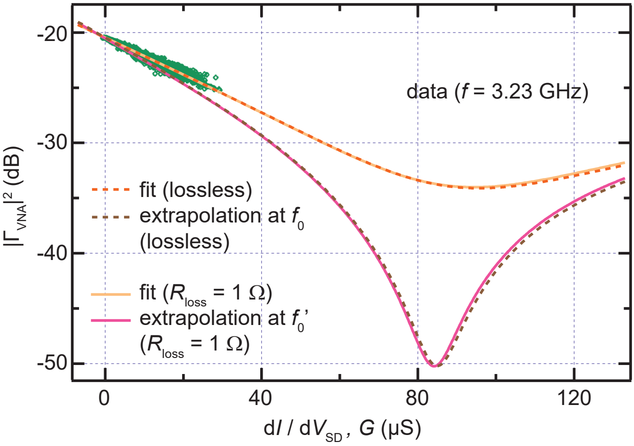

Figure A.2. Reflectance vs. conductance. Green diamonds represent measured $|\Gamma_{\mathrm{VNA}}|^2$ vs. dI/dV_{SD}. The dashed (full) lines are extracted $|\Gamma_{\mathrm{VNA}}|^2(G)$ curves at 3.23 GHz and at the resonance frequency, in the case $R_{\mathrm{loss}} = 0$ ($R_{\mathrm{loss}} = 1\,\Omega$).

B Calibration of the stub tuner data

One of the two samples data sets used in chapter 6, namely device B, was a gated CNT QD (fig. B.1a) with a stub tuner (fig. B.1c). Device B was fabricated and measured by Roy Haller and Vishal Ranjan. They provided the content of this appendix.

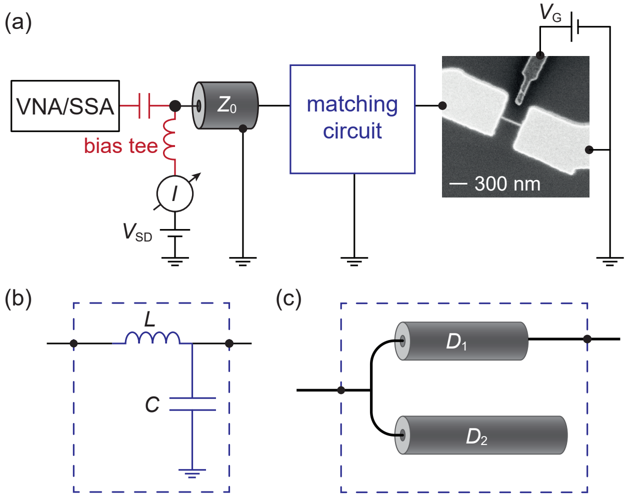

Figure B.1. Reminder: **(a)** simplified sketch of the measurement setup. **(b)** The *LC*-matching circuit corresponds to the other sample, device A. **(c)** Stub tuner for impedance matching, like in device B.

Impedance matching in device B is provided by a stub tuner based on transmission lines. The reflectance response of the circuit for different G is plotted in fig. B.2a. For increasing G, the depth of the resonance increases and goes down to $-30\,\mathrm{dB}$ for $G = 6\,\mu\mathrm{S}$, signifying a complete transmission of the applied input power. Alternatively, at this conductance the circuit effectively transforms the impedance of the CNT device close to $50\,\Omega$. An interesting feature to note is the change in the reflectance spectrum when G is negative. Here the depth and bandwidth of the resonance decrease. This behaviour of negative differential conductance imitates an effective smaller microwave loss of the circuit yielding an amplification.

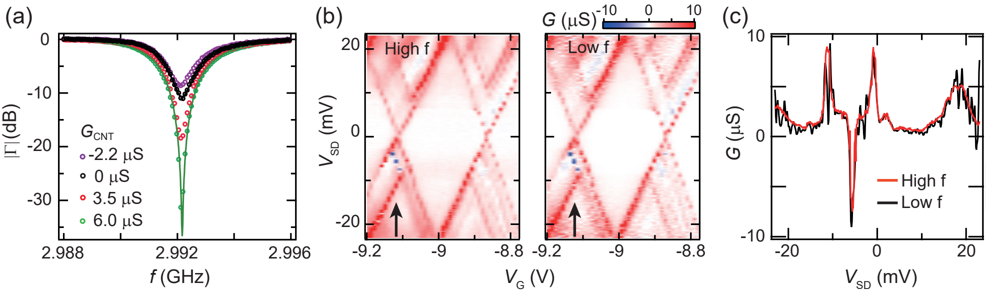

Figure B.2. Circuit calibration of Device B. **(a)** Reflectance response for different values of differential conductance. **(b)** Conductance plots deduced from the reflectance (high f) and from the numerical derivative dI/dV_{SD} of the current (low f). Color scale is kept same for both plots. **(c)** Cuts of conductance shown by the solid arrows in panel (b) showing excellent agreement between two traces.

We describe the reflectance $\Gamma = (Z_{\mathrm{in}}e^{i\phi} - Z_0)/(Z_{\mathrm{in}}e^{i\phi} - Z_0)$, where the phase ϕ accounts for standing waves from the measurement setup and the input impedance Z_{in} reads as

$$Z_{\mathrm{in}} = Z_0 \left(\tanh(\gamma D_2) + \frac{Z_0 + R\tanh(\gamma D_1)}{R + Z_0 \tanh(\gamma D_1)} \right)^{-1}, \tag{B.1}$$

with $\gamma = \alpha + i\beta$ the propagation constant, α the attenuation constant, $\beta = \sqrt{\epsilon_{\mathrm{eff}}}2\pi f/c$ the phase constant and c the speed of light. We first fit the resonance in the Coulomb blockade by setting $G = 0$, yielding $D_1 = 10.16$ mm, $D_2 = 10.52$ mm, $\alpha = 0.019\ \mathrm{m}^{-1}$ and $\epsilon_{\mathrm{eff}} = 5.9$. Both lengths are within 1% of the planned geometric values. The extracted parameters are now fixed and resonance spectra outside the blockade are fit to extract G. These calculations are captured by solid lines in fig. B.2a showing excellent match. We further compare the conductance deduced from reflectance measurements (high frequency) with that from the numerical derivative dI/dV_{SD} (low frequency) of the dc current. As shown in fig. B.2bc, both positive and negative conductances values match well. The main text retains only the high-frequency conductance map (fig. 6.1f).

After the reliable extraction of the parameters, the transfer function from the nanotube to the setup line can be calculated using a simple circuit model [7]:

$$H_V(f,R) = \frac{2Z_0}{R + Z_0} \cdot \frac{e^{\gamma D_1} \cdot \coth(\gamma D_2)}{\Gamma_{\mathrm{L}} + e^{2\gamma D_1} \cdot [1 + 2\coth(\gamma D_2)]}, \tag{B.2}$$

where $\Gamma_{\mathrm{L}} = (R - Z_0)/(R + Z_0)$ is the reflection coefficient seen directly at the device end before the matching circuit. The noise maps are presented in the main text (fig. 6.1g-j).

C Numerical simulations based on FCS

The Matlab code used in running simulations based on full counting statistics (FCS) simulations by Gergő Fülöp and me. It is built on a master equation approach that involves the rates of all possible transitions between the states of the system. Thus, the model takes into account all first- and second-order tunneling processes, as well as thermal excitation and relaxation, in the way presented in [67]. The master equation is extended into a *counting field* in order to make possible the calculation of the *cumulants* (moments), i.e. current and current noise power spectral density. With these, the numerical differential conductance and the Fano factor are derived and plotted on voltage 2D maps (figures 6.5ae, 6.5fj, 7.1b).

C.1. Tunneling amplitudes

This appendix section makes the connection between the main simulation ingredient, namely the tunneling amplitude, and tunneling rates. If the reader chooses to descend to a deeper level, a more detailed description of the FCS framework is given in the next sections.

In the model, we define the tunnel coupling of the QD to lead α via transition $N \to M$ as the complex amplitude of tunneling between lead α and the QD [67],

$$t^{\alpha}_{N\to M} = \langle M|\hat{t}^{\dagger}_{\alpha}|N\rangle = (t^{\alpha}_{M\to N})^{*}, \tag{C.1}$$

such that $|N\rangle$ is the initial state of the QD, $|M\rangle$ its final state, $|N\rangle$ and $|M\rangle$ are consecutive-charge states, and $\hat{t}^{\dagger}_{\alpha}$ is the electron creation operator in the QD, coupled to lead α. In other words, $\hat{t}^{\dagger}_{\alpha}$ is the operator that describes the tunneling of one electron from lead α into the QD. Tunneling rates are proportional to tunneling probabilities, namely the magnitude squared of lead couplings:

$$\Gamma^{\alpha}_{N\to M} \propto |t^{\alpha}_{N\to M}|^2 \quad \text{with } \alpha \in \{\mathrm{S}, \mathrm{D}\}. \tag{C.2}$$

We suppose that tunnel couplings do not depend on V_{G} and V_{SD}. Moreover, considering only real values, their notation simplifies: $t^{\alpha}_{N\to M} = t^{\alpha}_{M\to N} =: t^{\alpha}_{N,M}$.

In a sequential process, two tunneling rates are involved, e.g.

$$\Gamma^{\mathrm{S}}_{N\to N+1} \propto |t^{\mathrm{S}}_{N,N+1}|^2, \tag{C.3}$$

$$\Gamma^{\mathrm{D}}_{N+1\to N} \propto |t^{\mathrm{D}}_{N,N+1}|^2. \tag{C.4}$$

The tunneling rate of an IEC process, $\Gamma^{\mathrm{SD}}_{N\to N^*}$, accounts for both $|N-1\rangle$ and $|N+1\rangle$ as possible virtual states and reads:

$$d\Gamma^{\mathrm{SD}}_{N\to N^*} \propto \left| \frac{t^{\mathrm{D}}_{N,N-1} t^{\mathrm{S}}_{N-1,N^*}}{\mu_{N^*\leftrightarrow N-1} - E} + \frac{t^{\mathrm{S}}_{N,N+1} t^{\mathrm{D}}_{N+1,N^*}}{E - \mu_{N\leftrightarrow N+1}} \right|^2 dE. \tag{C.5}$$

The V_{G} and V_{SD} dependence of the tunneling rates is explicitly taken into account by means of Fermi-Dirac distribution functions. For details, see the following sections and consult ref. [67].

C.2. The FCS theory

The dynamics of the state occupation probabilities of a system is described by its master equation:

$$\dot{\mathbf{p}}(n,t) = \sum_{n'} \mathcal{M}(n-n')\mathbf{p}(n',t), \tag{C.6}$$

with the matrices $\mathcal{M}$ holding the tunneling rates (equations C.2, C.5) between the all the possible states ($|M\rangle$) and the vector $\mathbf{p}$ containing all the state occupation probabilities, $p_M(n,t)$. n is the number of electrons that could have traversed the quantum dot in the time t; in the stationary regime, this is also the number of electrons that could have tunneled from the source into the QD. The probability distribution of the charge transfer is $P(n,t) = \sum_M p_M(n,t)$.

The tunneling mechanisms that we consider are first-order tunneling ($n-n' = \pm 1$) and cotunneling ($n-n' = 0$). As said in the appendix introduction, we also consider excitation and relaxation mechanisms ($n-n' = 0$), with rates included in the $\mathcal{M}$ matrix.

The master equation (eq. C.6) has the form of a convolution around the counting variable n and is therefore easily Fourier-transformable: The master equation in the counting frequency (χ) space, also called *the counting field*, reads:

$$\boxed{\dot{\mathbf{p}}(\chi,t) = \mathcal{M}(\chi)\mathbf{p}(\chi,t),} \tag{C.7}$$

where $\mathbf{p}(\chi,t) = \sum_n \mathbf{p}(n,t)e^{in\chi}$. Deriving $\mathcal{M}(\chi)$ from $\mathcal{M}(-1,0,1)$ is a relatively easy task:

$$\mathcal{M}(\chi) = \mathcal{M}(-1)e^{-i\chi} + \mathcal{M}(0) + \mathcal{M}(+1)e^{i\chi}. \tag{C.8}$$

The FCS is based on obtaining the cumulant-generating function, $\mathcal{S}(\chi,t)$, defined by $e^{\mathcal{S}(\chi,t)} = \langle e^{in\chi}\rangle_n = \sum_n P(n,t)e^{in\chi}$, from the eigenvalue of $\mathcal{M}(\chi)$ with the real part closest to zero, $\Lambda_{\min}$. In the stationary limit, $t_0 \to \infty$, within the Markovian approximation, the relation is [67]:

$$\mathcal{S}(\chi,t_0) = t_0\Lambda_{\min}, \tag{C.9}$$

yielding the cumulants $\frac{\partial^m \mathcal{S}}{\partial(i\chi)^m}\Big|_{\chi\to 0}$. Current and current noise are then written as:

$$\boxed{\begin{aligned} I &= \frac{e}{t_0}\frac{\partial \mathcal{S}}{\partial(i\chi)}\bigg|_{\chi=0}, && \text{(C.10a)} \\ S_I &= \frac{e^2}{t_0}\frac{\partial^2 \mathcal{S}}{\partial(i\chi)^2}\bigg|_{\chi=0}. && \text{(C.10b)} \end{aligned}}$$

C.3. Simple example

In section 6.2 of the main text, we consider a 3-state stationary system where the only transition is first-order tunneling. After sketching its quantum state graph (fig. 6.6), we presented its master equation (eq. 6.7). If by convention the counting lead is the drain (i.e. the counting variable is taken to be the number of electrons arriving at drain, see fig. 6.7b), then we observe that the matrix of the master equation (eq. 6.7) is the sum:

$$\mathcal{M}(-1)+\mathcal{M}(0)+\mathcal{M}(1) = 0 + \begin{pmatrix} -\gamma_1 & 0 & 0 \\ 0 & -\gamma_3 & 0 \\ 0 & 0 & -\gamma_2-\gamma_4 \end{pmatrix} + \begin{pmatrix} 0 & 0 & \gamma_4 \\ 0 & 0 & \gamma_2 \\ \gamma_1 & \gamma_3 & 0 \end{pmatrix}. \tag{C.11}$$

With eq. C.8, one calculates the χ-dependent matrix:

$$\mathcal{M}(\chi) = \begin{pmatrix} -\gamma_1 & 0 & \gamma_4\cdot e^{i\chi} \\ 0 & -\gamma_3 & \gamma_2\cdot e^{i\chi} \\ \gamma_1\cdot e^{i\chi} & \gamma_3\cdot e^{i\chi} & -\gamma_2-\gamma_4 \end{pmatrix}. \tag{C.12}$$

The eigenvalues are further numerically calculated for different $\gamma_1 = \gamma_4 = \gamma$, $\gamma_3 = \gamma/m$ and $\gamma_2 = \gamma/n$, resulting in the cumulant-generating function, $\mathcal{S}(\chi, t_0)$ (eq. C.9). The Fano factor is obtained from equations C.10a, C.10b and plotted in fig. 6.8.

C.4. Rates

When their broadening is smaller than the other energy scales, i.e. $k_{\mathrm{B}}T$ and $|eV|$, the tunneling rates have expressions derived by expanding the T matrix to the desired order:

- first-order tunneling, namely adding an electron to the QD:

$$\Gamma^{\alpha}_{i\to j} = \frac{\Gamma_\alpha}{\hbar}|t_{i\to j}|^2 f_\alpha(\mu_{i\leftrightarrow j}), \tag{C.13}$$

- first-order tunneling, namely removing an electron from the QD:

  $$\Gamma^{\alpha}_{j\to i} = \frac{\Gamma_\alpha}{\hbar} |t_{j\to i}|^2 \Big[1 - f_\alpha(\mu_{i\leftrightarrow j})\Big]. \tag{C.14}$$

  Here above, $|i\rangle$ and $|j\rangle$ are QD states of consecutive charges. $\alpha \in \{\mathrm{S}, \mathrm{D}\}$ designates the lead and Γ_α is the tunnel broadening at electrode α and is measured in energy units. f_α is the Fermi-Dirac distribution function for lead α.

- elastic tunneling:

  $$\Gamma^{\alpha\beta}_{j\to j} = \frac{\Gamma_\alpha \Gamma_\beta}{2\pi\hbar} \int d\epsilon \left| \sum_i \frac{t^{\beta}_{j\to i} t^{\alpha}_{i\to j}}{\epsilon - \mu_{i\leftrightarrow j}} + \sum_k \frac{t^{\alpha}_{j\to k} t^{\beta}_{k\to j}}{\mu_{j\leftrightarrow k} - \epsilon} \right|^2 f_\alpha(\epsilon) \Big[1 - f_\beta(\epsilon)\Big], \tag{C.15}$$

  where $|i\rangle$, $|j\rangle$, $|k\rangle$ are QD states of consecutive charges. The scripts $\alpha, \beta \in \{\mathrm{S}, \mathrm{D}\}$ designates leads and can be different or equal.

- inelastic tunneling:

  $$\Gamma^{\alpha\beta}_{Na\to Nb} = \frac{\Gamma_\alpha \Gamma_\beta}{2\pi\hbar} \int d\epsilon \left| \sum_i \frac{t^{\beta}_{Na\to i} t^{\alpha}_{i\to Nb}}{\epsilon - \mu_{i\leftrightarrow Nb}} + \sum_k \frac{t^{\alpha}_{Na\to k} t^{\beta}_{k\to Nb}}{\mu_{Na\leftrightarrow k} - \epsilon} \right|^2 f_\alpha(\epsilon) \Big[1 - f_\beta(\epsilon - \Delta)\Big], \tag{C.16}$$

  where the QD states $|Na\rangle$, $|Nb\rangle$ have the same number of charge carriers; $|i\rangle$, $|Na\rangle$, $|k\rangle$ are QD states of consecutive charges; $\Delta = |E_{Na} - E_{Nb}|$.

Thermal relaxation is described with the aid of the Bose-Einstein distribution, n_B:

$$\Gamma^{\mathrm{rel}}_{Na\to N} = \frac{\Gamma_{\mathrm{rel}}}{\hbar} |n_\mathrm{B}(\Delta_a)|, \text{ with } \Delta_a = E_{Na} - E_N. \tag{C.17}$$

The symmetric process, thermal excitation, is modeled with the same law.

C.5. Simulation parameters

Let us first recall, in table C.1, the QD configuration of most of our numerical calculations.

Table C.1. Quantum dot states and the corresponding total energies

i	$\|N-1\rangle$	$\|N\rangle$	$\|N^*\rangle$	$\|N+1\rangle$	$\|(N+1)^*\rangle$	$\|N+2\rangle$
E_i	0	ε_0	$\varepsilon_0 + \Delta_0$	$2\varepsilon_0 + U_c$	$2\varepsilon_0 + U_c + \Delta_1$	$3\varepsilon_0 + 3U_c$

The usual values were $\varepsilon_0 = 0.5$, $U_c = 1$, $\hbar = 1$, $\Gamma_{\mathrm{S|D}} = 10^{-3}$, $k_\mathrm{B}T = 4 \cdot 10^{-3}$, $\Gamma_{\mathrm{rel}} = 10^{-6}$. The tunneling rates are given in the main text (chapter 6).

C.6. Matlab code

To run the calculation, execute the script qdot_noise.m. The other .m files are called by it. In the code, the tunneling amplitudes are noted with `ML` and `MR` instead of t^{S} and t^{D}.

qdot_config.m

```matlab
% This file is initially named: qdot_config.m
% The present config and output will be saved in directory:
config_dir = 'config_M2=0.4_M2e=0.6';

% GammaL, GammaR: coupling strength to the normal leads [eV]
% kT: temperature [meV]
% Ea: energy of the first level [meV]
% biasV: bias voltage [mV]; gateVv: gate voltage
% Uc: charging energy [meV]

inelastic_cotunneling = 1; %1 to include inelastic cotunneling; 0 ...
     otherwise

Gamma = 0.001;
GammaL = 1 * Gamma;
GammaR = 1 * Gamma;
Gamma_rel = 0.001 * Gamma; % relax rate

Ea = 0.5;
Uc = 1;
kT = 0.004;

E_spectrum = [  0 ...
                Ea ...
               (2*Ea+Uc) (2*Ea+Uc)+0.1*Uc+1e3*eps (2*Ea+Uc)+0.35*Uc ...
               3*Ea+3*Uc ];
E_electrons = [0  1  2 2 2  3];

%%% Function orb will return the E_spectrum index of an electron, ...
     from the number of electrons and the the orbital number (e.g. ...
     orb (2,2) refers to 2 electrons, 2nd excited state).
subindex = @(vector,i) vector(i);
% N = charge; orbital index is 0 for a ground state
orb = @(N,orbital_index) subindex(find(E_electrons==N),orbital_index+1);
% Groundstate for N electrons
GS = @(N) orb(N,0);

num_states = length(E_spectrum);
% Matrix of relaxation rates
% The upper part contains relaxation rates, the lower part contains ...
     excitation rates
Gamma_rel_mat = Gamma_rel * ones(num_states);

% Tunneling matrix elements (all 1 by default)
% Convention for M(n,m): from state m to state n (as opposed to n->m ...
     in Belzig)
ML = ones(num_states);
ML(GS(1),GS(2)) = 0.4; ML(GS(2),GS(1)) = 0.4;
ML(GS(3),GS(2)) = 0.4; ML(GS(2),GS(3)) = 0.4;
```

```
ML(orb(2,1),GS(1))=0.6; ML(GS(1),orb(2,1))=0.6;
ML(orb(2,1),GS(3))=0.6; ML(GS(3),orb(2,1))=0.6;
MR=ML;

biasVv = linspace(-1.2,1.2,120+1);
gateVv = linspace(1.3,2.7,140+1);
```

Main script: **qdot_noise.m**

```
%% Simulation of a single quantum dot based on a rate eq. model
% capable of noise calculation
% based on Kaasbjerg and Belzig, PRB 91 235413 (2015)
% Authors: Cezar Harabula (general case) and Gergo Fulop (1 excited ...
     level)

% This script uses psin.m from: ...
     https://www.mathworks.com/matlabcentral/fileexchange/
% 5687-polygamma-function-of-arbitrary-order-valid-complex-plane

clc;

% Spectrum and number of electrons in each orbital, to be defined in ...
     config file (qdot_config.m)
E_spectrum = [0];
E_electrons = [0];

qdot_config; % gives E_spectrum, E_electrons, num_states, Gamma*, kT...

hbar = 1;
chi_step=1e-3;
im=sqrt(-1);

E=E_spectrum;

same_charge   = @(i) find(E_electrons==E_electrons(i)  );
previous_charge = @(i) find(E_electrons==E_electrons(i)-1);
next_charge   = @(i) find(E_electrons==E_electrons(i)+1);
E_same_charge   = cellfun(same_charge,  ...
     num2cell(1:num_states),'UniformOutput',false);
E_previous    = ...
     cellfun(previous_charge,num2cell(1:num_states),'UniformOutput',false);
E_next   = cellfun(next_charge,  ...
     num2cell(1:num_states),'UniformOutput',false);

current = zeros(length(gateVv),length(biasVv));
current_old = zeros(length(gateVv),length(biasVv));
current_noise = zeros(length(gateVv),length(biasVv));
error_map = zeros(length(gateVv),length(biasVv));
trigamma_up = zeros(length(gateVv),length(biasVv));
pmatrix = zeros(num_states,length(gateVv)); % for storing the ...
     solution of the stationary p vector (zero bias cut)

Bose = @(en) 1/(exp(en/kT)-1);

I = @(E1,E2,Ea,Eb) Bose(E2-E1)./(Ea-Eb) .* real(...
  psin(  1/2 + im./(2*pi*kT) .* (E2-Ea))  ...
  -psin( 1/2 - im./(2*pi*kT) .* (E2-Eb)) ...
  -psin( 1/2 + im./(2*pi*kT) .* (E1-Ea))  ...
```

```
  +psin( 1/2 - im./(2*pi*kT) .* (E1-Eb)));

J = @(E1,E2,Ea)  1./(2*pi*kT) .*  Bose(E2-E1) .* imag(...
  psin(1, 1/2 + im./(2*pi*kT) .* (E2-Ea))  ...
  -psin(1, 1/2 + im./(2*pi*kT) .* (E1-Ea)));

mu = @(m,n) E(max(m,n))-E(min(m,n)); % because E spectrum is ordered ...
     upon charge state, this correctly returns negative result when ...
     the input consists of E(N,i)>E(N+1,j)

tic

for Vbi = 1:length(biasVv)
  biasV = biasVv(Vbi);
  parfor Vgi = 1:length(gateVv)
    % matrix of tunneling rates; convention: g(n,m) is the tunneling ...
        rate from state m to state n (as opposed to Belzig)
    g = zeros(num_states);
    g_chi = zeros(num_states);
    g_chi_minus = zeros(num_states);

    % matrices of cotunneling rates; same sense convention
    gCotLL = zeros(num_states);
    gCotRR = zeros(num_states);
    gCotLR = zeros(num_states);
    gCotRL = zeros(num_states);

    gL= zeros(num_states);
    gR= zeros(num_states);
    gLe= zeros(num_states); % Le means "exits the QD thru L"
    gRe= zeros(num_states);

    % Fermi functions, symmetric biasing:
    dEL=gateVv(Vgi)-biasV./2;
    dER=gateVv(Vgi)+biasV./2;

    FermiL = @(x)(exp((x-dEL)./kT)+1).^(-1);
    FermiR = @(x)(exp((x-dER)./kT)+1).^(-1);

    % for elastic cotunneling:
    ILR = @(Ea,Eb) I(dEL,dER,Ea,Eb);
    IRL = @(Ea,Eb) I(dER,dEL,Ea,Eb);
    ILL = @(Ea,Eb) I(dEL,dEL,Ea,Eb); % not in Gergo's code
    IRR = @(Ea,Eb) I(dER,dER,Ea,Eb); % not in Gergo's code

    JLR = @(Ea) J(dEL,dER,Ea);
    JRL = @(Ea) J(dER,dEL,Ea);
    JLL = @(Ea) J(dEL,dEL,Ea); % not in Gergo's code
    JRR = @(Ea) J(dER,dER,Ea); % not in Gergo's code

    % for inelastic cotunneling:

    % Delta = excitation energy = E(N,m)-E(N,n) with m,n orbital indices
    ILL_up = @(Ea,Eb,Delta) inelastic_cotunneling* ...
        I(dEL,dEL+Delta,Ea,Eb);
    IRR_up = @(Ea,Eb,Delta) inelastic_cotunneling* ...
        I(dER,dER+Delta,Ea,Eb);
    ILR_up = @(Ea,Eb,Delta) inelastic_cotunneling* ...
```

```
     I(dEL,dER+Delta,Ea,Eb);
IRL_up = @(Ea,Eb,Delta) inelastic_cotunneling* ...
     I(dER,dEL+Delta,Ea,Eb);

JLL_up = @(Ea,Delta) 0;%J(dEL,dEL+Delta,Ea);
JRR_up = @(Ea,Delta) 0;%J(dER,dER+Delta,Ea);
JLR_up = @(Ea,Delta) 0;%J(dEL,dER+Delta,Ea);
JRL_up = @(Ea,Delta) 0;%J(dER,dEL+Delta,Ea);

% Sequential tunneling
% transition rates:

for i = 1:num_states

  for ku = 1:length(E_next{i})
    u = E_next{i}(ku);
    % different charge states, indices i and u (i<u)
    % (filling the dot)
    gL(u,i)= GammaL/hbar .* abs(ML(u,i))^2 .* FermiL(mu(u,i)) ;
    gR(u,i)= GammaR/hbar .* abs(MR(u,i))^2 .* FermiR(mu(u,i));
    g(u,i) = gR(u,i);
    g_chi(u,i) = gL(u,i);
  end

  for kd = 1:length(E_previous{i})
    d = E_previous{i}(kd);
    % different charge states, indices i and d (i>d)
    % (emptying the dot)
    gLe(d,i) = GammaL/hbar .* abs(ML(d,i))^2 .* (1-FermiL(mu(d,i)));
    gRe(d,i) =  GammaR/hbar .* abs(MR(d,i))^2 .*(1-FermiR(mu(d,i)));
    g(d,i) = gRe(d,i);
    g_chi_minus(d,i) = gLe(d,i);
  end

end

% excitation/relaxation (i -> j or j -> i respectively )

for i=1:num_states-1
  for j=i+1:num_states % j is always >i
    if(E_electrons(j)==E_electrons(i)) % tests if j is among the ...
         orbitals of i
      g(i,j)=Gamma_rel_mat(i,j)/hbar *abs(Bose(E(i)-E(j)));
      g(j,i)=Gamma_rel_mat(j,i)/hbar *abs(Bose(E(j)-E(i)));
      % no transport, thus g_chi(_minus) do not change
    end
  end
end

% rate equation matrix:

% diagonal elements
for i=1:num_states

  % diminishing, from emptying
  for j = 1:length(E_previous{i})
    d = E_previous{i}(j);
    g(i,i) = g(i,i) - GammaL/hbar * abs(ML(d,i))^2 .* (1 - ...
```

```
           FermiL(E(i)-E(d)));
      g(i,i) = g(i,i) - GammaR/hbar * abs(MR(d,i))^2 .* (1 - ...
           FermiR(E(i)-E(d)));
    end

    % from filling
    for j = 1:length(E_next{i})
      u = E_next{i}(j);
      g(i,i) = g(i,i) - GammaL/hbar * abs(ML(u,i))^2 .* ...
           FermiL(E(u)-E(i));
      g(i,i) = g(i,i) - GammaR/hbar * abs(MR(u,i))^2 .* ...
           FermiR(E(u)-E(i));
    end

    % from relaxation / thermal excitation
    for j = 1:length(E_same_charge{i})
      s = E_same_charge{i}(j);
      if(i~=s)
        % subtract relax/excitation from i to s
        g(i,i) = g(i,i) - g(s,i);
        % no transport, thus g_chi(_minus) do not change
      end
    end

  end

  % Elastic co-tunnneling:
  for i=1:num_states

    for j=1:length(E_previous{i})
      d = E_previous{i}(j);

      gCotLR(i,i) = gCotLR(i,i) + abs(ML(i,d)*MR(d,i))^2 * ...
           JLR(mu(i,d)); % eq.(45): |term|^2
      gCotRL(i,i) = gCotRL(i,i) + abs(MR(i,d)*ML(d,i))^2 * ...
           JRL(mu(i,d));
      gCotLL(i,i) = gCotLL(i,i) + abs(ML(i,d)*ML(d,i))^2 * ...
           JLL(mu(i,d)); % not in Gergo's code...
      gCotRR(i,i) = gCotRR(i,i) + abs(MR(i,d)*MR(d,i))^2 * ...
           JRR(mu(i,d));

      for j2=1:j-1
        d2 = E_previous{i}(j2);
        gCotLR(i,i) = gCotLR(i,i) + 2 * real( ML(i,d2)*MR(d2,i) * ...
             conj(ML(i,d)*MR(d,i)) * ILR(mu(i,d2),mu(i,d)));% ...
             eq.(45): products
        gCotRL(i,i) = gCotRL(i,i) + 2 * real( MR(i,d2)*ML(d2,i) * ...
             conj(MR(i,d)*ML(d,i)) * IRL(mu(i,d2),mu(i,d)));
        gCotLL(i,i) = gCotLL(i,i) + 2 * real( ML(i,d2)*ML(d2,i) * ...
             conj(ML(i,d)*ML(d,i)) * ILL(mu(i,d2),mu(i,d)));
        gCotRR(i,i) = gCotRR(i,i) + 2 * real( MR(i,d2)*MR(d2,i) * ...
             conj(MR(i,d)*MR(d,i)) * IRR(mu(i,d2),mu(i,d)));
      end
    end

    for j=1:length(E_next{i})
      u = E_next{i}(j);
      gCotLR(i,i) = gCotLR(i,i) + abs(MR(i,u)*ML(u,i))^2 * ...
```

```
             JLR(mu(i,u)); % eq.(42): |term|^2
        gCotRL(i,i) = gCotRL(i,i) + abs(ML(i,u)*MR(u,i))^2 * ...
             JRL(mu(i,u));
        gCotLL(i,i) = gCotLL(i,i) + abs(ML(i,u)*ML(u,i))^2 * ...
             JLL(mu(i,u));
        gCotRR(i,i) = gCotRR(i,i) + abs(MR(i,u)*MR(u,i))^2 * ...
             JRR(mu(i,u));

        for j2=1:j-1
          u2 = E_next{i}(j2);
          gCotLR(i,i) = gCotLR(i,i) + 2 * real(MR(i,u2)*ML(u2,i) * ...
               conj(MR(i,u)*ML(u,i)) * ILR(mu(i,u2),mu(i,u))); % ...
               eq.(42): products
          gCotRL(i,i) = gCotRL(i,i) + 2 * real(ML(i,u2)*MR(u2,i) * ...
               conj(ML(i,u)*MR(u,i)) * IRL(mu(i,u2),mu(i,u)));
          gCotLL(i,i) = gCotLL(i,i) + 2 * real(ML(i,u2)*ML(u2,i) * ...
               conj(ML(i,u)*ML(u,i)) * ILL(mu(i,u2),mu(i,u)));
          gCotRR(i,i) = gCotRR(i,i) + 2 * real(MR(i,u2)*MR(u2,i) * ...
               conj(MR(i,u)*MR(u,i)) * IRR(mu(i,u2),mu(i,u)));
        end

        % now combine up and down states to get the negative reals - ...
             eqs.(43,44)
        for k=1:length(E_previous{i})
          d = E_previous{i}(k);
          gCotLR(i,i) = gCotLR(i,i) - 2 * real(ML(i,d)*MR(d,i) * ...
               conj(MR(i,u)*ML(u,i)) * ILR(mu(i,d),mu(i,u)));
          gCotRL(i,i) = gCotRL(i,i) - 2 * real(MR(i,d)*ML(d,i) * ...
               conj(ML(i,u)*MR(u,i)) * IRL(mu(i,d),mu(i,u)));
          gCotLL(i,i) = gCotLL(i,i) - 2 * real(ML(i,d)*ML(d,i) * ...
               conj(ML(i,u)*ML(u,i)) * ILL(mu(i,d),mu(i,u)));
          gCotRR(i,i) = gCotRR(i,i) - 2 * real(MR(i,d)*MR(d,i) * ...
               conj(MR(i,u)*MR(u,i)) * IRR(mu(i,d),mu(i,u)));
        end
      end

      gCotLR(i,i) = 1/(2*pi*hbar) * GammaL * GammaR * gCotLR(i,i);
      gCotRL(i,i) = 1/(2*pi*hbar) * GammaL * GammaR * gCotRL(i,i);
      gCotLL(i,i) = 1/(2*pi*hbar) * GammaL * GammaL * gCotLL(i,i);
      gCotRR(i,i) = 1/(2*pi*hbar) * GammaR * GammaR * gCotRR(i,i);

      g(i,i) = g(i,i) - gCotLR(i,i) - gCotRL(i,i);% - gCotLL(i,i)- ...
           gCotRR(i,i);
      g_chi(i,i) = g_chi(i,i) + gCotLR(i,i);
      g_chi_minus(i,i) = g_chi_minus(i,i) + gCotRL(i,i);

    end

    % Inelastic cotunneling
    for i=1:num_states
      for j=1:length(E_same_charge{i})
        s = E_same_charge{i}(j);

        if(i==s)
          % this is the elastic case, already calculated
          continue;
        end

```

```
% now, gCotXX(s,i)=0 from initialization

if(i<s) % transition to a higher energy

  Delta = E(s)-E(i);

  for kd=1:length(E_previous{i})
    d = E_previous{i}(kd);

    gCotLL(s,i) = gCotLL(s,i) + abs(ML(s,d)*ML(d,i))^2 * ...
         JLL_up(mu(s,d),Delta);
    gCotRR(s,i) = gCotRR(s,i) + abs(MR(s,d)*MR(d,i))^2 * ...
         JRR_up(mu(s,d),Delta);
    gCotLR(s,i) = gCotLR(s,i) + abs(ML(s,d)*MR(d,i))^2 * ...
         JLR_up(mu(s,d),Delta); % eq.(46): |first_MM_term|^2
    gCotRL(s,i) = gCotRL(s,i) + abs(MR(s,d)*ML(d,i))^2 * ...
         JRL_up(mu(s,d),Delta);

  end

  for ku=1:length(E_next{i})
    u = E_next{i}(ku);

    gCotLL(s,i) = gCotLL(s,i) + abs(ML(s,u)*ML(u,i))^2 * ...
         JLL_up(mu(u,i),Delta);
    gCotRR(s,i) = gCotRR(s,i) + abs(MR(s,u)*MR(u,i))^2 * ...
         JRR_up(mu(u,i),Delta);
    gCotLR(s,i) = gCotLR(s,i) + abs(MR(s,u)*ML(u,i))^2 * ...
         JLR_up(mu(u,i),Delta); % eq.(46): |2nd_MM_term|^2
    gCotRL(s,i) = gCotRL(s,i) + abs(ML(s,u)*MR(u,i))^2 * ...
         JRL_up(mu(u,i),Delta);

  end

  for kd=1:length(E_previous{i})
    d = E_previous{i}(kd);
    for ku=1:length(E_next{i})
      u = E_next{i}(ku);

      gCotLL(s,i) = gCotLL(s,i) - 2 * real(ML(s,d)*ML(d,i) * ...
           conj(ML(s,u)*ML(u,i)) * ...
           ILL_up(mu(s,d),mu(u,i),Delta));
      gCotRR(s,i) = gCotRR(s,i) - 2 * real(MR(s,d)*MR(d,i) * ...
           conj(MR(s,u)*MR(u,i)) * ...
           IRR_up(mu(s,d),mu(u,i),Delta));
      gCotLR(s,i) = gCotLR(s,i) - 2 * real(ML(s,d)*MR(d,i) * ...
           conj(MR(s,u)*ML(u,i)) * ...
           ILR_up(mu(s,d),mu(u,i),Delta)); % eq.(46): product
      trigamma_up(Vgi,Vbi) = IRL_up(mu(s,d),mu(u,i),Delta); ...
           % for debugging
      gCotRL(s,i) = gCotRL(s,i) - 2 * real(MR(s,d)*ML(d,i) * ...
           conj(ML(s,u)*MR(u,i)) * ...
           IRL_up(mu(s,d),mu(u,i),Delta));
    end
  end
end

if(i>s) % transition to a lower energy
```

```
          Delta = -E(s)+E(i);

          for kd=1:length(E_previous{i})
            d = E_previous{i}(kd);

            gCotLL(s,i) = gCotLL(s,i) + abs(ML(s,d)*ML(d,i))^2 * ...
                 JLL_up(mu(s,d),-Delta);
            gCotRR(s,i) = gCotRR(s,i) + abs(MR(s,d)*MR(d,i))^2 * ...
                 JRR_up(mu(s,d),-Delta);
            gCotLR(s,i) = gCotLR(s,i) + abs(ML(s,d)*MR(d,i))^2 * ...
                 JLR_up(mu(s,d),-Delta); % eq.(47): |first_MM_term|^2
            gCotRL(s,i) = gCotRL(s,i) + abs(MR(s,d)*ML(d,i))^2 * ...
                 JRL_up(mu(s,d),-Delta);

          end

          for ku=1:length(E_next{i})
            u = E_next{i}(ku);

            gCotLL(s,i) = gCotLL(s,i) + abs(ML(s,u)*ML(u,i))^2 * ...
                 JLL_up(mu(u,i),-Delta);
            gCotRR(s,i) = gCotRR(s,i) + abs(MR(s,u)*MR(u,i))^2 * ...
                 JRR_up(mu(u,i),-Delta);
            gCotLR(s,i) = gCotLR(s,i) + abs(MR(s,u)*ML(u,i))^2 * ...
                 JLR_up(mu(u,i),-Delta); % eq.(47): |2nd_MM_term|^2
            gCotRL(s,i) = gCotRL(s,i) + abs(ML(s,u)*MR(u,i))^2 * ...
                 JRL_up(mu(u,i),-Delta);

          end

          for kd=1:length(E_previous{i})
            d = E_previous{i}(kd);
            for ku=1:length(E_next{i})
              u = E_next{i}(ku);

              gCotLL(s,i) = gCotLL(s,i) - 2 * real(ML(s,d)*ML(d,i) * ...
                   conj(ML(s,u)*ML(u,i)) ...
                * ILL_up(mu(s,d),mu(u,i),-Delta));
              gCotRR(s,i) = gCotRR(s,i) - 2 * real(MR(s,d)*MR(d,i) * ...
                   conj(MR(s,u)*MR(u,i)) ...
                * IRR_up(mu(s,d),mu(u,i),-Delta));
              gCotLR(s,i) = gCotLR(s,i) - 2 * real(ML(s,d)*MR(d,i) * ...
                   conj(MR(s,u)*ML(u,i)) ...
                * ILR_up(mu(s,d),mu(u,i),-Delta)); % eq.(47): product
              gCotRL(s,i) = gCotRL(s,i) - 2 * real(MR(s,d)*ML(d,i) * ...
                   conj(ML(s,u)*MR(u,i)) ...
                * IRL_up(mu(s,d),mu(u,i),-Delta));
            end
          end
        end

        gCotLL(s,i) = 1/(2*pi*hbar) * GammaL * GammaL * gCotLL(s,i);
        gCotRR(s,i) = 1/(2*pi*hbar) * GammaR * GammaR * gCotRR(s,i);
        gCotLR(s,i) = 1/(2*pi*hbar) * GammaL * GammaR * gCotLR(s,i);
        gCotRL(s,i) = 1/(2*pi*hbar) * GammaR * GammaL * gCotRL(s,i);

        g(s,i) = g(s,i) + gCotLL(s,i) ...
          + gCotRR(s,i) ;
```

```
        g_chi(s,i) = g_chi(s,i) + gCotLR(s,i);
        g_chi_minus(s,i) = g_chi_minus(s,i) + gCotRL(s,i);

        g(i,i) = g(i,i) - gCotLL(s,i) ...
          - gCotRR(s,i) ...
          - gCotLR(s,i) ...
          - gCotRL(s,i);
      end
    end

    for chi = [+chi_step -chi_step 0] % in this specific order

      P = g + g_chi*exp(im*chi) + g_chi_minus*exp(-im*chi);

      if (any(isnan(P(:))))
        sre = nan;
        error_map(Vgi,Vbi)=1;
      else
        if (any(isinf(P(:))))
          1
        end
        % check for inf and replace any infinity by 1e308 (with its ...
             sign)
        P_real = real(P);
        P_real(isinf(P_real)) = sign(P_real(isinf(P_real))) * 1e308; ...
             % larger exponent x 0 = NaN
        P_imag = imag(P);
        P_imag(isinf(P_imag)) = sign(P_imag(isinf(P_imag))) * 1e308; ...
             % larger exponent x 0 = NaN
        P = P_real + 1i * P_imag;

        % diagonalize
        [~,D] = eig(P);
        D=diag(D);
        [~,IND] = min(abs(real(D)));
        sre = D(IND) ;
      end

      if (chi > 0)
        % + chi_step;
        sre_plus = sre ;

      elseif (chi < 0)
        % -chi_step;
        sre_minus = sre ;

      elseif (chi == 0)
        sre_zero = sre ;

        % Old method: should be recovered for chi=0
        pdot_stationary = zeros(num_states,1); %the time derivative ...
             of the probability vector is nil mathematical trick: ...
             setting one pdot to 1 and a row in P to 1, we state ...
             that the sum of the probabilities is 1 (this trick ...
             makes the following equation solvable)
        pdot_stationary(1) = 1; %[1 0 0 0]';
        P(1,:) = ones(1,num_states);
        % solve the stationary probability vector, p
```

```
          p = P\pdot_stationary ;


          if (biasV<1e-4)
            pmatrix(:,Vgi) = p;
          end
          % calculating the current:
          crt=0;
          for i=1:num_states

            for ku = 1:length(E_next{i})
              u = E_next{i}(ku);
              crt = crt + p(i)*gL(u,i);
            end

            for kd = 1:length(E_previous{i})
              d = E_previous{i}(kd);
              crt = crt + p(i)*(-gLe(d,i));
            end
          end
          current_old(Vgi,Vbi) = -1 * crt;
        end


      end % chi end (calculated stuff for both +chi_step and -chi_step)
      %current(Vgi,Vbi) = (sre_plus)./(im*2*chi_step);
      current(Vgi,Vbi) = -(sre_plus-sre_minus)./(im*2*chi_step);
      current_noise(Vgi,Vbi) = ...
           (sre_plus-2*sre_zero+sre_minus)./((im*chi_step)^2);
    end
  end

  toc

  %% display figures and save output

  qdot_noise_display;

  mkdir(config_dir);
  save([config_dir '/qdot_noise.mat'],'current', 'current_noise', ...
       'gateVv', 'biasVv','config_dir');
  copyfile('qdot_config.m', [config_dir '/' config_dir '.m']);
  savefig(fighandle, [config_dir '/' config_dir '.fig'], 'compact');
```

qdot_noise_display.m

```
% This file is named: qdot_noise_display.m
% Displays maps for calculations in qdot_noise.m
% Saves the input qdot data and the resulted figure.
% Alternately, load data from qdot_noise.mat and run this.

% This script uses the bluewhitered color map from: ...
     www.mathworks.com/matlabcentral/fileexchange/4058-bluewhitered
fighandle(1) = figure('rend','painters','pos',[900 500 1000 450]);

spdIdV = subplot(1,5,1);

dIdV = zeros(size(current));
```

```
dV = biasVv(2)-biasVv(1);

for Ei = 1:length(gateVv)
    for Vi = 2:length(biasVv)
        dIdV(Ei,Vi)= (current(Ei,Vi)-current(Ei,Vi-1))./dV;
    end
end
ih=imagesc(gateVv,biasVv,real(dIdV'));
set(gca,'YDir','normal');
caxis ([-.03 .03]);
%title('dI/dV');
colormap(spdIdV,bluewhitered(256))
c=colorbar('southoutside');
min_dIdV = min(dIdV(dIdV<0)); % min(dIdV(dIdV<0)) is a workaround
if(isempty(min_dIdV))
    min_dIdV = min(dIdV(:));
end
c.Limits = [min_dIdV  max(dIdV(:))];
c.Label.String = 'dI/dV';
c.Label.FontSize = 12; c.FontSize = 12;
c.TickDirection='out';
c.TickLength = 0.05;

sp2eI = subplot(1,5,2);
schottky = abs(current);
Si = abs(current_noise);
mS = max( max(schottky(:)), max(Si(:)));
ih=imagesc(gateVv,biasVv,real(schottky'));
set(gca,'YDir','normal');
caxis([0, mS]);
%title('|2eI|');
colormap(sp2eI,flipud(gray))
c=colorbar('southoutside');
c.Label.String = '|2eI|';
c.Label.FontSize = 12; c.FontSize = 12;
c.TickDirection='out';
c.TickLength = 0.05;

spSi = subplot(1,5,3);

ih=imagesc(gateVv,biasVv,real(Si'));
set(gca,'YDir','normal');
caxis([0, mS]);
colormap(spSi,flipud(gray))
c=colorbar('southoutside');
c.Label.String = 'S_I';
c.Label.FontSize = 12; c.FontSize = 12;
c.TickDirection='out';
c.TickLength = 0.05;

spSep = subplot(1,5,4);
S_ep = Si - schottky;
ih=imagesc(gateVv,biasVv,real(S_ep'));
set(ih,'alphadata',~isnan(S_ep'))
set(gca,'YDir','normal');
caxis([min(S_ep(:)), max(S_ep(:))]);
%title('S_{EP}');
colormap(spSep,bluewhitered(256))
```

```
c=colorbar('southoutside');
c.Label.String = 'S_I^{EP}';
c.Label.FontSize = 12; c.FontSize = 12;
c.TickDirection='out';
c.TickLength = 0.05;

spF = subplot(1,5,5);
Fano_factor = Si./schottky;
Fano_factor(schottky<1e-15)=nan;
Fano_factor = Fano_factor - 1;

ih=imagesc(gateVv,biasVv,real(Fano_factor'));
set(ih,'alphadata',~isnan(Fano_factor'))
set(gca,'YDir','normal');
% set(sp,'clim',[0 3]);
caxis([-1, max(8,max(Fano_factor(:)))]);
%title('F');
%colormap(spF,flipud(gray))
colormap(spF,bluewhitered(256))
c=colorbar('southoutside');
c.Limits = [-1 max(Fano_factor(:))];
c.Label.String = 'F-1';
c.Label.FontSize = 12; c.FontSize = 12;
c.TickDirection='out';
c.TickLength = 0.05;
%suptitle(config_dir); %in BioInformatics toolbox
```

D Fabrication Recipes

These are recipes used in resonator and CNT quantum dot fabrication.

LC resonators

Substrate	Undoped Si ($\rho > 1000\,\Omega$cm) with 170 nm of thermal oxide on top
Partial contacts and marks	Ti/Au deposition in the Sharon evaporator • PMMA mask – Spin-coat chlorobenzene-diluted PPMA (thickness 250 nm) – Bake at 180 °C for 5 min. • E-beam lithography – Acceleration voltage 20 kV – Area dose 200 μC/cm^2, line dose 1200 pC/cm – Writefield 2000^2 μm^2, aperture 120 μm – Writefield 200^2 μm^2, aperture 10 μm • Mask development – 1 min in MIBK-IPA (1:3) – Stop in IPA, blow-dry with N_2 • E-beam evaporation in Sharon – First 10 nm of Ti, rate $0.5 - 1$ Å/s – Then Au with a rate ~ 1 Å/s, thickness $30 - 50$ nm • PMMA liftoff – 4 min. in acetone (safe to sonicate) – Acetone jet with syringe

continued on next page...

Covering future CNT area	• PMMA/HSQ bilayer mask – Spin-coat PMMA (thickness 600 nm) – Bake at 180 °C for 5 min. – Spin-coat HSQ (6000 rpm, 60 s) – Bake at 90 °C for 5 min. • E-beam lithography (HSQ is a negative e-beam resist, expose where it should stay) – Acceleration voltage 20 kV – Area dose 200 μC/cm^2 – Writefield 1000^2 μm^2, aperture 120 μm • Developing – 25 s in TMAH (25% solution) – Stop in deionized H_2O and then IPA, blow-dry with N_2 • Reactive-ion etch (RIE) uncovered PMMA in O_2 plasma – Params: O_2-flow 16 sccm, 250 mTorr, 100 W, 9 min.
Nb sputtering	• AJA magnetron sputtering machine – Params: Ar 40 sccm, 4 mTorr, 160 W – Stage rotation ON in case the sample is large – Thickness 100 – 150 nm • Remove PMMA/HSQ mask: 2 min. in acetone
Resonator patterning	• PMMA mask – Spin-coat diluted PPMA (thickness 600 nm) – Bake at 180 °C for 5 min. • E-beam lithography – Acceleration voltage 20 kV – Area dose 130 μC/cm^2 – Aperture 60 μm • Mask development – 1 min in MIBK-IPA (1:3) – Stop in IPA, blow-dry with N_2
Nb etching	• Etching with inductively coupled plasma (ICP) – Ar 25 sccm, Cl_2 40 sccm, 1 Pa, ICP power 100 W, rf power 125 W – Time 50 s, Nb etch rate ∼ 4 nm/s • PMMA removal: 3 min. in acetone (safe to sonicate)

CNT stamping

Substrate	Si with 170 nm thermal oxide on top, patterned with pillars like in fig. 4.3
Catalyst solution	Recipe from Thomas Hasler [13] • 30 mg of Al_2O_2, 93 mg of $Fe(NO_3)_3$– $9H_2O$ and 27 mg of MoO_2Cl_2, dissolved in 60 ml IPA • High-power sonication in cell disrupter – 2 h, $T_{max} = 34\,°C$, pulse ON 0.5 s, pulse OFF 0.5 s • Spin-coat one drop of catalyst on the stamps – 4000 rpm for 30 s – repeat 5 times to get a high CNT density
CVD growth	• Heat furnace to 950 °C under Ar flow (1500 sccm) and H_2 flow (500 sccm) • Growth: replace Ar by CH_4 (1000 sccm) for 10 min. • Cooldown under Ar and H_2 flow again until $T < 320\,°C$
CNT stamping	• Place target substrate in center of mask aligner (Süss MicroTec) stage • Mount a cross-marked glass plate • Use aligner's optical microscope to align plate cross on top of target substrate • Take glass plate out and glue-stamp on its cross the pillared substrate, with a drop of PMMA • Re-mount glass plate in mask aligner • Lift stage until contact • Press target and plate together by turning the wheel until "WEC"=OK, make 6 extra turns up, then release
Stamp reuse	Substrate can be recycled, by cleaning its pillars • HF etching: 40 s/stamp • Stop in water and then IPA, blow-dry with N_2

At this point, final contacts can be fabricated. Note that they will connect to previous (partial) Ti/Au contacts, not onto Nb. This way, no Nb oxide removal is necessary.

CNT contacts and gates

Patterning	• ZEP mask – Spin-coat ZEP-520A diluted with anisole (thickness 300 nm) – Bake at 180 °C for 3 min. • E-beam lithography – Acceleration voltage 10 kV – Area dose 34 μC/cm^2 for a trapezoidal undercut – Aperture 10 μm • Mask development – 60 s in pentylacetate and 10 s in MIBK-IPA (9:1) – Stop in IPA (20 s), blow-dry with N$_2$
Ti/Au evaporation	• E-beam evaporation in Sharon – First 10 nm of Ti, rate 0.5 – 1 Å/s – Then Au with a rate ∼ 1 Å/s, thickness 30 – 50 nm
Mask liftoff	No sonication • 15 min. in NMP at 70 °C – Blow surface with a syringe to remove metal residues • 30 min. in acetone at 50 °C (to remove NMP) – Rinse with IPA and blow-dry with N$_2$

Al wire is bonded on the sample, from an outer contact to the inner contact of the planar coil. The recipe needs practice on dummy samples.

Al wire bonds

Stage mount	• Glue sample on sample holder, with Ag paint • Fixate sample holder on Delvotec bonder stage		
Bonding	work height	22300 μm	
		Bond 1 (outside)	Bond 2 (inside)
	search height	22800 μm	22900 μm
	bond weight	19 g/cN	18 g/cN
	u.s. power	47	47
	u.s. time	53 ms	53 ms
	t.d. steps	10 μm	10 μm
	loop	800 μm, 50 cnt	
	Heights were set to match the Nb surface level: 22978 μm		

Curriculum Vitae

Mihai-Cezar HARABULA AUGUSTIN

Citizen of France and Romania

Research

2014–2018 PhD in experimental physics at the *University of Basel*

- Dissertation in the group of Prof. C. Schönenberger: “Lumped Impedance Matchers and GHz Noise Investigation of Quantum Dots”

Education

2012–2013 Master of Science in Physics at *Université Paris Diderot*

- Official title: *M2 in Quantum Devices*
- Project thesis at the *University of Queensland*, Brisbane, Australia, under the guidance of Dr. J. Sabbatini and Prof. H. Rubinsztein-Dunlop:
  “Numerical stimulation of percolation in a two-species BEC condensate”

2002–2005 Engineer of *Ecole Polytechnique, France*

Professional experience

2005–2012 Positions in industry, entrepreneurship

Publications

First-author articles

- *Blocking-state influence on shot noise and conductance in quantum dots*
  M.-C. Harabula, V. Ranjan, R. Haller, G. Fülöp, and C. Schönenberger
  Physical Review B **97**, 115403 (2018)

- *Measuring a Quantum Dot with an Impedance-Matching On-Chip Superconducting LC Resonator at Gigahertz Frequencies*
  M.-C. Harabula, T. Hasler, G. Fülöp, M. Jung, V. Ranjan, and C. Schönenberger
  Physical Review Applied **8**, 054006 (2017)

Poster contributions

- *Blocking states and inelastic cotunneling outside the Coulomb blockade*
  M.-C. Harabula, V. Ranjan, R. Haller, G. Fülöp, T. Hasler, M. Jung, and C. Schönenberger
  Poster at the conference "Trends in Nanoscience", Kloster Irsee, March 27 - 30, 2017

- *Quantum transport experiments in carbon nanotubes and semiconducting nanowires*
  G. Abulizi, C. Jünger, A. Baumgartner, A. Bordoloi, M.-C. Harabula, V. Ranjan, R. Haller, G. Fülöp, T. Hasler, C. Schönenberger
  Poster at the "7th NCCR QSIT General Meeting", Arosa, February 1 - 3, 2017

- *Carbon nanotube device with impedance-matching LC circuit*
  M.-C. Harabula, V. Ranjan, T. Hasler, M. Jung, and C. Schönenberger
  Poster at the conference "Swiss NanoConvention", Basel, June 30 - July 1, 2016

Acknowledgement

My grateful thanks go to all the people who helped me along my way to the defense of this doctorate thesis.

It will start with my school physics teachers, Mihai Sandu and Elena Hlușcu from Dorohoi, Romania. Professor Sandu, who is not among us anymore, knew how to encourage me and remained my greatest fan until he left. D-na Hlușcu was my trainer for so numerous physics competitions in high school, fighting for me and always giving me unconditional support.

Later, Prof. Jean-Louis Basdevant from École Polytechnique was very receptive in writing for me recommendation letters, many years after my graduation. I warmly thank him for his sympathy and his most precious help. I further acknowledge Prof. Sara Ducci, the chief of my master's program, who accepted me back in the physics world and made possible my application for a PhD position. I am also obliged for Emilie Alix's backing and for Sumit Tewari's aid and comradeship at that time.

A very pleasant intermezzo in my scientific research took place at the University of Queensland, Brisbane, where Prof. Halina Rubinsztein welcomed me in her group. I feel indebted to her, as well as to Tyler Neely, Mark Baker and Jacopo Sabbatini, who made me feel at ease during this internship. From my Australian break I could never forget Florin and Alina Augustin-Ibănescu's friendship, for which I am so grateful.

I thank Prof. Christian Schönenberger, who offered me the opportunity of pursuing a doctoral degree in physics. He also knew when to align my topic to a more fundamental direction. My appreciation is due for his patience towards me, that led to more elegant published results.

I am thankful to my doctorate teammates: Thomas Hasler, my office and lab colleague who put all his kindness in introducing me to nanofabrication; Minkyung Jung, who pushed hard on nanotube sample fabrication and assisted me in measuring; Gergő Fülöp, who advised me and immensely helped me in data analysis, always with tact and scientific rigor; Roy Haller, who put consistent effort in the interpretation of Coulomb diamond noise regimes and so gave valuable insight; Vishal Ranjan, the rf specialist always ready to discard everything. I am also grateful for my other colleagues' friendship and support, either coolies: Andreas Baumgartner, Raphaëlle Delagrange, Gulbostan Ablizi, Simon Zihlmann, Frederick Thomas, Arunav Bordoloi, Lujun Wang, Christian Jünger, Clevin Handschin, Péter Makk, David Indolese, Olivier Faist, Paritosh Karnatak, Lukas Gubser, Mehdi Ramezani, Peter Rickhaus, Jörg Gramich, Samuel d'Hollosy, Gabor Fabian, Julia Samm, Wangyang Fu; or roomies: Michel Calame, Maria el Abbassi, Anton Vladyka, Axel Fanget, Jan Overbeck, Kishan Thodkar, Oliver Braun, Yves Mermoud, Olena Synhaivska, Masoud Baghernejad, Ralph Stoop, Mathias Wipf, Cornelia Nef. I should not forget Barbara Kammermann and Astrid Kalt, for their kind administrative assistance.

I greatly appreciated Carina's loyalty and support—from her dog perspective, she never hesitated to be near me while I was writing this thesis.

I am beholden to my sister, Odeta, who believed in me and encouraged me in all my decisions.

Last, but not least, I want to express my gratitude towards Gloria, who faithfully accompanied me in my quest and endorsed me in all circumstances. Dear Lori, we made it!